Available online at www.sciencedirect.com
SCIENCE DIRECT®
Ocean Modelling xxx (2004) xxx–xxx
Ocean Modelling
www.elsevier.com/locate/ocemod

The regional oceanic modeling system (ROMS): a split-explicit, free-surface, topography-following-coordinate oceanic model

Alexander F. Shchepetkin *, James C. McWilliams

Institute of Geophysics and Planetary Physics, University of California at Los Angeles, 405 Hilgard Avenue, Los Angeles, CA 90024-1567, United States

Received 22 October 2003; received in revised form 18 May 2004; accepted 16 August 2004

Abstract

The purpose of this study is to find a combination of optimal numerical algorithms for time-stepping and mode-splitting suitable for a high-resolution, free-surface, terrain-following coordinate oceanic model. Due to mathematical feedback between the baroclinic momentum and tracer equations and, similarly, between the barotropic momentum and continuity equations, it is advantageous to treat both modes so that, after a time step for the momentum equation, the computed velocities participate immediately in the computation of tracers and continuity, and vice versa, rather than advancing all equations for one time step simultaneously. This leads to a new family of time-stepping algorithms that combine *forward–backward* feedback with the best known synchronous algorithms, allowing an increased time step due to the enhanced internal stability without sacrificing its accuracy. Based on these algorithms we design a split-explicit hydrodynamic kernel for a realistic oceanic model, which addresses multiple numerical issues associated with mode splitting. This kernel utilizes consistent temporal averaging of the barotropic mode via a specially designed filter function to guarantee both *exact* conservation and constancy preservation properties for tracers and yields more accurate (up to second-order), resolved barotropic processes, while preventing aliasing of unresolved barotropic signals into the slow baroclinic motions. It has a more accurate mode-splitting due to redefined barotropic pressure-gradient terms to account for the local variations in density field, while maintaining the computational efficiency of a split model. It is naturally compatible with a variety of centered and

* Corresponding author.
E-mail addresses: alex@atmos.ucla.edu (A.F. Shchepetkin), jcm@atmos.ucla.edu (J.C. McWilliams).

1463-5003/$ - see front matter
doi:10.1016/j.ocemod.2004.08.002

upstream-biased high-order advection algorithms, and helps to mitigate computational cost of expensive physical parameterization of mixing processes and submodels.

1. Introduction

Realistic oceanic circulation models are usually based on Boussinesq, hydrostatic momentum and mass balances, material tracer conservation, seawater's equation of state, and parameterized subgrid-scale transports. Their time integration is made with a decomposition of the 3D fields into barotropic (depth-averaged) and baroclinic (the residual) parts to facilitate the calculation of the pressure-gradient force (Bryan and Cox, 1969). The motivation to build a free-surface oceanic model is twofold. From a physical point of view, it is desirable to recapture processes lost or altered by the rigid-lid assumption. These include tidal motions, altered dispersion relations for the Rossby waves, etc. The other motivation comes from computational economics: as pointed out by Killworth et al. (1991), there is a natural physical ratio of phase speeds for the external and internal gravity-wave modes. Once the model time step is chosen from the CFL criterion based on the fastest baroclinic wave speed, the external mode has to be treated by either (i) a streamfunction method using rigid-lid approximation; or (ii) a two-dimensional (2D) pressure Poisson equation for pressure on the rigid-lid or due to free-surface elevation; or (iii) a special 2D barotropic submodel that uses a smaller time step chosen from a CFL criterion based on the barotropic speed. Approaches (i)–(ii) require solution of a 2D elliptic problem (Dukowicz, 1994; Dukowitz and Smith, 1994) at every time step that, with a conventional Successive Over-Relaxation (SOR) or similar method, requires a number of iterations on the order of the number of grid points in the longest direction of the computational domain. Since on this path the number of operations needed at every grid point at every time step tends to increase with the resolution, on finer grids the approach (iii) tends to be more efficient than the others with a threshold set by the ratio of phase speeds of the external and the fastest internal gravity waves compared to the number of grid points in the longest dimension, [1]

$$\frac{|\,V_{\mathrm{ext}}\,|}{|\,V_{\mathrm{int}}\,|\cdot\max(N_x,N_y)}. \tag{1.1}$$

Despite the long-time existence of split-explicit versions for all three major classes of oceanic models—z-, sigma-, and density-coordinate—there are few published studies about the mathematical aspects: consistency, accuracy, and stability associated with mode splitting (e.g., Higdon and Bennett, 1996; Higdon and de Szoeke, 1997; Hallberg, 1997; Higdon, 2002 and an earlier theoretical work, Yanenko, 1971 and Skamarock and Klemp, 1992) more related to atmospheric

[1] This criterion may be shifted in favor of the rigid-lid model if a more efficient (e.g., conjugate gradient, direct, or multigrid; Multigrid Methods, 1981) elliptic solver is used instead of SOR. These kinds of solvers are available for relatively simple geometries but not for complex geometry and topography. Similarly, if the rigid-lid is abandoned in favor of an implicit free-surface approach, the associated elliptic operator becomes diagonally-dominant: this alleviates the requirements for the solver and ultimately helps to reduce the computational cost (Dvinsky and Dukowicz, 1993; Dukowitz et al., 1993; Dukowitz and Smith, 1994).

modeling. Even within the limits of numerical stability based on the usual CFL condition, mode splitting may introduce additional sources of numerical instability not present in models with uniform time steps nor in rigid-lid models.

The purpose of the present study is to reconsider the computational kernel of an oceanic model, including the optimal choice of time-stepping algorithms for the barotropic and baroclinic momentum and tracer equations, and their mutual interaction. Here we advocate an integrated approach whose main focus is on the time-step limitation coming from the system as a whole that, as we will show, is typically more restrictive than the CFL limitations coming from each equation taken individually. We design a new finite-volume, finite-time-step discretization for the tracer equations to eliminate the conflict between integral conservation and constancy preservation properties associated with the variable free surface. We generalize the barotropic mode to take into account the nonuniform density. Collectively, these steps reduce the mode-splitting error and improve the stability, robustness, and efficiency of the model.

1.1. A generalized topography-following coordinate

The topography-following vertical coordinate system implies that there is a transformation

$$z = z(x, y, \sigma), \tag{1.2}$$

where z is the Cartesian height and σ is the vertical distance from the surface measured as the fraction of the local water column thickness (i.e., $-1 \leqslant \sigma \leqslant 0, \sigma = 0$ corresponds to the free surface, $z = \zeta$ and $\sigma = -1$ corresponds to the oceanic bottom, $z = -h(x, y)$). The resulting system of coordinates is nonorthogonal and leads to a set of chain rules for derivatives,

$$\left.\frac{\partial}{\partial x}\right|_z = \left.\frac{\partial}{\partial x}\right|_\sigma - \left.\frac{\partial z}{\partial x}\right|_\sigma \cdot \frac{\partial}{\partial z}. \tag{1.3}$$

In the case of the classical a-coordinate, (1.2) reduces to

$$z = \sigma \cdot h(x, y). \tag{1.4}$$

This may be combined with nonlinear stretching, $S(\sigma)$

$$z(x, y, \sigma) = S(\sigma) \cdot h(x, y) \tag{1.5}$$

and further generalized into the S-coordinate of (Song and Haidvogel, 1994)—which in essence behaves like (1.4) in shallow regions and (1.5) in deep.

Past experience with σ-coordinate models and intercomparisons with z- and isopycnic-coordinate models (Beckmann, 1998; Willebrand et al., 2001) reveal that the solutions from (T-models exhibit stronger topographic sensitivity than the other two classes of models. This is attributed to the fact that the isosurfaces of the vertical coordinate intersect the isopycnals at some angle, even in the case of horizontally uniform stratification, which causes pressure-gradient error. One way to address this problem is to redesign the model algorithms making them less sensitive to such errors (Shchepetkin and McWilliams, 2003). It is also desirable to allow the possibility of a smooth transition from σ to z-coordinates, such that the top-most isosurfaces are nearly flat while the bottom-most are still aligned with topography. For example, one can chose a set of z-levels,

$\{z^*_{k+\frac{1}{2}} \mid k = 0, 1, \ldots, N\}$ where $z^*_{\frac{1}{2}} = -h_{\max}$ is chosen to be the maximum depth and $z^*_{N+\frac{1}{2}} = 0$ is the unperturbed free surface. [2] Then, starting from the bottom, for $k = 0$ set

$$z_{\frac{1}{2}}(x, y) = -h(x, y) \tag{1.6}$$

and for each $k = 1, \ldots, N-1$ set

$$z_{k+\frac{1}{2}}(x, y) = \max\left(z^*_{k+\frac{1}{2}}, z_{k-\frac{1}{2}}(x, y) + \Delta z_{\min}\right), \tag{1.7}$$

where $\Delta z_{\min}$ is the chosen minimal vertical grid spacing (n.b., to avoid surfacing of coordinate isolines, $\Delta z_{\min} \leqslant h_{\min}/N$, where $h_{\min}$ is the minimal depth). In principle, $\Delta z_{\min}$ may be chosen as infinitely small, so the resultant system is equivalent to a z-coordinate with the necessity of handling the layers near the bottom as "mass-less" layers. Its disadvantage is the nonsmooth transition from z-level to topography-following regions. This nonsmoothness can be repaired by applying 2D diffusion to $z_{k+\frac{1}{2}}$ with a variable diffusivity coefficient—zero for the bottom and increasing toward the surface. The resultant coordinate systems are shown in Fig. 1b–d for the cases of two different degrees of smoothing: case (b) is closer to the stretched σ-coordinate, while (c) retains more features of the original z-coordinate (d). Unlike the (σ-coordinate, in both cases the coordinate surfaces near the top are almost horizontal and have less resemblance to the topography.

Throughout this study we assume that our vertical system of coordinates is no longer separable in the sense that it cannot be generated by the simple relationships (1.5) where $S(\sigma)$ is independent of horizontal coordinates, but involves a full three-dimensional (3D) transformation (1.2).

Consequently, the applicability of the methods developed here is not limited to just a σ- or S-coordinate class of models.

1.2. Perturbed vertical coordinate system

Discretization of vertical coordinate introduces a set of coordinate surfaces,

$$\{z_{k+\frac{1}{2}} = z_{k+\frac{1}{2}}(x, y), \quad k = 0, 1, \ldots, N\}. \tag{1.8}$$

If the ocean is at rest, the free-surface elevation is $\zeta = 0$, hence $z_{N+\frac{1}{2}} = 0$, and the whole set corresponding to zero free-surface $\{z^{(0)}_{k+\frac{1}{2}}\}$ is referred as an unperturbed coordinate system. In the case of a nonzero ζ, all $z_{k+\frac{1}{2}}$ are displaced by a distance proportional to ζ and the distance from the bottom as the fraction of unperturbed local depth

$$z_{k+\frac{1}{2}} = z^{(0)}_{k+\frac{1}{2}} + \zeta\left(1 + \frac{z^{(0)}_{k+\frac{1}{2}}}{h}\right) \tag{1.9}$$

(recall that $z_{\frac{1}{2}} \equiv z^{(0)}_{\frac{1}{2}} \equiv -h$ and $z_{N+\frac{1}{2}} \equiv \zeta$). As a result the perturbed grid-box height, $\Delta z_k \equiv z_{k+\frac{1}{2}} - z_{k-\frac{1}{2}}$, is related to the unperturbed height, $\Delta z^{(0)}_k \equiv z^{(0)}_{k+\frac{1}{2}} - z^{(0)}_{k-\frac{1}{2}}$ according to

[2] For notational consistency throughout this study, $z^*_{k+\frac{1}{2}}$ have half-integer indices to reflect the fact that these z-levels are placed between the tracer point levels on a vertically staggered grid. Specifically, these z-levels correspond to interfaces between two adjacent grid boxes in the finite-volume discretization.

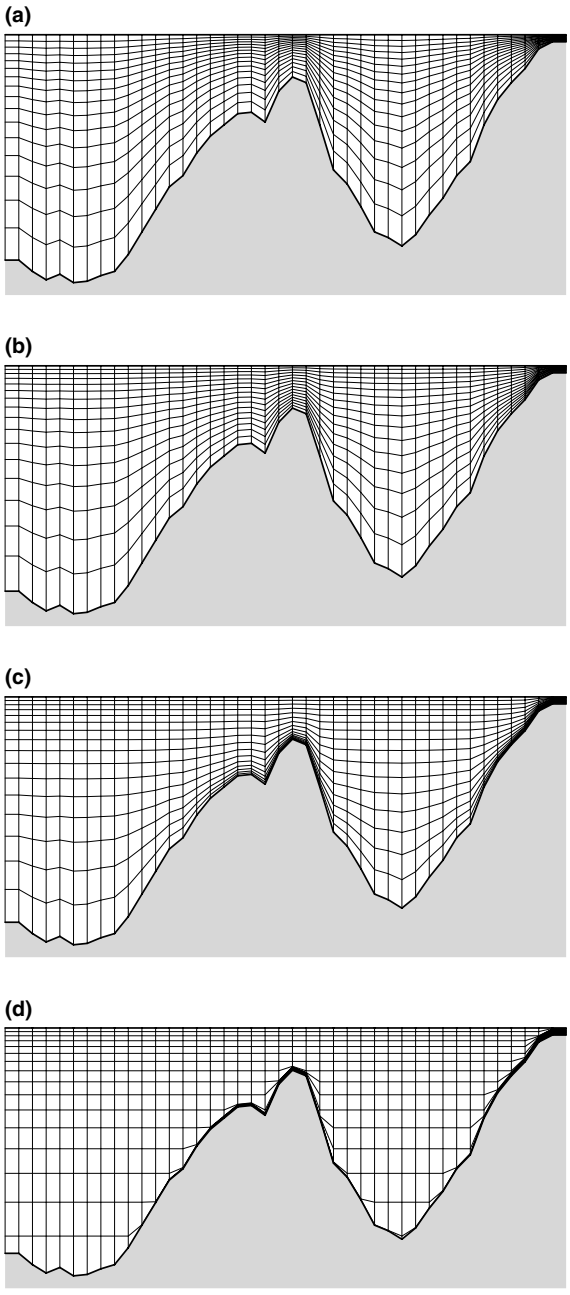

Fig. 1. Examples of vertical coordinate systems: (a) *S*-coordinate of Song and Haidvogel, 1994 with $\theta_s = 3$ and $\theta_b = 0.01$; (b), (c) hybrid $z - \sigma$ coordinate systems obtained by relaxing the (d) z-coordinate system toward the *S*-coordinate.

$$\Delta z_k = \Delta z_k^{(0)}\left(1+\frac{\zeta}{h}\right), \tag{1.10}$$

where the multiplier $(1+\zeta/h)$ is independent of the vertical coordinate. This choice is similar to Higdon and Bennett (1996) and Higdon and de Szoeke (1997), with the exception that they applied it for an isopycnic coordinate model. But it is different from Killworth et al. (1991) and Dukowitz and Smith (1994), where free-surface elevation affects only the top-most grid box, as well as from (Song and Haidvogel, 1994), where each grid box receives the same increment (hence $\Delta z_k = \Delta z_k^{(0)} + \zeta/N$) regardless of its unperturbed size $\Delta z_k^{(0)}$. Later we show that (1.10) has several consequences, including the fact that vertical mass fluxes generated by a purely barotropic motion vanish identically at every interface, $z_{k+\frac{1}{2}}$.

1.3. Conflict between integral and constancy preservation for tracers

Combining the tracer equation in advective form

$$\frac{\partial q}{\partial t} + (\mathbf{u}\cdot\nabla)q = 0 \tag{1.11}$$

with the nondivergence equation,

$$(\nabla\cdot\mathbf{u}) = 0, \tag{1.12}$$

we derive the tracer equation in conservation form,

$$\frac{\partial q}{\partial t} + \nabla\cdot(\mathbf{u}q) = 0. \tag{1.13}$$

As a consequence of (1.11), if the tracer is specified as a spatially uniform field at the initial time, it remains so regardless of the velocity field. On the other hand, as a consequence of (1.13), the volume integral of the tracer concentration is conserved in the absence of incoming and outgoing fluxes across the domain boundary. The continuity equation (1.12) provides the compatibility condition between these two properties. Both properties are valuable and should be considered in constructing numerical oceanic models.

The discretization of (1.13) is usually done using a finite-volume approach

$$\begin{aligned}\Delta\mathscr{V}^{n+1}_{i,j,k} q^{n+1}_{i,j,k} = \Delta\mathscr{V}^{n}_{i,j,k} q^{n}_{i,j,k} - \Delta t\Big[&\tilde{q}_{i+\frac{1}{2},j,k}U_{i+\frac{1}{2},j,k} - \tilde{q}_{i-\frac{1}{2},j,k}U_{i-\frac{1}{2},j,k} + \tilde{q}_{i,j+\frac{1}{2},k}V_{i,j+\frac{1}{2},k} - \tilde{q}_{i,j-\frac{1}{2},k}V_{i,j-\frac{1}{2},k}\\ &+\tilde{q}_{i,j,k+\frac{1}{2}}W_{i,j,k+\frac{1}{2}} - \tilde{q}_{i,j,k-\frac{1}{2}}W_{i,j,k-\frac{1}{2}}\Big],\end{aligned} \tag{1.14}$$

where $q_{i,j,k}$ is understood as a volume-averaged concentration over the grid-box $\Delta\mathscr{V}_{i,j,k}$,

$$q_{i,j,k} = \frac{1}{\Delta\mathscr{V}^{n}_{i,j,k}}\int_{\Delta\mathscr{V}^{n}_{i,j,k}} q\,\mathrm{d}\mathscr{V}. \tag{1.15}$$

The $\tilde{q}_{i+\frac{1}{2},j,k}$ (q with one index half-integer) are the interfacial values of tracer concentration. Uppercase [3] $U_{i+\frac{1}{2},j,k}$, $V_{i,j+\frac{1}{2},k}$, and $W_{i,j,k+\frac{1}{2}}$ are volumetric fluxes [4] in the two horizontal and vertical directions. These are defined as velocity components multiplied by the contact area between two adjacent grid boxes

$$\begin{aligned} U_{i+\frac{1}{2},j,k} &= u_{i+\frac{1}{2},j,k}\Delta z_{i+\frac{1}{2},j,k}\Delta\eta_{i+\frac{1}{2},j} \\ V_{i,j,+\frac{1}{2},k} &= v_{i,j+\frac{1}{2},k}\Delta z_{i,j+\frac{1}{2},k}\Delta\xi_{i,j+\frac{1}{2}}, \end{aligned} \tag{1.16}$$

where $\Delta z_{i+\frac{1}{2},j,k}$, $\Delta\eta_{i,j+\frac{1}{2}}$, and $\Delta z_{i,j+\frac{1}{2},k}$, $\Delta\xi_{i,j+\frac{1}{2}}$, are vertical and horizontal measures of the corresponding grid-box interfaces ($\Delta\varepsilon,\Delta\eta$ are assumed to be nonuniform because of curvilinear horizontal coordinates). The superscripts $n+1$ and n denote new and old time steps. The time step for the flux variables in (1.14) is not specified yet (must be effectively at $n+1/2$ to achieve the second-order temporal accuracy), but the flux form by itself guarantees exact conservation of the global volume integral of the advected quantity as long as there is no net flux across the domain boundary. Setting $q_{i,j,k}\equiv 1$ in (1.14) yields the discretized continuity equation,

$$\Delta\mathscr{V}^{n+1}_{i,j,k} = \Delta\mathscr{V}^{n}_{i,j,k} - \Delta t\cdot\left[U_{i+\frac{1}{2},j,k} - U_{i-\frac{1}{2},j,k} + V_{i,j+\frac{1}{2},k} - V_{i,j-\frac{1}{2},k} + W_{i,j,k+\frac{1}{2}} - W_{i,j,k-\frac{1}{2}}\right]. \tag{1.17}$$

Once it holds, the conservative form of the discrete tracer equation (1.14) also has the property of constancy preservation in addition to global content conservation.

In a hydrostatic model the discrete continuity equation (1.17) is needed to compute vertical velocity rather than grid-box volume $\Delta\mathscr{V}^{n+1}_{i,j,k}$. (The latter is entirely controlled by change of ζ via (1.10).) Hence,

$$W_{i,j,\frac{1}{2}} = 0 \quad \text{at the sea floor and} \tag{1.18}$$

$$W_{i,j,k+\frac{1}{2}} = -\sum_{k'=1}^{k}\left\{\frac{\Delta\mathscr{V}^{n+1}_{i,j,k'} - \Delta\mathscr{V}^{n}_{i,j,k'}}{\Delta t} + U_{i+\frac{1}{2},j,k'} - U_{i-\frac{1}{2},j,k'} + V_{i,j+\frac{1}{2},k'} - V_{i,j-\frac{1}{2},k'}\right\} \quad \text{for all } k=1,2,\ldots,N, \tag{1.19}$$

which, in fact, defines the meaning of $W_{i,j,k+\frac{1}{2}}$ as a finite-volume flux across the *moving* grid-box interface $z_{i,j,k+\frac{1}{2}}$. Vertical summation of (1.17) for different k leads to the equation for the free surface,

$$\zeta^{n+1}_{i,j} = \zeta^{n}_{i,j} - \frac{\Delta t}{\Delta\mathscr{A}_{i,j}}\left[\overline{U}_{i+\frac{1}{2},j} - \overline{U}_{i-\frac{1}{2},j} + \overline{V}_{i,j+\frac{1}{2}} - \overline{V}_{i,j-\frac{1}{2}}\right], \tag{1.20}$$

where $\Delta\mathscr{A}_{i,j}$ is the horizontal area of the grid box i,j;

[3] We use uppercase letters to denote finite-volume fluxes, while the corresponding lowercase letters are reserved for the velocity components. The same convention holds for the barotropic fluxes and velocities that are indicated by an overbar.

[4] We make a Boussinesq approximation that implies density is constant and equal to the background density ρ_0 everywhere except in the gravitational force. This implies that mass conservation is equivalent to volume conservation, and in the present study these two terms are used interchangeably.

$$\overline{U}_{i+\frac{1}{2},j} = \sum_{k=1}^{N} U_{i+\frac{1}{2},j,k}, \quad \overline{V}_{i,j+\frac{1}{2}} = \sum_{k=1}^{N} V_{i,j+\frac{1}{2},j} \tag{1.21}$$

are vertically integrated (barotropic) volume fluxes; and we have used the identity

$$(\zeta_{i,j} + h_{i,j}) \cdot \Delta\mathscr{A}_{i,j} \equiv \sum_{k=1}^{N} \Delta\mathscr{V}_{i,j,k}, \tag{1.22}$$

where $h_{i,j}$ is independent of time. Obviously, setting $k = N$ in (1.19), consistently with 1.20, 1.21 and 1.22 results in

$$W_{i,j,N+\frac{1}{2}} = 0, \tag{1.23}$$

as required by the kinematic boundary condition at the free surface.

Thus far we have assumed that the time step and time-stepping algorithm for the tracer (1.14) and for ζ (1.20) are the same. This would be the case if the barotropic and baroclinic components were advanced using the same small time step dictated by the stability criterion for the barotropic mode; or if the barotropic mode were treated implicitly with a special care to construct finite-volume fluxes $U_{i+\frac{1}{2},j,k}$, $V_{i,j+\frac{1}{2},k}$, and $W_{i,j,k+\frac{1}{2}}$ such that the (1.17) holds exactly and is compatible with (1.21) and (1.23), (Dukowitz and Smith, 1994). In a split-explicit, free-surface model (cf., Blumberg and Mellor, 1987; Killworth et al., 1991), the equation for free-surface (1.20) and the vertically integrated (2D) momenta are advanced using a much smaller time step than the tracer equations. Each baroclinic time step starts with computation of the rhs of the 3D momentum equations. The rhs components are integrated vertically to provide forcing terms for the barotropic mode. During the barotropic time stepping, the free surface and the barotropic velocity components are averaged over the sequence of the barotropic steps and the averaged values are feed back into the 3D momenta. The averaging is needed to prevent temporal aliasing of the signals resolved by the barotropic, but not by the baroclinic step, and [in some models, cf., Nadiga et al., 1997; Hallberg, 1997; Higdon and de Szoeke, 1997; Higdon, 2002, where no dealiazing (averaging) of ζ-equation is actually performed] to provide vertically integrated fluxes consistent with finite-time-step "baroclinic time" free-surface equation (1.20). Then the 3D momenta are advanced to the baroclinic time step $n + 1$ (with violation of the external mode CFL criterion), and vertical integrals of the new fields are subtracted from the similar values from the barotropic submodel. The resultant differences is then uniformly distributed throughout the vertical column to make sure that the corrected 3D velocity components have the same vertical integrals as the barotropic ones. At the same time, free surface ζ at the new baroclinic step is assigned to its new state from the the barotropic submodel.

Perhaps the most delicate matter here is the replacement of free-surface ζ at $n + 1$ with its fast-time-averaged value: not doing so leaves room for aliasing error, while the replacement makes the "slow-time" discrete 2D continuity equation (1.20) hold only within the order of temporal accuracy, but no longer exactly (even thought it is exact at every fast time step). Consequently, it is no longer possible to reconstruct vertical velocity via (1.19) in such a way that the top kinematic

boundary condition (1.23) is respected. [5] As the result, a conservative update of the tracer fields (1.14) looses its constancy preservation property.

2. Accuracy and stability of time-stepping algorithms

Table 4 in Griffies et al. (2000), provides a comprehensive overview of time-stepping and mode-splitting algorithms for virtually all oceanic models currently in use. Despite the large diversity of models, the time-stepping algorithms are mainly limited to applications of classical methods—Leap-Frog (LF), Adams–Bashforth (AB), and Forward–Backward (FB, used almost exclusively for the barotropic mode). In this section we will show that, for oceanic modeling specifically where the time step is restricted mainly by internal or external gravity waves, it is advantageous to use more general algorithms that introduce FB-type feedback into the terms responsible for wave motions while treating other terms differently, with special care to ensure that different algorithms can be combined.

2.1. Simple time stepping

Consider the one-dimensional (1D) linear hyperbolic equation,

$$\frac{\partial q}{\partial t} = -c\frac{\partial q}{\partial x}, \tag{2.1}$$

and 1D hyperbolic system of equations,

$$\frac{\partial \zeta}{\partial t} = -c\frac{\partial u}{\partial x} \qquad \frac{\partial u}{\partial t} = -c\frac{\partial \zeta}{\partial x}, \tag{2.2}$$

where c is phase speed. This is a simple analog for the barotropic mode in the absence of Coriolis force and topography. In the free-surface equation, barotropic mass fluxes are the product of vertically averaged velocities and total depth that depends on ζ; the nonlinear barotropic system (3.46) and (3.47) is similar to both (2.1) and (2.2) in the sense that ζ may be advected by the flow as well as be changed by its divergence. [6] Therefore, our goal is to design an accurate and stable algorithm to advance both (2.1) and (2.2). We focus on achieving the greatest stability for the system (since the waves usually propagate faster than the advection speed), while at the same time minimizing dissipation for the advection equation.

A Fourier transform of (2.1) and (2.2) respectively yields

$$\frac{\partial \hat{q}_k}{\partial t} = -\mathrm{i}\omega_k \cdot \hat{q}_k \tag{2.3}$$

and

[5] Alternatively on might distribute the mismatch in (1.23) throughout the water column, so that the top boundary condition holds, but at the expense of discrepancy in (1.19), (Song and Haidvogel, 1994).

[6] A similar duality exists in the baroclinic case, where temperature and salinity fields are advected directly by the flow as well as coupled with the momentum equations via the background stratification. This results in internal-wave propagation.

$$\frac{\partial \hat{\zeta}_k}{\partial t} = -\mathrm{i}\omega_k \cdot \hat{u}_k, \quad \frac{\partial \hat{u}_k}{\partial t} = -\mathrm{i}\omega_k \cdot \hat{\zeta}_k, \tag{2.4}$$

where $\omega_k \equiv ck$ and, in the continuous case, k is a spatial wavenumber. In the case of spatial second-order finite differences on a staggered grid, (2.2) becomes

$$\begin{aligned} \frac{\partial \zeta_j}{\partial t} &= -c \cdot \frac{u_{j+\frac{1}{2}} - u_{j-\frac{1}{2}}}{\Delta x} \\ \frac{\partial u_{j+\frac{1}{2}}}{\partial t} &= -c \cdot \frac{\zeta_{j+1} - \zeta_j}{\Delta x}. \end{aligned} \tag{2.5}$$

The Fourier transform has the same form as (2.4), except that ω_k is replaced with $\omega_k = c\tilde{k}$ where

$$\tilde{k} = \frac{\sin(\frac{k\Delta x}{2})}{\frac{\Delta x}{2}} = \begin{cases} k, & k\Delta x \ll 1, \\ 2/\Delta x, & k = \pi/\Delta x, \end{cases} \tag{2.6}$$

which has its maximum value $\tilde{k}_{\max} = 2/\Delta x$. This means that if a time stepping algorithm for (2.4) has a stability limit, $\omega \Delta t_{\max}$, it translates into maximum allowed Courant number,

$$\left.\frac{c\Delta t}{\Delta x}\right|_{\max} = \frac{1}{2}\omega \Delta t_{\max}, \tag{2.7}$$

if the same algorithm is applied to (2.5).

Explicit time-stepping algorithms for a single oscillatory equation (2.3) are well studied (Canute et al., 1988; Durran, 1991 and Appendix A). The same algorithms can be applied to the system when the right-hand side terms for both equations in (2.4) are computed at the same time and then added to their respective prognostic variables. This results in the same order of accuracy and stability limit as for the single equation. Let

$$q^{n+1} = \mathscr{F}(q^n, q^{n-1}, \ldots) - \mathrm{i}\alpha \cdot \mathscr{G}(q^n, q^{n-1}, \ldots), \tag{2.8}$$

where $\alpha \equiv \omega \Delta t$, and

$$\begin{aligned} \mathscr{F}(q^n, q^{n-1}, \ldots) &= \sum_{m=0}^{r} \beta_m q^{n-m} \\ \mathscr{G}(q^n, q^{n-1}, \ldots) &= \sum_{m=0}^{r} \gamma_m q^{n-m} \end{aligned}$$

be an explicit time-stepping algorithm for (2.3). Its amplification factors are the roots of the characteristic polynomial,

$$\mathscr{P}(\lambda) = \lambda^{r+1} - \sum_{m=0}^{r} (\beta_m - \mathrm{i}\alpha \cdot \gamma_m)\lambda^{r-m}. \tag{2.9}$$

Similarly, the same algorithm applied to the system, (2.4),

$$\begin{pmatrix} \zeta \\ u \end{pmatrix}^{n+1} = \mathscr{F}\left[\begin{pmatrix} \zeta \\ u \end{pmatrix}^{n}, \begin{pmatrix} \zeta \\ u \end{pmatrix}^{n-1}, \ldots\right] + \begin{pmatrix} 0 & -\mathrm{i}\alpha \\ -\mathrm{i}\alpha & 0 \end{pmatrix} \cdot \mathscr{G}\left[\begin{pmatrix} \zeta \\ u \end{pmatrix}^{n}, \begin{pmatrix} \zeta \\ u \end{pmatrix}^{n-1}, \ldots\right], \tag{2.10}$$

gives

$$\begin{vmatrix} \mathscr{F}(1,\lambda^{-1},\ldots)-\lambda & -\mathrm{i}\alpha\cdot\mathscr{G}(1,\lambda^{-1},\ldots) \\ -\mathrm{i}\alpha\cdot\mathscr{G}(1,\lambda^{-1},\ldots) & \mathscr{F}(1,\lambda^{-1},\ldots)-\lambda \end{vmatrix} = 0 \tag{2.11}$$

or

$$(\mathscr{F}(1,\lambda^{-1},\ldots)-\lambda)^2+\alpha^2\mathscr{G}^2(1,\lambda^{-1},\ldots) = \left(\lambda-\sum_{m=0}^{r}(\beta_m-\mathrm{i}\alpha\cdot\gamma_m)\lambda^{-m}\right) \times\left(\lambda-\sum_{m=0}^{r}(\beta_m+\mathrm{i}\alpha\cdot\gamma_m)\lambda^{-m}\right)=0. \tag{2.12}$$

This obviously has the same set of roots as (2.9) as well as their complex conjugates, since the coefficients β_m and γ_m are real numbers. Eq. (2.8) is the most general form that covers both single-step (e.g., LF and AB (AB2, AB3)) and multistage algorithms (e.g., Runge–Kutta (RK2, RK3), and various predictor–correctors). In the last case, β_m and γ_m also depend on α, but they are still real-valued.

Eqs. (2.8)–(2.10) are not the most efficient way to advance the system (2.2) since none of them has an efficiency factor exceeding unity (Appendix A). [7] In contrast, a simple FB step

$$\begin{aligned} \zeta^{n+1} &= \zeta^n-\mathrm{i}\alpha\cdot u^n \\ u^{n+1} &= u^n-\mathrm{i}\alpha\cdot\zeta^{n+1} \end{aligned} \tag{2.13}$$

retains its stability up to $\alpha=2$. The FB algorithm may be rewritten in matrix form as

$$\begin{pmatrix}\zeta\\ u\end{pmatrix}^{n+1} = \begin{pmatrix}1 & -\mathrm{i}\alpha\\ -\mathrm{i}\alpha & 1-\alpha^2\end{pmatrix}\begin{pmatrix}\zeta\\ u\end{pmatrix}^{n}, \tag{2.14}$$

leading to characteristic equation

$$\lambda^2-(2-\alpha^2)\lambda+1=0. \tag{2.15}$$

This has roots

$$\lambda_\pm = 1-\frac{\alpha^2}{2}\pm\mathrm{i}\alpha\sqrt{1-\frac{\alpha^2}{4}}. \tag{2.16}$$

Obviously $|\lambda_\pm|\equiv 1$ as long as the expression under the square root remains positive (i.e., $\alpha\leqslant 2$). Substitution of the "ideal" value of $\lambda=\mathrm{e}^{\pm\mathrm{i}\alpha}$ into (2.15) and subsequent expansion in Taylor series for small σ results in a mismatch between the left- and right-hand sides. To cancel the leading-order term of this mismatch, $\frac{\alpha^3}{24}$, we set $\lambda=\mathrm{e}^{\pm\mathrm{i}\alpha(1+\frac{1}{24}\alpha^2)}$; this indicates that the phase approximation has second-order accuracy. The positions of the roots $\lambda_\pm$ on a complex plane are shown in Fig. 2. As predicted, they show a positive dispersion.

[7] The efficiency factor is defined as the maximum allowed Courant number α divided by the number of computations of the right-hand side per time step.

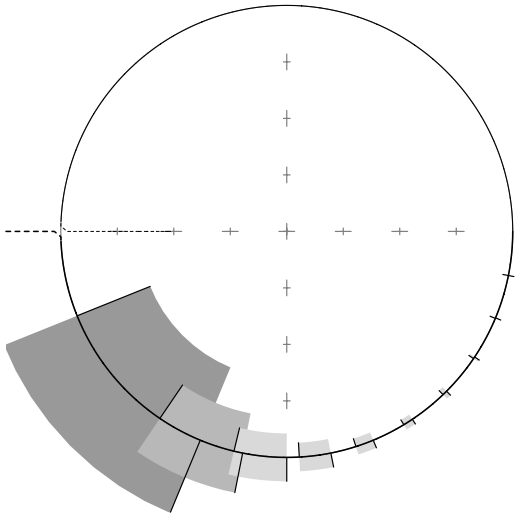

Fig. 2. Roots of the characteristic equation for the FB algorithm (2.13) on the complex plane. Tickmarks on the outer side of the unit circle point to the location of "ideal" amplification factors $e^{-i\alpha}$, where $\alpha = \{-\frac{\pi i}{16}, -\frac{\pi i}{8}, -\frac{3\pi i}{16}, \ldots\}$. Tickmarks on the inner-side indicate the location of the actual roots (2.16) corresponding to the same values of a. The mismatch between inner and outer tickmarks indicates the phase error, also illustrated here by the shaded sectors.

The FB algorithm has been successfully used in many models for the barotropic mode (Bleck and Smith, 1990; Killworth et al., 1991; Hallberg, 1997). Its efficiency is explained by the fact that ζ^{n+1} is immediately used in the computation of u^{n+1}, while in (2.10) it is used only during the next time step (or substep if a predictor–corrector scheme is used). Compared with LF, FB is twice as efficient, and it does not have computational modes since both roots correspond to physical waves traveling to the left and right. Furthermore, because one needs to suppress the computational modes of LF, the efficiency contrast is even larger.

An difficulty in using FB comes from the fact that the forward step is unconditionally unstable for (2.1). In the context of a free-surface model, this implies that unless the actual free-surface equation is linearized,

$$\overline{\mathbf{U}} = (h+\zeta)\bar{\mathbf{u}} \rightarrow \overline{\mathbf{U}} = h\bar{\mathbf{u}} \tag{2.17}$$

the algorithm is unstable due to the advective features of in the free-surface equation. The linearization is undesirable because it destroys the consistency of the 3D continuity equation and eventually results in loss of conservation or constancy preservation for the tracers. In (2.17) $\overline{\mathbf{U}}$ is the vertically integrated (barotropic) mass flux; $\bar{\mathbf{u}}$ is the vertically averaged velocity; h is topography; and $(h+\zeta)$ is the total thickness of the water column. A similar obstacle occurs for the Coriolis force where a special treatment is required (e.g., an AB3; an implicit time step; or treating $\bar{u}, \bar{v}$-components using FB in alternating sequence, Bleck and Smith, 1990). Additionally, FB and LF are quite inaccurate in terms of phase error at the second half of their ranges of stability, and neither provides any damping for motions it cannot accurately represent. Therefore, we seek to generalize the FB algorithm such that the first substep—the update of ζ—is stable if applied to single oscillation equation (2.3). A secondary goal is to improve on the phase error of FB.

2.2. Generalized predictor–corrector algorithm

The simplest predictor–corrector algorithm is the second-order RK2 step modified by introducing terms with coefficients β and ε to make the predictor substep,

$$\zeta^{n+1,*} = \zeta^n - \mathrm{i}\alpha \cdot u^n \tag{2.18}$$

$$u^{n+1} = u^n - \mathrm{i}\alpha \cdot (\beta\zeta^{n+1,*} + (1-\beta)\zeta^n), \tag{2.19}$$

and the corrector substep

$$\zeta^{n+1} = \zeta^n - \frac{\mathrm{i}\alpha}{2} \cdot (u^{n+1,*} + u^n) \tag{2.20}$$

$$u^{n+1} = u^n - \frac{\mathrm{i}\alpha}{2} \cdot (\epsilon\zeta^{n+1} + (1-\epsilon)\zeta^{n+1,*} + \zeta^n)\cdot \tag{2.21}$$

The case $\beta = \epsilon = 0$ corresponds to the original RK2 that is second-order accurate and is known to have a weak instability for a hyperbolic problem. The presence of the new terms with β and ϵ makes it similar to FB in the sense that as soon as each prognostic variable is updated, the new values participate immediately in the update of the partner variable (cf., the synchronous time step (2.10) where it happens only during the next step).

Algorithm (2.18)–(2.21) can be rewritten in matrix form as a single step

$$\begin{pmatrix}\zeta\\ u\end{pmatrix}^{n+1} = \begin{pmatrix} 1-\frac{\alpha^2}{2} & -\mathrm{i}\alpha\left(1-\frac{\alpha^2\beta}{2}\right)\\ -\mathrm{i}\alpha\left(1-\frac{\alpha^2\epsilon}{4}\right) & 1-\frac{\alpha^2}{2}+\frac{\alpha^4\beta\epsilon}{4}\end{pmatrix}\begin{pmatrix}\zeta\\ u\end{pmatrix}^{n},$$

which leads to the characteristic equation

$$P(\lambda) = \lambda^2 - \left(2-\alpha^2+\frac{\alpha^4\beta\epsilon}{4}\right)\lambda + 1 + \frac{\alpha^4}{4}(1-2\beta-\epsilon+\beta\epsilon) = 0, \tag{2.22}$$

where coefficients β and ϵ are yet to be specified. The order of approximation of $\lambda = \mathrm{e}^{\mathrm{i}\alpha} + \mathcal{O}(\alpha^n)$, when $\alpha \to 0$, can be estimated by the order of smallness of $P(\mathrm{e}^{\mathrm{i}\alpha}) = \mathcal{O}(\alpha^m)$, however, it should be noted that for all settings of coefficients β and ϵ,

$$\frac{\partial}{\partial\lambda}P(\lambda)\bigg|_{\substack{\alpha=0\\ \lambda=1}} = 0 \quad \text{but} \quad \frac{\partial}{\partial\lambda^2}P(\lambda)\bigg|_{\substack{\alpha=0\\ \lambda=1}} \neq 0, \tag{2.23}$$

therefore to achieve a certain order of accuracy for λ, we must ensure that $P(\mathrm{e}^{\mathrm{i}\alpha})$ is one order smaller. To chose β and ϵ we substitute $\lambda = \mathrm{e}^{\mathrm{i}\alpha}$ into (2.22) and expand it in Taylor series for small α, after which it becomes

$$\alpha^4\left(\frac{1}{3}-\frac{\beta}{2}-\frac{\epsilon}{4}\right) + \mathrm{i}\alpha^5\left(\frac{1}{12}-\frac{\beta\epsilon}{4}\right) + \mathcal{O}(\alpha^6) = 0. \tag{2.24}$$

Setting $\epsilon = \frac{4}{3} - 2\beta$ eliminates the $\mathcal{O}(\alpha^4)$-term, transforming the above into

$$+\mathrm{i}\alpha^5\left[\frac{1}{36}+\frac{1}{2}\left(\beta-\frac{1}{3}\right)^2\right]+\mathcal{O}(\alpha^6)=0. \tag{2.25}$$

No choice of real-valued β can eliminate the $\mathcal{O}(\alpha^5)$; however, $\beta = \frac{1}{3}$ minimizes it. The resultant algorithm is third-order accurate for the approximation of $\lambda(\alpha) = \mathrm{e}^{\mathrm{i}\alpha}$ with a dissipative leading-order truncation term. Location of its characteristic roots relatively to the unit circle is shown in Fig. 3, indicating a much smaller phase error in comparison with the classical FB. Stability of algorithms of this family is always limited by one of its physical modes leaving the unit circle along the negative real axis, so substituting $\lambda = -1$ and $\epsilon = \frac{4}{3} - 2\beta$ into (2.22), we obtain

$$4-\alpha^2+\left[\frac{1}{36}-\left(\beta-\frac{1}{3}\right)^2\right]\alpha^4=0, \tag{2.26}$$

which is to be solved for α. The form of this equation suggests that the largest stability limit is achieved by setting $\beta = 1/3$—remarkably, the same value, as to minimize the truncation error. The corresponding $\alpha_{\max} = \sqrt{6(3-\sqrt{5})} \approx 2.140932539$ exceeds the limit of all algorithms of similar computational costs (i.e. predictor–corrector type) shown in Fig. 20, Appendix A, but is quite modest relatively to FB, given that twice-as many computations required. Due to the fact that this algorithm does not require any knowledge of past time steps, it is a good choice for the beginning time step since it cures the usual problem of accuracy loss associated with a forward Euler step.

Another commonly used algorithm is the Leap-Frog–Trapezoidal Rule (LF–TR) predictor–corrector step. Following the same methodology, we introduce FB-feedback (β- and ϵ-terms) between the equations during both the predictor stage

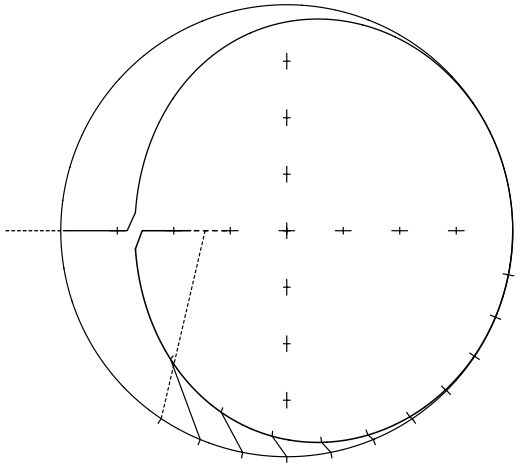

Fig. 3. Roots of the characteristic equation for the modified RK2 algorithm (2.18)–(2.21) with coefficients set to achieve the smallest possible truncation error among all third-order schemes, $\epsilon = 4/3 - 2\beta$ (bottom). This sets $\beta = 1/3$, $\epsilon = 2/3$, resulting in $\alpha_{\max} = 2.140932539$. As in Fig. 2, tickmarks on the outer side of the unit circle point to the location of "ideal" amplification factors $\mathrm{e}^{-\mathrm{i}\alpha}$. These are connected with the actual roots corresponding to the same values of α.

$$\zeta^{n+1,*} = \zeta^{n-1} - 2\mathrm{i}\alpha \cdot u^n \tag{2.27}$$

$$u^{n+1,*} = u^{n-1} - 2\mathrm{i}\alpha \cdot \left[(1-2\beta)\zeta^n + \beta(\zeta^{n+1,*} + \zeta^{n-1})\right] \tag{2.28}$$

and the corrector stage,

$$\zeta^{n+1} = \zeta^n - \mathrm{i}\alpha \cdot \left\{\left(\frac{1}{2}-\gamma\right)u^{n+1,*} + \left(\frac{1}{2}+2\gamma\right)u^n - \gamma u^{n-1}\right\}, \tag{2.29}$$

$$u^{n+1} = u^n - \mathrm{i}\alpha \cdot \left\{\left(\frac{1}{2}-\gamma\right)\left[\epsilon\zeta^{n+1} + (1-\epsilon)\zeta^{n+1,*}\right] + \left(\frac{1}{2}+2\gamma\right)\zeta^n - \gamma\zeta^{n-1}\right\}. \tag{2.30}$$

When $\beta = \epsilon = \gamma = 0$, this is equivalent to the familiar LF–TR algorithm with the stability limit $\alpha_{\max} = \sqrt{2}$. $\beta = \epsilon = 0$ and $\gamma = 1/12$ result in LF–AM3, which is third-order accurate and has the slightly larger stability limit of 1.587 (Appendix A). The presence of β-terms in the LF-step (2.27) and (2.28) used alone (without corrector) is known sometimes as Shuman's averaging (Brown and Campana, 1978). As follows from their analysis, β-terms do not cause any numerical dumping (despite the obvious visual similarity with Asselin filter), but rather change phase behavior of the algorithm. The meaningful range of β is $0 \leqslant \beta < 1/4$, with maximum stability achieved at the upper end. And, similarly to LF, Shuman's algorithm possesses nondecaying computational modes.

The algorithm (2.27)–(2.30) may be rewritten in matrix form

$$\begin{pmatrix}\zeta\\ u\end{pmatrix}^{n+1} = \begin{pmatrix}A & -\mathrm{i}\beta\\ -\mathrm{i}C & D\end{pmatrix}\begin{pmatrix}\zeta\\ u\end{pmatrix}^{n} + \begin{pmatrix}E & -\mathrm{i}F\\ -\mathrm{i}G & H\end{pmatrix}\begin{pmatrix}\zeta\\ u\end{pmatrix}^{n-1} \tag{2.31}$$

where

$$A = 1 - 2\alpha^2\left(\frac{1}{2}-\gamma\right)(1-2\beta), \quad B = \alpha\left\{\frac{1}{2}+2\gamma-4\alpha^2\left(\frac{1}{2}-\gamma\right)\beta\right\},$$

$$C = \alpha\left\{\frac{1}{2}+2\gamma+\epsilon\left(\frac{1}{2}-\gamma\right)\left[1-2\alpha^2\left(\frac{1}{2}-\gamma\right)\times(1-2\beta)\right]\right\},$$

$$D = 1 - 2\alpha^2\left(\frac{1}{2}-\gamma\right)\left\{1-\epsilon\left[\frac{3}{4}-\gamma+2\alpha^2\left(\frac{1}{2}-\gamma\right)\beta\right]\right\},$$

$$E = -4\alpha^2\left(\frac{1}{2}-\gamma\right)\beta, \quad F = \alpha\left(\frac{1}{2}-2\gamma\right),$$

$$H = -\alpha^2\left(\frac{1}{2}-\gamma\right)\left(\frac{1}{2}-2\gamma\right)\epsilon, \quad G = \alpha\left\{\frac{1}{2}-2\gamma-\epsilon\left(\frac{1}{2}-\gamma\right)\left[1+4\alpha^2\left(\frac{1}{2}-\gamma\right)\beta\right]\right\}.$$

This leads to the characteristic equation.

$$\lambda^2 - (A+D)\lambda + AD + BC - H - E + (AH + ED + BG + FC)\lambda^{-1} + (EH + FG)\lambda^{-2} = 0, \tag{2.32}$$

which we rewrite as

$$\lambda^2 + (-2 + \alpha^2 p' + \alpha^4 p'')\lambda + 1 + \alpha^2 q' + \alpha^4 q'' + (\alpha^2 r' + \alpha^4 r'')\lambda^{-1} + \alpha^2 s'\lambda^{-2} = 0 \tag{2.33}$$

to facilitate further analysis. Unlike $A, B, \ldots, H$ above, the new coefficients $p', p'', \ldots, s'$ in (2.33)

$$p' = 4\left(\frac{1}{2} - \gamma\right)\left[1 - \beta - \epsilon\left(\frac{3}{8} - \frac{\gamma}{2}\right)\right], \quad p'' = -4\left(\frac{1}{2} - \gamma\right)^2 \beta\epsilon,$$

$$q' = -4\left(\frac{1}{2} - \gamma\right)\left[1 - 2\beta - \epsilon\left(\frac{5}{8} - \frac{\gamma}{2}\right)\right] + \left(\frac{1}{2} + 2\gamma\right)^2,$$

$$q'' = 4\left(\frac{1}{2} - \gamma\right)\left[\left(\frac{1}{2} - \gamma\right)(1 - 2\beta)(1 - \epsilon) - \left(\frac{1}{2} + 2\gamma\right)\beta\right],$$

$$r' = 2\left(\frac{1}{2} + 2\gamma\right)\left[\frac{1}{2} - 2\gamma - \frac{\epsilon}{2}\left(\frac{1}{2} - \gamma\right)\right] - 4\left(\frac{1}{2} - \gamma\right)\beta,$$

$$r'' = 4\left(\frac{1}{2} - \gamma\right)\left[\frac{1}{2} - \epsilon\left(\frac{1}{2} - \gamma\right)\right]\beta,$$

$$s' = \left(\frac{1}{2} - 2\gamma\right)\left[\frac{1}{2} - 2\gamma - \epsilon\left(\frac{1}{2} - \gamma\right)\right]$$

do not depend on α. (It should be noted that in the derivation above products BG and ED contain $\mathcal{O}(\alpha^6)$ terms which cancel each other, resulting in no appearance of a $r'''\alpha^6$ term. Similar cancellation occurs between the $\mathcal{O}(\alpha^4)$ terms in EH and FG, hence there is no $s''\alpha^4$ in (2.33).)

Substitution of $\lambda = e^{i\alpha}$ into (2.33) and subsequent Taylor series expansion for powers of α yields

$$\begin{aligned}
&\alpha^2(p' + q' + r' + s' - 1) + i\alpha^3(p' - r' - 2s' - 1)\\
&\quad + \alpha^4\left(\frac{7}{12} - \frac{p'}{6} + p'' + q'' - \frac{r'}{2} + r'' - 2s'\right) + i\alpha^5\left(\frac{1}{4} - \frac{p'}{6} + p'' + \frac{r'}{6} - r'' + \frac{4}{3}s'\right)\\
&\quad + \frac{\alpha^6}{2}\left(-\frac{31}{180} + \frac{p'}{12} - p'' + \frac{r'}{12} - r'' + \frac{4}{3}s'\right) + \mathcal{O}(\alpha^7) = 0,
\end{aligned} \tag{2.34}$$

where it can be immediately verified that, after the substitution p', p'',...,s', the $\mathcal{O}(\alpha^2)$ and $\mathcal{O}(\alpha^3)$ terms identically vanish for any choice of values of γ, β, and ϵ, while the $\mathcal{O}(\alpha^4)$ term becomes

$$-\alpha^4\left(\frac{1}{6}-2\gamma\right). \tag{2.35}$$

This indicates that setting $\gamma = 1/12$ ensures third-order accuracy, regardless of the settings of β and ϵ.

Once $\gamma = 1/12$ is chosen, p', p'',...,s' become

$$p' = \frac{5}{3}\left(1-\beta-\frac{\epsilon}{2}\right), \quad p'' = -\frac{25}{36}\beta\epsilon, \quad q' = -\frac{11}{9}+\frac{10}{3}\beta+\frac{35}{36}\epsilon,$$

$$q'' = \frac{25}{18}\left(\frac{1}{2}-\frac{9}{5}\beta-\frac{\epsilon}{2}+\beta\epsilon\right),$$

$$r' = \frac{4}{9}-\frac{5}{3}\beta-\frac{5}{18}\epsilon, \quad r'' = \frac{5}{6}\beta\left(1-\frac{5}{6}\epsilon\right),$$

$$s' = \frac{1}{9}-\frac{5}{36}\epsilon.$$

After substituting these into (2.34), we derive that β and ϵ must satisfy

$$\beta = \frac{7}{30}-\frac{\epsilon}{6} \tag{2.36}$$

in order to eliminate the $\mathcal{O}(\alpha^5)$ term, and

$$\frac{1}{75}-\frac{11}{12}\epsilon-4\beta+5\beta\epsilon = 0 \tag{2.37}$$

to eliminate $\mathcal{O}(\alpha^6)$. Satisfying the first only or both of these conditions result respectively in the fourth- and fifth-order accuracy approximation for the phase multiplier. Using (2.36) to exclude β from (2.37), one can derive a single quadratic equation for ϵ. It does not have a real-valued solution, so one can only minimize the error in (2.37) by choosing $\epsilon = 11/20$ and $\beta = 17/120$ (hence (2.36) is satisfied). This results in fourth-order accuracy with the minimum possible truncation error (among all possible β, γ, and ϵ) and in the stability limit $\alpha_{\max} = 1.851640$ (Fig. 4). Remarkably, this setting of β, ϵ in not far away from the largest stability limit among the fourth-order schemes with β and ϵ related via (2.36), (Fig. 5, left).

Thus far, we have explored the possibility of achieving the best possible accuracy. For the barotropic mode in a split-explicit model, the design goals are different: the truncation error is of lesser priority, but it is desirable that the algorithm have a large stability limit and be dissipative for high frequencies. Arguably, the same is true for the baroclinic mode, but to a lesser extent, because in most cases accurate representation of the phase speed of internal waves is not the main objective but they impose a CFL limitation onto the time step. For the next step in our exploration we treat β and ϵ as independent free parameters and produce a two-dimensional map of the

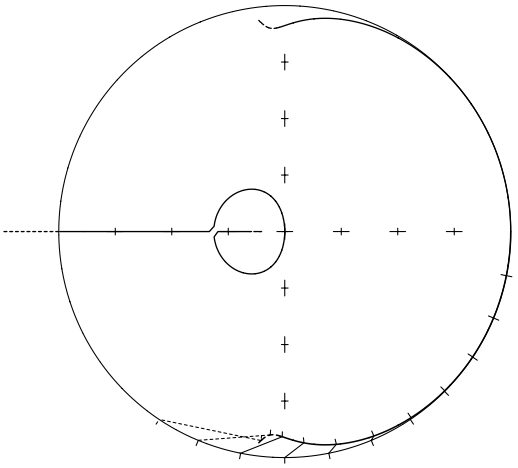

Fig. 4. Roots of the characteristic polynomial for algorithm (2.27)–(2.30) with $\gamma = 1/12$, $\beta = 17/120$, $\epsilon = 11/20$, corresponding to the minimal possible truncation error among all settings of γ, β, and ϵ. Its stability limit is $\alpha_{\max} = 1.851640$.

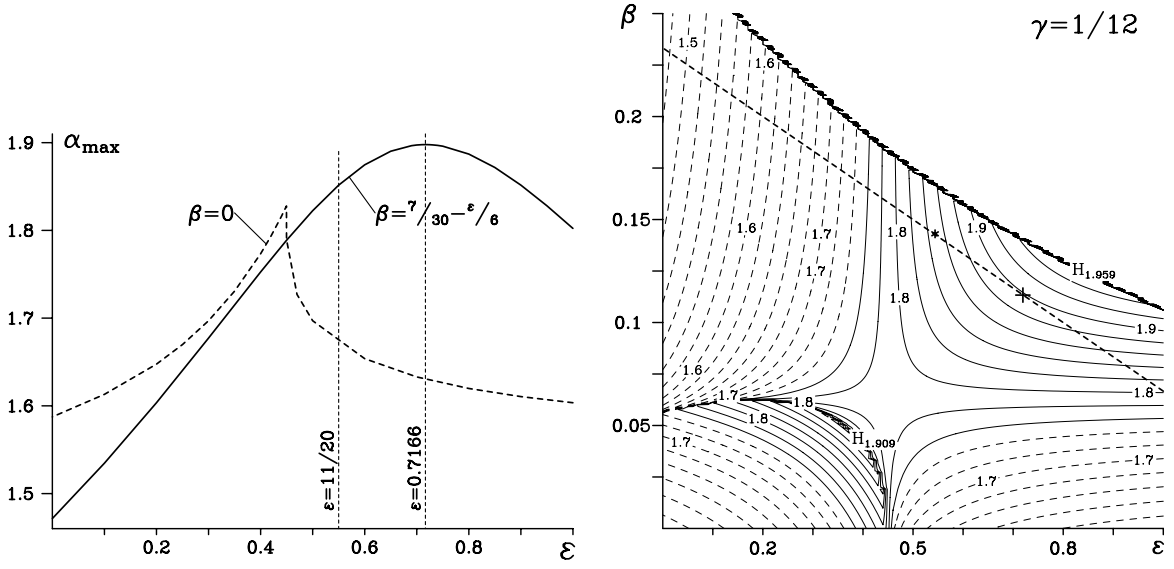

Fig. 5. (left) Stability limit $\alpha_{\max}$ as a function of ϵ for algorithm (2.27)–(2.30) with $\gamma = 1/12$ for two different settings of β: (solid) along the line of vanishing $\mathcal{O}(\alpha^5)$ term (2.36) and (dashed) $\beta = 0$. (right) $\alpha_{\max}$ as function of ϵ, β with fixed $\gamma = 1/12$. Contours below $\alpha = 1.75$ are shown in dashed lines. The empty area in the upper-right corner corresponds to schemes with an asymptotic instability of the physical modes. Note the appearance of two maxima of stability, at $(\epsilon, \beta) = (0.83, 0.126)$ just on the edge of asymptotic instability, and $(0.39, 0.044)$. The straight dashed line approximately parallel to the edge corresponds to a zero $\mathcal{O}(\alpha^5)$ truncation term. The asterisk * and cross + on this line denote locations of the minimal truncation error and maximum stability limit among the forth-order algorithms.

stability limit $\alpha_{\max}(\epsilon, \beta)$, while still maintaining third-order accuracy, $\gamma = 1/12$ (Fig. 5, right). There are two maxima of stability at $(\epsilon, \beta) = (0.83, 0.126)$ and $(0.39, 0.044)$. Their characteristic roots are

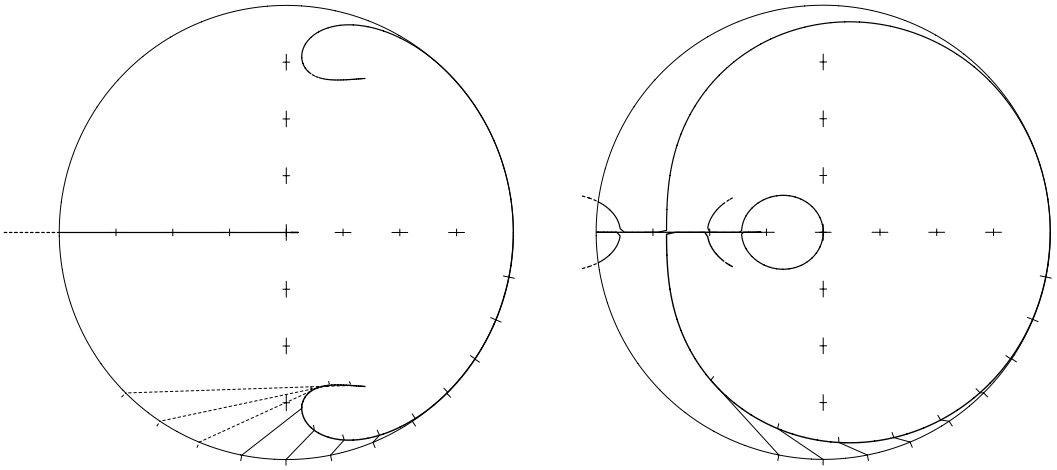

Fig. 6. Characteristic roots of algorithms corresponding to the primary (left) and secondary (right) maxima of stability limit in Fig. 5.

shown on Fig. 6. Though only formally third-order accurate, the algorithm shown on the upper panel exhibits very small phase error—virtually indistinguishable from that in Fig. 4—and, it has remarkably small numerical dissipation for almost the whole of its stability range. This is not surprising, since its (ϵ, β) are not far away from the minimum of truncation error. The primary maximum on Fig. 5, right, is located on the edge asymptotic instability, which explains its small dissipation: the stability for the algorithm in the vicinity of this point is restricted by one of the computational modes leaving the unit circle along the negative direction of the real axis, and the limit increases when increasing both ϵ and β. However, after crossing the edge, the physical modes became weakly (asymptotically) unstable due to changes in higher-order truncation terms (recall that regardless of β, ϵ all these schemes are at least third-order accurate). Consequently, the location right on the edge on (β, ϵ)-plane corresponds to a delicate balance in these terms, resulting in a overall extremely low and delayed dissipation. In contrast, the algorithm corresponding to the secondary maximum possesses no special properties, and its behavior in phase error and dissipation rate is typical for a common third-order accurate scheme (cf., Fig. 3 or LF–AM3 step on Fig. 20, Appendix A).

Giving up third-order accuracy allows us to threat γ as a free parameter and makes it possible to achieve a much greater stability limit. To do so, for each γ from the range of $-0.07 \leqslant \gamma \leqslant 1/12$ we scan the (β, ϵ)-plane in a manner similar to Fig. 5, bottom, to find values that produce the largest $\alpha_{\max}$. The outcome is summarized in the top left panel Fig. 7. The other three panels show examples of algorithms from this sequence. When γ decreases and then becomes negative, the arms corresponding to the physical mode contract, allowing a larger stability limit. At the same time, the roots corresponding to the computational mode became closer to the unit circle, and finally touch it at $\gamma = -0.055$. Although this shows the possibility of a dramatic increase of $\alpha_{\max}$ up to 2.8, algorithms with negative γ do not behave well in practice because of poor damping of the computational mode. This leads to a compromise choice of $\gamma = 0$, resulting in $\alpha_{\max} = 2.41$ that is still 70% more efficient than the standard LF–TR.

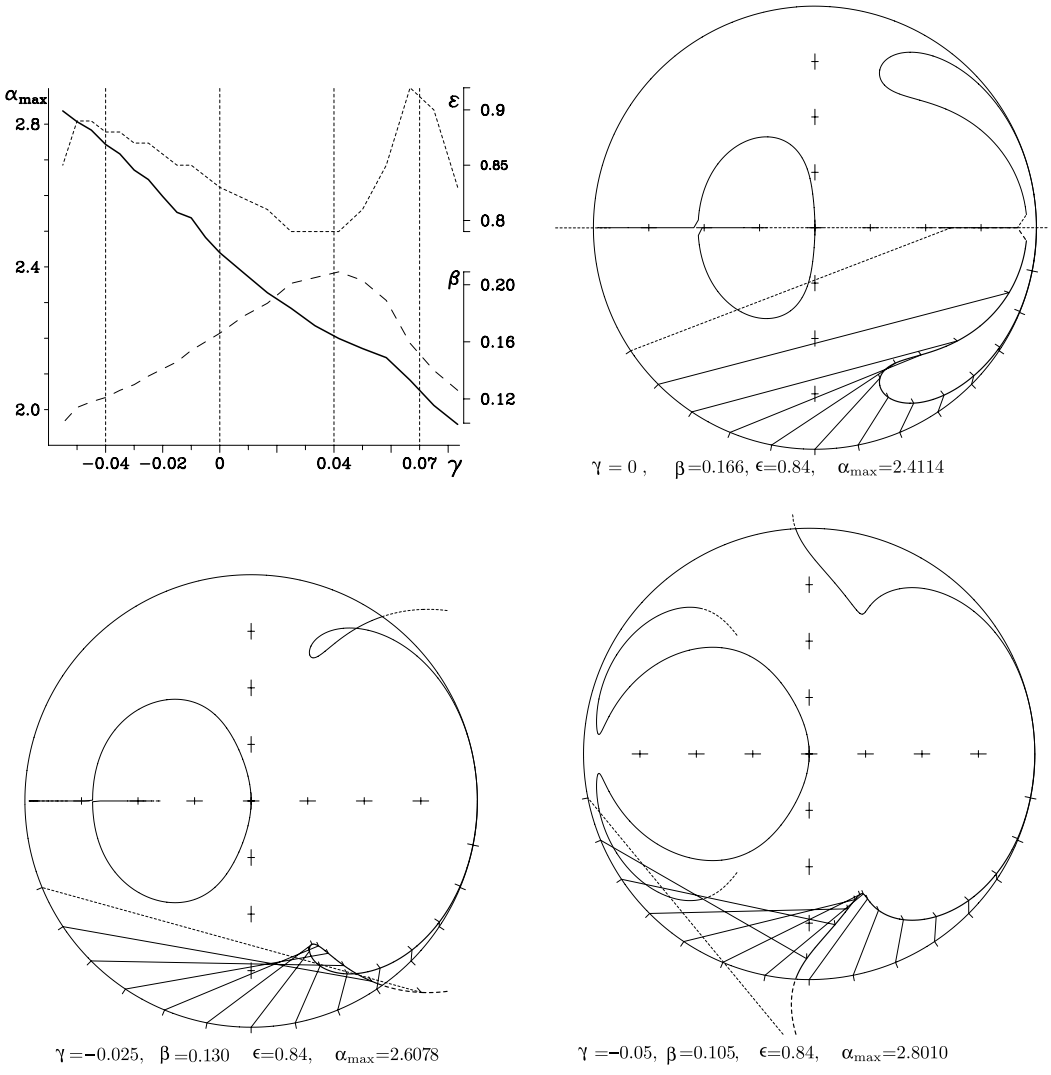

Fig. 7. (top left) Maximum achievable stability limits α_{max} as function of γ for the algorithm (2.27)–(2.30), with β (plotted in long-dashed line) and ϵ (short dashes) optimized for stability range for each value of γ. The associated ranges for β, ϵ are shown on the right axis. Note that with the departure from $\gamma = 1/12$ (hence loss of third-order accuracy), it is possible to expand significantly the stability range at the expense of accuracy. The three remaining panels show the location of the roots of the characteristic polynomials for three sets of $(\gamma, \beta, \epsilon)$ taken from the curves on the upper left.

As the final remark, we note that the system (2.27)–(2.30) may be reformulated as

$$\zeta^{n+\frac{1}{2}} = \left(\frac{1}{2} - 2\gamma\right)\zeta^{n-1} + \left(\frac{1}{2} + 2\gamma\right)\zeta^{n} - \mathrm{i}\alpha(1-2\gamma)u^{n}, \tag{2.38}$$

$$u^{n+\frac{1}{2}} = \left(\frac{1}{2} - 2\gamma\right)u^{n-1} + \left(\frac{1}{2} + 2\gamma\right)u^{n} - \mathrm{i}\alpha(1-2\gamma)\left[\zeta^{n} + \beta\frac{2\zeta^{n+\frac{1}{2}} - 3\zeta^{n} + \zeta^{n-1}}{1-2\gamma}\right] \tag{2.39}$$

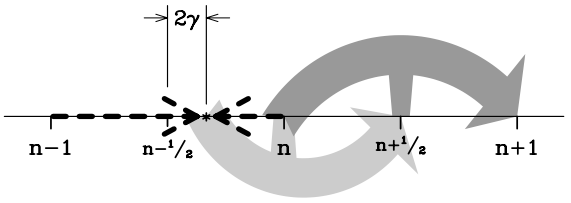

Fig. 8. Geometrical interpretation of reformulated LF–AM3 predictor–corrector step (2.38)–(2.41) with $\beta = \epsilon = 0$. Initial data at $n-1$ and n are linearly interpolated to $n-\frac{1}{2}+2\gamma$ (bold dashed arrows) and advanced to $n+\frac{1}{2}$; using rhs at n (light gray curved arrow, predictor). The resultant values participate only in the computation of rhs. at $n+\frac{1}{2}$ to advance prognostic variables from n to $n+1$ (dark gray arrow, corrector), and they do not need to be stored from one time step to the other.

followed by

$$\zeta^{n+1} = \zeta^n - \mathrm{i}\alpha u^{n+\frac{1}{2}}, \tag{2.40}$$

$$u^{n+1} = u^n - \mathrm{i}\alpha\left\{(1-\epsilon)\zeta^{n+\frac{1}{2}} + \epsilon\left[\left(\frac{1}{2}-\gamma\right)\zeta^{n+1} + \left(\frac{1}{2}+2\gamma\right)\zeta^n - \gamma\zeta^{n-1}\right]\right\} \tag{2.41}$$

after which the provisional values $\zeta^{n+\frac{1}{2}}$ and $u^{n+\frac{1}{2}}$ are discarded. This algorithm can be interpreted as a combination of linear interpolation and two LF-like steps (Fig. 8), and in the case of a linear system it gives the same result as the original version (2.27)–(2.30). The key distinction between the two is that a temporal interpolation of the complete rhs is replaced with an interpolation of prognostic variables, with subsequent computation of right-hand side terms from the interpolated values; this leads to a slightly different result in the nonlinear case, but consistent within second-order accuracy. The practical advantage of the alternative form (2.38)–(2.41) is that it leads to a more efficient code because it eliminates the need to store time tendencies for the prognostic variables from one time step to the next.

2.3. Generalized forward–backward algorithm

We first consider an AB2-like two-point extrapolation of rhs for (ζ-equation in combination with a three-point AM3-like interpolation for pressure gradient term in u-equation

$$\begin{aligned}\zeta^{n+1} &= \zeta^n - \mathrm{i}\alpha[(1+\beta)u^n - \beta u^{n-1}],\\ u^{n+1} &= u^n - \mathrm{i}\alpha[(1-\gamma-\epsilon)\zeta^{n+1} + \gamma\zeta^n + \epsilon\zeta^{n-1}],\end{aligned} \tag{2.42}$$

where β, γ, and ϵ are not specified yet. The corresponding characteristic equation is

$$\begin{aligned}&P\lambda^2 - [2-\alpha^2(1-\gamma-\epsilon)(1+\beta)]\lambda + 1 - \alpha^2(\beta-\gamma-2\beta\gamma-\beta\epsilon)\\ &\quad + \alpha^2(\epsilon+\beta\epsilon-\beta\gamma)\lambda^{-1} - \alpha^2\beta\epsilon\lambda^{-2} = 0.\end{aligned} \tag{2.43}$$

As it is done previously, (2.22)–(2.24) and the discussion there, we substitute $\lambda = \mathrm{e}^{\mathrm{i}\alpha}$ into (2.43) and Taylor-expand for small α

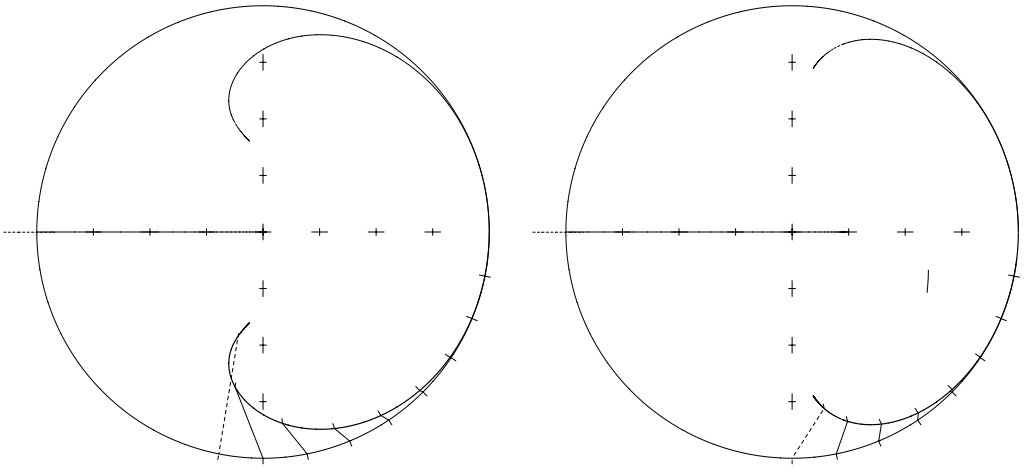

Fig. 9. (left) Characteristic roots for algorithm (2.42) with $\beta = 0$, but respecting both conditions (2.45). In comparison with the classical FB, Fig. 2, it is third-order accurate and has much smaller phase error. Its stability limit is $\alpha_{\max} = \sqrt{3}$, which is only 12% less than that of FB; (right) Same as on the (a), but $\beta = 0.3737076$, which satisfies (2.47) in addition to (2.45). This results in a fourth-order accurate scheme, the only one within this family.

$$(\beta - \gamma - 2\epsilon)\mathrm{i}\alpha^3 + \left(\frac{1}{12} - \frac{\beta}{2} + \frac{\gamma}{2} + \beta\gamma + 2\beta\epsilon\right)\alpha^4 + \left(\frac{1}{12} - \frac{\beta}{6} + \frac{\gamma}{6} + \frac{\epsilon}{3} - \beta\epsilon\right)\mathrm{i}\alpha^5 + \mathcal{O}(\alpha^6) = 0, \tag{2.44}$$

which leads to a set of conditions for coefficients β, γ, and ϵ. To ensure that the numerical algorithm is at least second-order accurate, one must respect the relation $\beta = \gamma + 2\epsilon$, which puts constraints of time-placement of rhs of the two equations of (2.42): if the rhs for ζ-equation is time centered at $t_n + (\frac{1}{2} - \delta)\Delta t$, then rhs for u-equation must be centered at $t_n + (\frac{1}{2} + \delta)\Delta t$ with the same offset δ. This property is respected for all algorithms discussed here, including the classical FB (2.13), which corresponds to $\beta = \gamma = \epsilon = 0$. To simultaneously cancel out $\mathcal{O}(\alpha^3)$ and $\mathcal{O}(\alpha^4)$ terms in (2.44), one must set

$$\gamma = \beta - 2\beta^2 - \frac{1}{6} \quad \text{and} \quad \epsilon = \beta^2 + \frac{1}{12}, \tag{2.45}$$

where β can still be arbitrary, giving raise to a monoparametric family of third-order accurate schemes. [8] Fig. 9, left, shows characteristic roots for the $\beta = 0$ algorithm, which is the simplest of this kind. Despite the similarity with the classical FB (shown in Fig. 2), the new algorithm has very different properties: its leading-order truncation term is dissipation-dominant, and the step multiplier is approximated with third-order accuracy. Detailed examination of properties of algorithms of this family within the range of $0 \leqslant \beta \leqslant 1/2$ reveals that their stability is always

[8] To derive these relationships we first exclude ϵ from α^4-term via substitution $\epsilon = (\beta - \gamma)/2$, and then solve for γ via β.

restricted by one of the computational modes leaving the unit circle in along the negative direction of real axis. Substituting (2.45) into (2.43), setting $\lambda = -1$, and solving it for α yields

$$\alpha_{\max} = \sqrt{3} \Big/ \sqrt{1 + \frac{\beta}{2} + 6\beta^3}, \tag{2.46}$$

which indicates that the stability range decreases with in crease of β, if one wishes to maintain third-order accuracy.

To eliminate all three leading terms in (2.44), in addition to (2.45), one must satisfy

$$\frac{1}{12} - \frac{\beta}{12} - \beta^3 = 0. \tag{2.47}$$

This has a unique solution $\beta = 0.3737076$. Correspondingly, $\gamma = -0.0722738$ and $\epsilon = 0.2229907$, which yields a fourth-order accurate algorithm, Fig. 9, right. As expected, it has small phase error, and in addition to that smaller dissipation relatively to one on the left. Detailed examinations of the algorithms from this family in the vicinity of $\beta = 0.3737076$ reveals that the small dissipation is achieved by a delicate cancellation of high-order truncation terms, which makes algorithms with β exceeding this value be asymptotically unstable (cf. $\beta = 1/2$, Fig. 10), although the instability is extremely weak: the maximum amplitude $|\lambda| = 1.0015$ at $\alpha \approx \pm 0.58$.

For practical reasons it is advantageous to set $\beta = 1/2$, hence to use AB2 time step for ζ-equation (2.42), because it naturally combines with the computation of other terms in shallow-water equations (Coriolis and advection). Although AB2 is still asymptotically unstable for terms of purely hyperbolic nature, the instability is much weaker than for forward Euler step, or $\beta < 1/2$-steps. To explore this possibility, we fix $\beta = 1/2$, and now treat e as a free parameter,

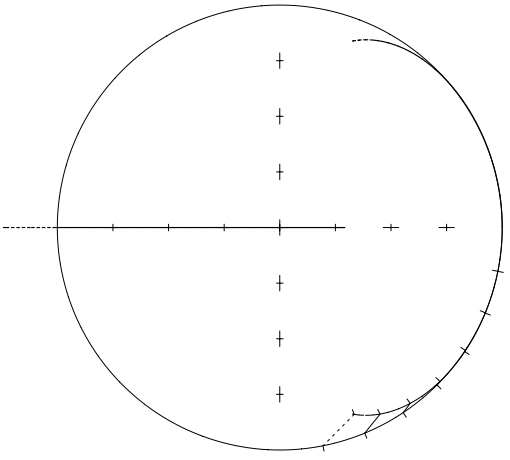

Fig. 10. Characteristic roots for algorithm (2.42) with $\beta = 1/2$, which corresponds to AB2 step for ζ-equation; γ, ϵ are set via (2.45). This algorithm has very weak asymptotic instability, $|\lambda| = 1.0015$ at $\alpha = \pm 0.58$.

but still respecting the property $\beta-\gamma-2\epsilon = 0$ to cancel $\mathcal{O}(\alpha^3)$ term in (2.44). Substitution of this into (2.43) transforms it into

$$\lambda^2 + \left[2 - \alpha^2\left(\frac{3}{2}\epsilon + \frac{3}{4}\right)\right]\lambda + 1 + \alpha^2\left(\frac{1}{2} - \frac{7}{2}\epsilon\right) - \left(\frac{1}{4} - \frac{5}{2}\epsilon\right)\alpha^2\lambda^{-1} - \frac{1}{2}\epsilon\alpha^2\lambda^{-2} = 0, \tag{2.48}$$

where we are interested in properties of algorithms in the vicinity of $\epsilon = 1/3$. Once again, stability is limited by one of the computational modes leaving the unit circle along negative real axis. Substituting $\lambda = -1$, we find that it occurs at $\alpha_{\max} = 1/\sqrt{2\epsilon}$, i.e., it decreases with ϵ. On the other hand, setting $\epsilon < 1/3$ results in asymptotic instability of the physical modes. Combination of these conditions defines $\epsilon = 1/3$ as yielding the largest possible stability range among all second-order accurate settings with $\beta = 1/2$. Overall it is more accurate than the classical FB: Fig. 10 vs. Fig. 2, and illustrates the principle that the order of accuracy of representing the phase speed and rate of dissipation of the propagating wave (ideally should none) can be made greater than the formal order accuracy of discretization of individual equations—the third- and the second-orders, respectively, in this case. However, its largest possible stability limit $\alpha_{\max} = \sqrt{3/2} \approx 1.2247$ is significantly less than 2 of FB. In addition to that, this algorithm still has a weak asymptotic instability of physical modes.

The next possibility is to use an AB3- and AM4-like time step for the ζ- and u-equations

$$\zeta^{n+1} = \zeta^n - \mathrm{i}\alpha\left[\left(\frac{3}{2} + \beta\right)u^n - \left(\frac{1}{2} + 2\beta\right)u^{n-1} + \beta u^{n-2}\right], \tag{2.49}$$

$$u^{n+1} = u^n - \mathrm{i}\alpha\left[\delta\zeta^{n+1} + (1 - \delta - \gamma - \epsilon)\zeta^n + \gamma\zeta^{n-1} + \epsilon\zeta^{n-2}\right].$$

Obviously it differs from (2.42) by the presence of β- and ϵ-terms associated with the use of prognostic variables at $n-2$ step. Setting $\beta = 5/12$ corresponds to an AB3 step for ζ. We will show that this choice is not optimal for the widest stability range; so for now β is viewed as an adjustable parameter.

Algorithm (2.49) has the characteristic equation

$$\begin{aligned}\lambda^2 &- \left[2 - \alpha^2\left(\frac{3}{2} + \beta\right)\delta\right]\lambda + 1 - \alpha^2\left[-\frac{3}{2} + 2\delta + \frac{3}{2}\gamma + \frac{3}{2}\epsilon - \beta(1 - 3\delta - \gamma - \epsilon)\right] \\ &- \alpha^2\left[\frac{1}{2} - \frac{\delta}{2} - 2\gamma - \frac{\epsilon}{2} + \beta(2 - 3\delta - 3\gamma - 2\epsilon)\right]\lambda^{-1} + \alpha^2\left[\beta(1 - \delta - 3\gamma) - \frac{\gamma}{2} + \frac{3}{2}\epsilon\right]\lambda^{-2} \\ &+ \alpha^2\left[\beta(\gamma - 2\epsilon) - \frac{\epsilon}{2}\right]\lambda^{-3} + \alpha^2\beta\epsilon\lambda^{-4} = 0.\end{aligned} \tag{2.50}$$

Similarly to (2.44), we substitute $\lambda = \mathrm{e}^{\mathrm{i}\alpha}$ and expand (2.50) in a Taylor series

$$\begin{aligned}&-\mathrm{i}\alpha^3\left[\frac{1}{2} - \delta + \gamma + 2\epsilon\right] + \alpha^4\left[\frac{5}{6} - \beta - \delta - \epsilon\right] + \frac{1}{6}\mathrm{i}\alpha^5[1 - \delta - 2\gamma - \epsilon + 6\beta(1 - \delta + \gamma + 2\epsilon)] \\ &+ \frac{1}{720}\alpha^6[-77 + 60\delta - 180\gamma - 480\epsilon + 60\beta(7 - 6\delta + 18\gamma + 48\epsilon)] + \mathcal{O}(\alpha^7) = 0.\end{aligned} \tag{2.51}$$

All terms of orders $\mathcal{O}(1)$, $\mathcal{O}(\mathrm{i}\alpha)$ and $\mathcal{O}(\alpha^2)$ cancel out for any choice of the coefficients β, γ, δ, and ϵ. To eliminate $\mathcal{O}(\alpha^3)$ terms in (2.51) we must satisfy

$$\delta = \frac{1}{2} + \gamma + 2\epsilon, \tag{2.52}$$

which in essence centers the rhs terms of u-equation (2.49) at $n + 1/2$. This condition will always be respected in the subsequent analysis in this section. Substituting (2.52) into (2.51) turns it into

$$\alpha^4\left[\frac{1}{3} - \beta - \gamma - 3\epsilon\right] + \frac{1}{2}\mathrm{i}\alpha^5\left[\frac{1}{6} + \beta - \gamma - \epsilon\right] + \alpha^6\left[-\frac{47}{720} - \frac{1}{6}\gamma - \frac{1}{2}\epsilon + \beta\left(\frac{1}{3} + \gamma + 3\epsilon\right)\right] + \mathcal{O}(\alpha^7) = 0. \tag{2.53}$$

At first we explore the possibility to achieve the highest order of accuracy. To eliminate both $\mathcal{O}(\alpha^4)$ and $\mathcal{O}(\alpha^5)$ terms in (2.53), we need to satisfy

$$\gamma = \frac{1}{4} - 2\epsilon \quad \text{and} \quad \beta = \frac{1}{12} - \epsilon, \tag{2.54}$$

which automatically sets $\delta = 3/4$ for any ϵ. In principle ϵ can be chosen from the condition of cancellation of $\mathcal{O}(\alpha^6)$ terms in (2.53) which, after substitution of (2.54), becomes

$$-\alpha^6\left[\frac{7}{120} + \frac{2}{3}\epsilon + \epsilon^2\right] + \mathcal{O}(\alpha^7) = 0. \tag{2.55}$$

This leads to

$$\epsilon = -\frac{1}{3} \pm \frac{\sqrt{190}}{60}. \tag{2.56}$$

As expected the resultant algorithm has extremely small phase and amplitude errors (Fig. 11, where we have chosen the "+" sign in (2.56) since the "–" results in a much smaller stability limit). But it is not attractive overall because of its modest stability limit of $\alpha_{\max} \approx 1$ (limited by one of the computational modes leaving unit circle at $\lambda = -1$) and it also has asymptotic instability of the physical modes. Here it should be noted that unlike for the quartic equation (2.43), there is no general analytical method for finding roots of a fifth- or sixth-order polynomial. However, the roots of (2.50) corresponding to physical modes are always isolated and can be found using an iterative Newton method. Once two physical roots are known, the power of the polynomial is reduced by two, and the remaining roots are found using conventional Cardano or Ferrari solutions.

Abandoning the cancellation of $\mathcal{O}(\alpha^6)$ terms while retaining both conditions in (2.54) yields asymptotically stable algorithms as long as $\epsilon > -0.03655$ (corresponding to $\alpha_{\max} = 1.187$). A further increase of ϵ results in an increase of the stability range until it reaches its maximum at $\alpha_{\max} = 1.727$ when $\epsilon = 0.083$; at this point the computational mode touches the unit circle (Fig. 12). This algorithm formally maintains fourth-order accuracy since it eliminates both $\mathcal{O}(\alpha^4)$ and $\mathcal{O}(\alpha^5)$ terms in (2.53).

Further relaxing the order of accuracy by abandoning the cancellation of $\mathcal{O}(\alpha^5)$ terms makes two parameters available for tuning while formally maintaining third-order accuracy. Thus we choose

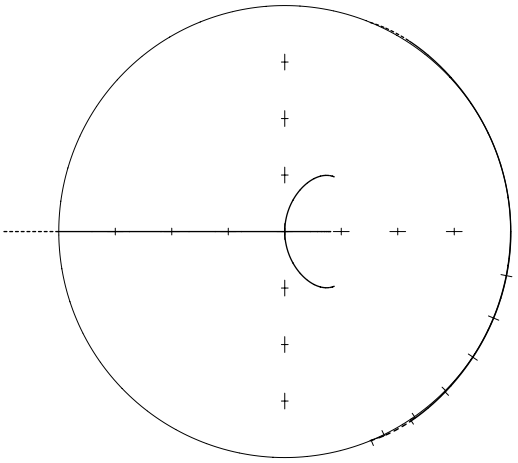

Fig. 11. Characteristic roots for algorithm (2.49) with coefficients selected to achieve the largest possible order of accuracy. It has asymptotic instability of the physical modes, (reaching $|\lambda| = 1.014$ at $\alpha \approx 1$) and $\alpha_{\max} = 1.014512$ limited by the computational mode leaving the unit circle at $\lambda = -1$.

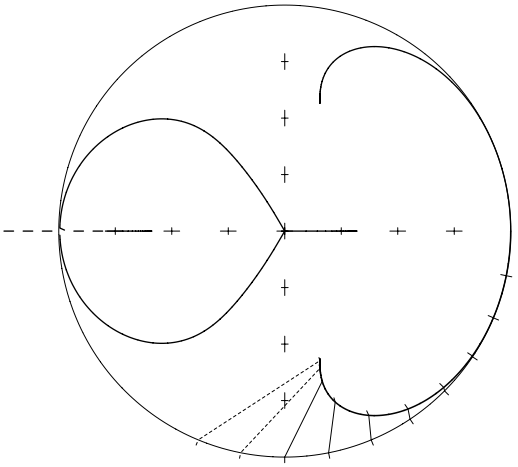

Fig. 12. $\epsilon = 0.083$, while maintaining (2.54) and (2.52). This yields the largest possible stability range $\alpha_{\max} = 1.727$ among the ϵ-family of fourth-order accurate schemes. The computational modes "touch" the unit circle at the place where they meet at $\lambda = -1$. It should be pointed out that despite the visual appearance, there are actually *four* computational modes here: two of them depart from the origin heading to the positive direction of real access, hence they are seen as a single line.

$$\gamma = \frac{1}{3} - \beta - 3\epsilon \tag{2.57}$$

and treat β and ϵ as adjustable parameters.

An obvious choice of $(\epsilon = 0, \beta = 5/12)$ results in $\gamma = -1/12$ and $\delta = 5/12$ that can be identified as the AB3 coefficients for ζ and AM3 coefficients for u. This has third-order accuracy for each

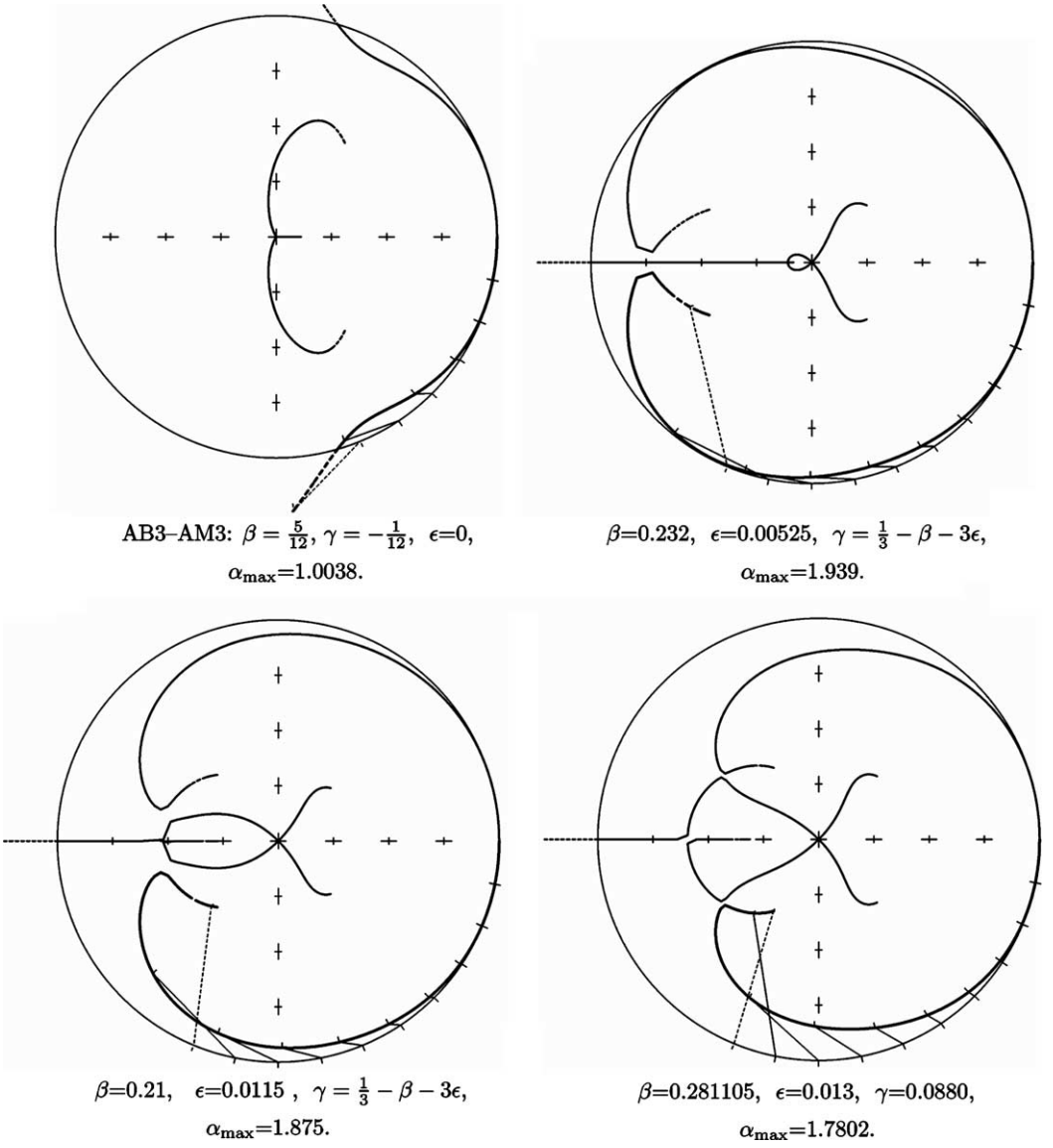

Fig. 13. Complex roots for generalized AB3–AM3 FB algorithms with different settings of coefficients. Although the choice with $\gamma \neq 1/12$ no longer maintains the third-order accuracy of the AM3 step for the ζ-equation taken alone, the phase speed of the wave system can still be approximated with third-order accuracy.

equation in (2.49) taken separately. Its stability limit is $\alpha_{\max} = 1.0039$, with the instability of the physical mode occurring first (Fig. 13, top left).

In this procedure we select β first, then for each beta we choose an ϵ to provide desirable properties of the resultant algorithm. The meaningful range for β is

$$\frac{1}{6} \leqslant \beta \leqslant \frac{5}{12} \tag{2.58}$$

with $\beta = 0$ correspond to AB2 and $\beta = 5/12$ to AB3 time steps for the ζ equation. Because of the advective properties of the nonlinear free-surface and tracer equations, it is also undesirable to choose $\beta < 1/6$ because of the weak instability of AB2 (Appendix A, Fig. 22). Setting $\beta = 0.281105$ corresponds to the best stability range for the AB2–AB3 family.

A two-parameter optimization for the maximum stability range on the β–ϵ plane results in $\beta = 0.232$ and $\epsilon = 0.00525$, hence $\alpha_{\max} = 1.939$ (Fig. 13, top right). This is only insignificantly smaller than for the classical FB algorithm (2.13), but the order of accuracy is now raised to third, and the phase lead of FB is eliminated for small values of α. Still, the new algorithm has the same drawback as the classical FB: the second half of its stability range (approx. $\alpha > \pi/3$) is too inaccurate (phase error) and does not provide sufficient damping (roots for physical modes touch the unit circle at $\alpha \approx \pm 2\pi/3$). A slightly modified choice of ($\beta = 0.21$, $\epsilon = 0.0115$) corrects the problem at the expense of a minor reduction of the stability range, $\alpha_{\max} = 1.875$ while maintaining third order accuracy (Fig. 13, bottom left).

It may be advantageous to choose $\beta = 0.281105$ (the largest possible stability limit among all AB2–AB3 family algorithms for a single equation; Appendix A) that leads to a simplification of the algorithm because separate coefficients for the advection terms in the nonlinear free-surface and tracer equations and for the pressure gradient in the momentum equations can be avoided. However, it is then no longer possible to maintain (2.57) and achieve a stability range comparable to 1.8, as in the two previous algorithms. A compromise choice of ($\beta = 0.281105$, $\gamma = 0.088$, $\epsilon = 0.013$) results in a slightly more dissipative algorithm (Fig. 13, bottom right). In a split-explicit model the fastest gravity waves are filtered out anyway, so this is the algorithm of choice for the barotropic mode.

3. Barotropic mode

In this section we address specific aspects of the barotropic mode as part of a coupled barotropic–baroclinic system.

3.1. Barotropic mode for a stratified ocean

In a split-explicit method à la Blumberg and Mellor, 1987, and Killworth et al. (1991), after the vertical integration of 3D momentum equations is performed, the Shallow Water Equation (SWE) pressure gradient (computed using the same free surface, ζ, and a constant reference density, ρ_0) is added and subtracted to it, resulting in

$$\frac{\partial \overline{U}}{\partial t} + \ldots = -gD\nabla_x\zeta + \{gD\nabla_x\zeta + \mathscr{F}\}, \tag{3.1}$$

where g is acceleration of gravity; $D = h + \zeta$ is total depth; $\overline{U} \equiv D\bar{u}$ is depth-integrated velocity (barotropic mass flux); $\nabla_x\zeta$ is a shorthand for $\partial\zeta/\partial x$; and

$$\mathscr{F} = -\frac{1}{\rho_0}\int_{-h}^{\zeta} \frac{\partial P}{\partial x}\,\mathrm{d}z \tag{3.2}$$

is the vertically integrated pressure gradient. The latter is a functional of the topography, free-surface gradient, and free surface itself, as well as the vertical distribution of density and its gradient,

$$\mathscr{F} = \mathscr{F}[\nabla_x\zeta, \zeta, \nabla_x\rho(z), \rho(z)]. \tag{3.3}$$

The term in curly brackets in (3.1) is interpreted as barotropic–baroclinic mode coupling. It is kept "frozen" during the barotropic time stepping while the first term on the right-hand side—the SWE-like term—is evolving in barotropic time.

The disadvantage of this approach is that after the barotropic time stepping is complete and the new free-surface field is substituted into the full baroclinic pressure gradient, its vertical integral will no longer be equal to the sum of the SWE-like pressure gradient (computed using new free surface) and the original coupling term (still based on the old free surface),

$$-gD\nabla_x\zeta' + \{gD\nabla_x\zeta + \mathscr{F}[\nabla_x\zeta, \zeta, \nabla_x\rho(z), \rho(z)]\} \neq \mathscr{F}[\nabla_x\zeta', \zeta', \nabla_x\rho(z), \rho(z)]. \tag{3.4}$$

$\zeta'$is the free-surface elevation after the sequence of barotropic time steps corresponding to one baroclinic time step. This type of discrepancy is usually known as a *mode-splitting* error.

The usual argument for the use of (3.1) is based on the fact that the difference is usually very small (since model density $\rho(x,y,z) = \rho_0 + \rho'(x,y,z)$ is always close to ρ_0). However, the primary concern here is that it affects the stability of the split-explicit model. The error (3.4) is discovered during the next baroclinic time step, and it plays the role of a disturbance causing the vertically integrated pressure gradient to be not in equilibrium with the barotropic mass flux. The barotropic time stepping drives the barotropic part toward an equilibrium, but it is disturbed again due to the redefinition of the vertically integrated baroclinic pressure gradient.

Higdon and Bennett (1996), and later (Higdon and de Szoeke, 1997), analyzed the stability of a coupled linearized system in an isopycnic vertical coordinate and show that, if nondissipative time stepping algorithms (LF or FB) are used for both modes, the resultant model is unavoidably unstable. [9] As a remedy they proposed an alternative definition of the barotropic mode in an isopycnic model that eliminates the mode splitting error, resulting in an effectively uncoupled (in linearized system) barotropic mode.

One may replace both $gD\nabla_x\zeta$ terms in (3.1) with

$$\frac{\partial\mathscr{F}}{\partial(\nabla_x\zeta)}\nabla_x\zeta + \frac{\partial\mathscr{F}}{\partial\zeta}\zeta, \tag{3.5}$$

where, for the purpose of partial differentiation, ζ and $\nabla_x\zeta$ are treated as independent variables and derivatives exist in variational sense. After this replacement, (3.4) becomes

$$\mathscr{F}[\nabla_x\zeta, \zeta, \ldots] + \frac{\partial\mathscr{F}}{\partial(\nabla_x\zeta)}\nabla_x(\zeta' - \zeta) + \frac{\partial\mathscr{F}}{\partial\zeta}(\zeta' - \zeta) \approx \mathscr{F}[\nabla_x\zeta', \zeta', \ldots]; \tag{3.6}$$

[9] This is evident from Fig. 3.1 from (Higdon and de Szoeke, 1997), and the associated discussion. In the case where the roots corresponding to the barotropic mode receive a phase increment during one baroclinic time step equal to the baroclinic roots + an integer times 2π, the barotropic mode is aliased to be in phase with the baroclinic mode. So any 2-way coupling between the modes (i.e., a perturbation due to the mode-splitting error) causes at least one root from each pair to go outside the unit circle.

i.e., the left-hand side formally appears as Taylor-series expansion of the right-hand side. This removes the dominant portion of the splitting error, and it also implies linearization with respect to the increment in ζ between baroclinic time steps (but it does not require smallness $\zeta/h \ll 1$).

We now show that without significant increase of the computational cost, one can take into account the nonuniform density field in the barotropic mode, resulting in a more accurate mode splitting method that is free of the shortcoming mentioned above and is suitable for use in a terrain-following model. Consider a fluid element bounded horizontally by two vertical lines corresponding to the locations of ζ_i and ζ_{i+1} and vertically by the free surface and bottom (Fig. 14, left). The horizontal component of the pressure-gradient force acting on this element is calculated by the integration of the pressure along the contour surrounding the fluid element (cf. Lin, 1997)

$$F_{i+\frac{1}{2}} = \int_{-h_i}^{\zeta_i} P(x_i, z)\,\mathrm{d}z - \int_{-h_{i+1}}^{\zeta_{i+1}} P(x_{i+1}, z)\,\mathrm{d}z - \int_{x_i}^{x_{i+1}} P(x, -h(x))\left[-\frac{\partial h(x)}{\partial x}\right]\mathrm{d}x = \mathcal{I}_i - \mathcal{I}_{i+1} - \mathcal{I}_{i+\frac{1}{2}}, \tag{3.7}$$

where we have neglected the effect of atmospheric pressure applied to the slopping surface of the ocean. In (3.7) $P(x,z)$ is the hydrostatic pressure,

$$P(x,z) = g\int_{z'}^{\zeta_i} \rho(x,z')\,\mathrm{d}z'. \tag{3.8}$$

Assuming a finite-volume approach to approximate (3.8) and eventually (3.7) at the discrete level, the barotropic pressure-gradient force at the velocity point $i+\frac{1}{2}$ is a function of the density in the vertical columns i and $i+1$, as well as the free-surface elevations ζ_i, ζ_{i+1}. Hence,

$$F_{i+\frac{1}{2}} = \mathscr{F}(\zeta_{i+1}, \bar{\rho}_{i+1,1}, \ldots, \bar{\rho}_{i+1,N}, \zeta_i, \bar{\rho}_{i,1}, \ldots, \bar{\rho}_{i,N}), \tag{3.9}$$

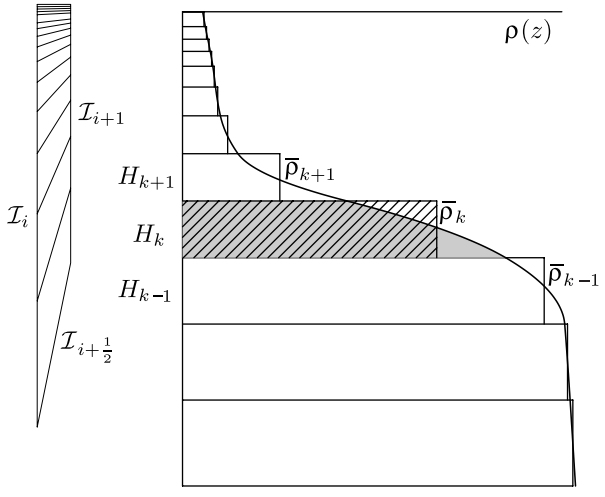

Fig. 14. (left) Fluid element showing placement of different terms in (3.7). (right) Reconstruction of the vertical density profile by parabolic segments (3.16): for each $k = 1, 2, \ldots, N$, $\bar{\rho}_k$ are density averaged over grid boxes H_k of a vertically nonuniform grid. The shaded area is the same as the area of the diagonally hatched rectangle.

where the structure of the functional $\mathscr{F}$ depends upon the discretization details of the baroclinic pressure gradient, typically involving nonlinear interaction of $\zeta_{i'}$ and $\overline{\rho}_{i',k}$ fields,

$$\frac{\partial^2 \mathscr{F}}{\partial \zeta_{i'} \partial \bar{\rho}_{i'',k}} \neq 0 \tag{3.10}$$

where $i', i'' = i, i+1$ in arbitrary combination and $k = 1, \ldots, N$. Consequently, one cannot split $\mathscr{F}$ into

$$\mathscr{F} \neq \mathscr{F}_1(\zeta_{i+1}, \zeta_i) + \mathscr{F}_2(\bar{\rho}_{i+1,1}, \ldots, \bar{\rho}_{i+1,N}, \bar{\rho}_{i,1}, \ldots, \bar{\rho}_{i,N}), \tag{3.11}$$

where $\mathscr{F}_2$ does not depend on ζ.

In the mode splitting technique proposed here, we assume that ζ is changing during the barotropic time stepping while the density values, $\{\bar{\rho}_{i,k}\}$, remain frozen and change only during the baroclinic time step. However, the nonlinear relation (3.9) holds in barotropic time. Of course, it would be prohibitively inefficient to recompute $\mathscr{F}$ in (3.9) at every barotropic step by vertical integration of the whole 3D pressure gradient. Instead, in each vertical column, once at every baroclinic time step before the barotropic mode calculation begins, we compute a vertically averaged density

$$\bar{\rho}(x) = \frac{1}{D} \int_{-h(x)}^{\zeta(x)} \rho(x,z)\, \mathrm{d}z \tag{3.12}$$

and a vertically averaged dynamical density,

$$\rho^*(x) = \frac{1}{\frac{1}{2}D^2} \int_{-h(x)}^{\zeta(x)} \left\{ \int_z^{\zeta(x)} \rho(x,z')\, \mathrm{d}z' \right\} \mathrm{d}z, \tag{3.13}$$

where $D \equiv D(x) = \zeta(x) + h(x)$ is the total thickness of the water column. Changing the integration variable to $\sigma = (z - \zeta)/D$ yields

$$\bar{\rho}(x) = \int_{-1}^{0} \rho(x,\sigma)\, \mathrm{d}\sigma, \quad \rho^*(x) = 2 \int_{-1}^{0} \left\{ \int_{\sigma}^{0} \rho(x,\sigma')\, \mathrm{d}\sigma' \right\} \mathrm{d}\sigma,$$

which implies that $\bar{\rho}$ and ρ^* are actually independent from ζ as long as density profile $\rho = \rho(\sigma)$ stays the same. Expressed in terms of $\bar{\rho}$ and ρ^*, (3.7) becomes

$$F_{i+\frac{1}{2}} = g \left\{ \frac{\rho_i^* D_i^2}{2} - \frac{\rho_{i+1}^* D_{i+1}^2}{2} + \int_{x_i}^{x_{i+1}} \bar{\rho} D \frac{\partial h}{\partial x}\, \mathrm{d}x \right\}. \tag{3.14}$$

This is a finite-volume discretization of the pressure-gradient term in the vertically integrated momentum equation

$$\frac{\partial}{\partial t}(D\overline{U}) + \cdots = -\frac{1}{\rho_0} g \left\{ \frac{\partial}{\partial x} \left(\frac{\rho^* D^2}{2} \right) - \bar{\rho} D \frac{\partial h}{\partial x} \right\} = -\frac{1}{\rho_0} g D \left\{ \rho^* \frac{\partial \zeta}{\partial x} + \frac{D}{2} \frac{\partial \rho^*}{\partial x} + (\rho^* - \bar{\rho}) \frac{\partial h}{\partial x} \right\}. \tag{3.15}$$

If $\rho^* \equiv \bar{\rho} \equiv \rho_0$, the right-hand side of (3.15) reverts back to the familiar SWE pressure-gradient term of (3.1), but in the general case nonuniformity of $\bar{\rho}$ and ρ^* leads to the appearance of

two extra terms that are baroclinic in nature. The problem therefore reduces to the search for a suitable method of calculation of $\bar{\rho}$ and ρ^* from the 3D density field $\{\bar{\rho}_{i,k}\}$ and an appropriate discretization of (3.14) and (3.15).

To address the first issue, consider, e.g., a piecewise-parabolic reconstruction of the vertical density profile from a set of discrete values $\{\bar{\rho}_k \mid k = 1, \ldots, N\}$ that is interpreted as a set of grid-box averages within each vertical vertical grid box H_k [10] (Fig. 14)

$$\rho(z') = \bar{\rho}_k + \frac{\rho_{k+\frac{1}{2}} + \rho_{k-\frac{1}{2}}}{H_k} z' + 6\left(\frac{\rho_{k+\frac{1}{2}} + \rho_{k-\frac{1}{2}}}{2} - \bar{\rho}_k\right)\left[\frac{z'^2}{H_k^2} - \frac{1}{12}\right]. \tag{3.16}$$

Here the local vertical coordinate z' spans within the grid box H_k, so that $-\frac{H_k}{2} \leqslant z' \leqslant +\frac{H_k}{2}$, and $\rho_{k\pm\frac{1}{2}} \equiv \rho(\pm\frac{H_k}{2})$ are the density values at at the upper and lower grid box interfaces, $z = \pm\frac{H_k}{2}$ computed via an appropriate reconstruction algorithm. Regardless of the details of computing $\rho_{k\pm\frac{1}{2}}$, (3.16) guarantees that

$$\frac{1}{H_k}\int_{-H_k/2}^{+H_k/2} \rho(z')\,\mathrm{d}z' \equiv \bar{\rho}_k \tag{3.17}$$

and leads to the discretization of vertically averaged density,

$$\bar{\rho}_i = \sum_{k=1}^{N} \bar{\rho}_{i,k} H_{i,k} \Bigg/ \sum_{k=1}^{N} H_{i,k}. \tag{3.18}$$

To compute ρ^* we note from (3.16) and (3.17) that the hydrostatic pressure in (3.7) can be expressed as a continuous function within each grid box H_k,

$$\begin{aligned} P(z') &= P_{k+\frac{1}{2}} + g\int_{z'}^{H_k/2} \rho(z'')\,\mathrm{d}z'' \\ &= P_{k+\frac{1}{2}} + gH_k\left\{\bar{\rho}_k\left[\frac{1}{2} - \frac{z'}{H_k}\right] + \frac{\rho_{k+\frac{1}{2}} - \rho_{k-\frac{1}{2}}}{2}\left[\frac{1}{4} - \frac{z'^2}{H_k^2}\right] + 2\left(\frac{\rho_{k+\frac{1}{2}} + \rho_{k-\frac{1}{2}}}{2} - \bar{\rho}_k\right)\left[\frac{z'}{4H_k} - \frac{z'^3}{H_k^3}\right]\right\}, \end{aligned} \tag{3.19}$$

where $P_{k+\frac{1}{2}}$ is the pressure at a depth corresponding to the interface between H_k and H_{k+1},

$$P_{N+\frac{1}{2}} = 0 \quad \text{and} \quad P_{k-\frac{1}{2}} = g\sum_{k'=k}^{N} \bar{\rho}_{k'}, H_{k'}, \quad k = 1, \ldots, N. \tag{3.20}$$

It can be verified from (3.19) that $P(-H_k/2) \equiv P_{k-\frac{1}{2}}$ that the pressure distribution and its first derivative are continuous across the grid box interfaces, (in the finite-volume approach, (3.20) is understood to be exact rather than a discrete approximation to the hydrostatic equation.)

Subsequent integration of (3.19) and (3.20) leads to

[10] For simplicity of notation, we dropped the horizontal index i in (3.16) and throughout the following part of this section. We use index k exclusively for the vertical coordinate while i and j refer to the horizontal coordinates. We will allow indices to disappear and reappear. In the particular context where k is the only present, all related operations are being performed within the vertical column independently from other columns.

$$\mathscr{I}_i = \int_{-h_i}^{\zeta_i} P_i(z)\,\mathrm{d}z = \sum_{k=1}^{N} \int_{-H_{i,k/2}}^{+H_{i,k/2}} P_i(z')\,\mathrm{d}z' = \sum_{k=1}^{N} H_{i,k}\overline{P}_{i,k}, \tag{3.21}$$

where

$$\overline{P}_{i,k} = P_{i,k+\frac{1}{2}} + \frac{1}{2} g H_{i,k}\left(\bar{\rho}_{i,k} + \frac{\rho_{i,k+\frac{1}{2}} - \rho_{i,k-\frac{1}{2}}}{6}\right) = \frac{P_{i,k+\frac{1}{2}} + P_{i,k-\frac{1}{2}}}{2} + g H_{i,k}\frac{\rho_{i,k+\frac{1}{2}} - \rho_{i,k-\frac{1}{2}}}{12} \tag{3.22}$$

is pressure averaged over $H_{i,k}$. This further leads to the definition of vertically averaged dynamical density as

$$\rho_i^* = \frac{1}{\frac{1}{2}\left(\sum_{k=1}^{N} H_{i,k}\right)^2} \cdot \sum_{k=1}^{N} H_{i,k}\left[\left(\sum_{k'=k+1}^{N} \bar{\rho}_{i,k'} H_{i,k'}\right) + \frac{1}{2} H_{i,k}\left(\bar{\rho}_{i,k} + \frac{\rho_{i,k+\frac{1}{2}} - \rho_{i,k-\frac{1}{2}}}{6}\right)\right]. \tag{3.23}$$

Using the identity

$$\sum_{k=1}^{N} H_{i,k}\left[\left(\sum_{k'=k+1}^{N} H_{i,k'}\right) + \frac{1}{2} H_{i,k}\right] \equiv \frac{1}{2}\left(\sum_{k=1}^{N} H_{i,k}\right)^2,$$

one can interpret (3.23) as just a weighted average. Furthermore, since

$$\sum_{k=1}^{N} H_{i,k} \equiv h_i + \zeta_i \equiv D_i, \tag{3.24}$$

(3.21) may be expressed as

$$\mathscr{I}_i = \frac{1}{2} g \rho_i^* D_i^2. \tag{3.25}$$

This is consistent with (3.13) and (3.14), as expected.

To approximate $\mathscr{I}_{i+\frac{1}{2}}$, we assume that D, $\bar{\rho}$, and h are linear functions of the horizontal coordinate between points x_i and x_{i+1}

$$\begin{aligned}\mathscr{I}_{i+\frac{1}{2}} &= g\int_{x_i}^{x_{i+1}} \left(\bar{\rho}_i \frac{x_{i+1} - x'}{\Delta x} + \bar{\rho}_{i+1}\frac{x' - x_i}{\Delta x}\right) \times \left(D_i \frac{x_{i+1} - x'}{\Delta x} + D_{i+1}\frac{x' - x_i}{\Delta x}\right)\frac{h_{i+1} - h_i}{\Delta x}\,\mathrm{d}x' \\ &= g\frac{(\bar{\rho}_i + \bar{\rho}_{i+1})(D_i + D_{i+1}) + \bar{\rho}_i D_i + \bar{\rho}_{i+1} D_{i+1}}{6} \times (h_{i+1} - h_i).\end{aligned} \tag{3.26}$$

After some algebra that repeats the transition from the first to the second line of (3.15) for the discrete formulation, (3.25) and (3.26) yield

$$\begin{aligned}F_{i+\frac{1}{2}} = {} & g\frac{D_i + D_{i+1}}{2} \cdot \frac{\rho_i^* + \rho_{i+1}^*}{2}(\zeta_i - \zeta_{i+1}) + g\frac{D_i^2 + D_{i+1}^2}{4}(\rho_i^* + \rho_{i+1}^*) \\ & + g\frac{D_i + D_{i+1}}{2} \cdot \frac{(\rho_i^* - \bar{\rho}_i) + (\rho_{i+1}^* - \bar{\rho}_{i+1})}{2}(h_i - h_{i+1}) \\ & + g\frac{(\bar{\rho}_{i+1} - \bar{\rho}_i)(D_{i+1} - D_i)(h_{i+1} - h_i)}{12}.\end{aligned} \tag{3.27}$$

The three terms on the first and second lines are obviously similar to the first, second, and third terms in the right-most part of (3.15), respectively. The term on the third line in (3.27) is on the order of $\mathcal{O}((\Delta x)^3)$ while all three preceding terms are $\mathcal{O}(\Delta x)$, so the former is negligible relative to the others as $\Delta x \to 0$.

In the case of $\zeta_i = \zeta_{i+1} = 0$, hence $D_i = h_i$ and $D_{i+1} = h_{i+1}$, (3.27) becomes

$$F^{(0)}_{i+\frac{1}{2}} = g(\rho^*_i - \bar{\rho}_i)\frac{h_i^2}{2} - g(\rho^*_{i+1} - \bar{\rho}_{i+1})\frac{h_{i+1}^2}{2} + g(\bar{\rho}_i - \bar{\rho}_{i+1})\frac{h_i^2 + h_i h_{i+1} + h_{i+1}^2}{6}. \tag{3.28}$$

Unlike the SWE pressure gradient, this does not vanish unless there is a spcial balance between the densities $\rho^*_i, \rho^*_{i+1}, \bar{\rho}_i, \bar{\rho}_{i+1}$ and the unperturbed thicknesses, h_i and h_{i+1} For example, if density is a linear function of depth, $\rho = \rho(z) = -\alpha z$ resulting in

$$\bar{\rho}_i = \frac{1}{h_i}\int_{-h_i}^{0} (-\alpha z)\,\mathrm{d}z = \frac{\alpha h_i}{2} \tag{3.29}$$

$$\rho^*_i = \frac{2}{h_i^2}\int_{-h_i}^{0}\int_{z}^{0} (-\alpha z')\,\mathrm{d}z' = \frac{\alpha h_i}{3}. \tag{3.30}$$

Then $F^{(0)}_{i+\frac{1}{2}}$ vanishes, as verified by direct substitution of these expressions into (3.28).

We therefore split (3.27) into

$$F_{i+\frac{1}{2}} = F^{(0)}_{i+\frac{1}{2}} + F'_{i+\frac{1}{2}}, \tag{3.31}$$

where

$$F'_{i+\frac{1}{2}} = -\frac{1}{2}g\Big\{(h_i + h_{i+1})(\rho^*_{i+1}\zeta_{i+1} - \rho^*_i\zeta_i) + \rho^*_{i+1}\zeta^2_{i+1} - \rho^*_i\zeta^2_i + (h_{i+1} - h_i)\left[(\rho^*_{i+1} - \bar{\rho}_{i+1})\zeta_{i+1} + (\rho^*_i - \bar{\rho}_i)\zeta_i + \frac{1}{3}(\bar{\rho}_{i+1} - \bar{\rho}_i)(\zeta_{i+1} - \zeta_i)\right]\Big\} \tag{3.32}$$

contains all the terms of (3.27) with ζ. The transition from (3.27)–(3.32) has no approximations.

We now summarize several properties of (3.28)–(3.32):

(i) The first line of (3.32) constitute a generalization of SWE pressure-gradient (3.1) with ρ^* playing role of "effective" density that is somewhat similar to the multiplicative split of (Bleck and Smith, 1990). In the uniform density case, $\rho^*_i = \bar{\rho}_i = \rho^*_{i+1} = \bar{\rho}_{i+1} = \rho_0$, it turns back to

$$F_{i+\frac{1}{2}} = -g\rho_0\frac{D_i + D_{i+1}}{2}(\zeta_{i+1} - \zeta_i), \tag{3.33}$$

as expected. The second line in (3.32) correspond to the response in pressure-gradient force to a perturbation of ζ in the presence of stratification and topography ($n \cdot b.$, these terms vanish if either the density field is uniform, or bottom is flat, or there is no free-surface perturbation). The appearance of this term is a fundamental property of stratified flows over topographic slopes and is related to the fact that it is no longer possible to split the motion into orthogonal vertical eigenmodes (including barotropic), even for waves (Munnich, 1993; Maas, 1997a,b). The full analysis of the consequences of this term is beyond the scope of the present study, but we point out

that it is a potential source of splitting error of the type analyzed and eliminated in (Higdon and de Szoeke, 1997).

(ii) For any given set of grid-box-averaged densities, $\bar{\rho}_{i,k}$, in a vertical column i, the values of $\bar{\rho}_i$ and ρ_i^* do not depend on the free-surface elevation, ζ_i. (1.9) and (1.10) imply that the disturbance of the free-surface field causes proportional stretching of all H_k,

$$H_{i,k} = H_{i,k}^{(0)} \cdot \left(1 + \frac{\zeta_i}{h_i}\right), \tag{3.34}$$

within each vertical column (here $H_{i,k}^{(0)}$ are the grid-box heights corresponding to an unperturbed free surface).

Consequently, replacement of $H_{i,k}^{(0)}$ with $H_{i,k}$ in (3.18) and (3.23) causes both the numerator and denominator to be multiplied by $(1 + \zeta_i/h_i)$ and $(1 + \zeta_i/h_i)^2$ respectively. This discrete-system property is consistent with a similar one for its continuous prototype, (3.12) and (3.13)); ultimately it guarantees the avoidance of splitting error of the kind in (3.4).

(iii) When the in situ density increases with depth, [11]

$$\rho_i^* \leqslant \bar{\rho}_i. \tag{3.35}$$

This implies that the effective barotropic pressure gradient (*i.e.*, the contribution due to ζ) of a stratified fluid is a systematically less than that for uniform density with the same ζ.

(iv) If the density field is a function only of depth (i.e., horizontally uniform stratification), the baroclinic pressure gradient should vanish. However, in order to make $F_{i+\frac{1}{2}}^{(0)} = 0$ in (3.28), there must be cancellation between its terms that can be achieved only by having a special relation between ρ_i^* and $\bar{\rho}_i$. Except for a few special choices of the density profile (constant, linear, or quadratic in z), this cancellation is not exact, but rather relies on the numerical accuracy of the integration method. This is often referred as *hydrostatic inconsistency* (Haney, 1991). The use of a high-order integration method does not offer an escape from inconsistency; it just reduces the error. For example, dropping the term,

$$gH_k \frac{\rho_{k+\frac{1}{2}} - \rho_{k-\frac{1}{2}}}{12}, \tag{3.36}$$

in (3.22) is equivalent to switching from a parabolic to a trapezoidal rule in integration of the hydrostatic equation. Because in stable stratification we expect all these terms to be negative, there is a systematic bias in ρ_i^* caused by this reduction of the order of accuracy.

3.2. Temporal averaging of the barotropic mode

The fluxes $U_{i+\frac{1}{2},j,k}$, $V_{i,j+\frac{1}{2},k}$, and $W_{i,j,k+\frac{1}{2}}$ in (1.14)–(1.17) are defined in *finite-volume* and *finite-time-step* senses (i.e., during a time interval Δt, the sum of fluxes across the moving facets of the grid element $\Delta\mathscr{V}_{i,j,k}$ produce a change in the volume of fluid inside that is equivalent to the difference of $\Delta\mathscr{V}_{i,j,k}^{n+1} - \Delta\mathscr{V}_{i,j,k}^{n}$; this in turn is determined by the free-surface equation advanced

[11] In the case of an incompressible fluid, this condition is equivalent to stable stratification. However, once compressibility effects are taken into account, it becomes less restrictive than stable stratification since the latter requires an increase of potential density with depth, rather than just in situ density.

in time with a different time-step size and time-stepping algorithm). Given the initial conditions for the free-surface elevation, ζ^n, and the vertically integrated velocity, $\overline{\mathbf{U}}^n$, at the time corresponding to the baroclinic time step n, as well as the baroclinic forcing functions (i.e., the vertically integrated right-hand side of the 3D momentum equations), the requirements on the 2D barotropic submodel are to compute (i) $\langle\zeta\rangle^{n+1}$ and $\langle\overline{\mathbf{U}}\rangle^{n+1}$ at the new baroclinic time step $n+1$, properly averaged to filter out and avoid aliasing of barotropic time scales not resolved by the baroclinic time step, and (ii) barotropic mass flux, $\langle\langle\mathbf{U}\rangle\rangle^{n+\frac{1}{2}}$, integrated over the barotropic time stepping, satisfying the slow-time, free-surface equation (1.20).

To fulfill task (i), we must choose an appropriate weighting shape function $\{\alpha_m\}$ (Fig. 15, top panel) that satisfies discrete normalization and centroid conditions,

$$\sum_{m=1}^{M^*} a_m \equiv 1, \quad \sum_{m=1}^{M^*} a_m \frac{m}{M} \equiv 1, \tag{3.37}$$

Here M denotes the barotropic–baroclinic mode-splitting ratio; m and n are fast and slow time indices (*n.b.*, it takes M barotropic steps to advance the barotropic mode for the time interval corresponding to one baroclinic step; $m=0$ corresponds to the baroclinic step n, while $m=M$ corresponds to the step $n+1$); M^* is the last index at which $\alpha_m \neq 0$, where $M \leqslant M^*$ to ensure that $\{a_m\}$ is time centered at $n+1$. Once $\{a_m\}$ is specified, we define the slow-time quantities (denoted by angle brackets)

$$\langle\zeta\rangle_{i,j}^{n+1} = \sum_{m=1}^{M^*} a_m \zeta_{i,j}^m, \quad \langle\overline{U}\rangle_{i+\frac{1}{2},j}^{n+1} = \sum_{m=1}^{M^*} a_m \overline{U}_{i+\frac{1}{2},j}^m, \quad \langle\overline{V}\rangle_{i,j+\frac{1}{2}}^{n+1} = \sum_{m=1}^{M^*} a_m \overline{V}_{i,j+\frac{1}{2}}^m, \tag{3.38}$$

where ζ^m, $\overline{U}^m$, and $\overline{V}^m$ are "instantaneous" barotropic variables. To satisfy the slow-time continuity equation (1.17), we have to construct another set of fast-time- averaged barotropic fluxes, $\langle\langle\overline{U}\rangle\rangle^{n+\frac{1}{2}}$ and $\langle\langle\overline{V}\rangle\rangle^{n+\frac{1}{2}}$, which are consistent with the change in sea level between the two consecutive slow-time steps,

$$\langle\zeta\rangle_{i,j}^{n+1} = \langle\zeta\rangle_{i,j}^{n} - \Delta t \cdot \mathrm{div}\langle\langle\overline{\mathbf{U}}\rangle\rangle_{i,j}^{n+\frac{1}{2}} \tag{3.39}$$

where

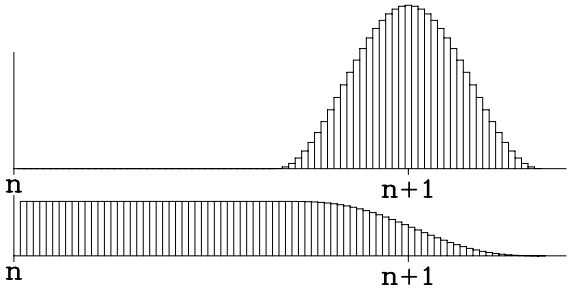

Fig. 15. Structure of the fast-time-averaging filter. (top) Primary weights, $\{a_m\}$, for computing $\langle\zeta\rangle^{n+1}$ and $\langle\overline{\mathbf{U}}\rangle^{n+1}$; and (bottom) corresponding secondary weights, $\{b_m\}$, to compute $\langle\langle\overline{\mathbf{U}}\rangle\rangle^{n+\frac{1}{2}}$. Small tickmarks symbolize the fast (barotropic) time steps, and large ones labeled by n and $n+1$ are the old and new baroclinic steps.

$$\mathrm{div}\langle\langle\overline{\mathbf{U}}\rangle\rangle_{i,j}^{n+\frac{1}{2}} = \frac{1}{\Delta_s\mathscr{A}_{i,j}}\left[\langle\langle\overline{U}\rangle\rangle_{i+\frac{1}{2},j}^{n+\frac{1}{2}} - \langle\langle\overline{U}\rangle\rangle_{i-\frac{1}{2},j}^{n+\frac{1}{2}} + \langle\langle\overline{V}\rangle\rangle_{i,j+\frac{1}{2}}^{n+\frac{1}{2}} - \langle\langle\overline{V}\rangle\rangle_{i,j-\frac{1}{2}}^{n+\frac{1}{2}}\right]. \tag{3.40}$$

Assume that the fast-time sea level is advanced by

$$\zeta^{m+1} = \zeta^m - \frac{\Delta t}{M}\cdot\mathrm{div}\overline{\mathbf{U}}^{m+\frac{1}{2}}, \quad \forall m = 1,\ldots,M^*, \tag{3.41}$$

where $\mathrm{div}\overline{\mathbf{U}}^{m+\frac{1}{2}}$ is similar to (3.40) except that it is applied to instantaneous barotropic fluxes, $\overline{U}_{i+\frac{1}{2},j}^{m+\frac{1}{2}}$ and $\overline{V}_{i,j+\frac{1}{2}}^{m+\frac{1}{2}}$, that are time-centered between fast steps m and $m+1$ as indicated by the half-integer index, $m+\frac{1}{2}$. Their relationship to the whole-indexed, barotropic prognostic variables, $\overline{\mathbf{U}}^m$, depends on the particular time stepping algorithm (Section 3.3). Successive summation of (3.41) with consecutive m yields

$$\zeta^m = \zeta^0 - \frac{\Delta t}{M}\sum_{m'=0}^{m-1}\mathrm{div}\overline{\mathbf{U}}^{m'+\frac{1}{2}}, \tag{3.42}$$

which after application of the time-averaging procedure (3.38) to the both sides turns into

$$\langle\zeta\rangle^{n+1} \equiv \sum_{m=1}^{M^*} a_m\zeta^m = \zeta^0 - \frac{\Delta t}{M}\cdot\mathrm{div}\sum_{m=1}^{M^*}\left[a_m\sum_{m'=1}^{m}\overline{\mathbf{U}}^{m'-\frac{1}{2}}\right],$$

where we have incremented the summation index m' by 1 relative to that in (3.42) to keep it within the range of index definition for $\{\alpha_m\}$, and moved the operation of horizontal divergence outside of the summation. To simplify the rhs, we substitute

$$\overline{\mathbf{U}}^{m'-\frac{1}{2}} \equiv \sum_{m''=1}^{M^*}\delta_{m'm''}\overline{\mathbf{U}}^{m''-\frac{1}{2}},$$

where $\delta_{m'm''} = \begin{cases} 1, & m' = m'' \\ 0, & \text{otherwise} \end{cases}$ is the Kronecker symbol, and rearrange the double summation above as

$$\begin{aligned}\sum_{m=1}^{M^*}\left[a_m\sum_{m'=1}^{m}\overline{\mathbf{U}}^{m'-\frac{1}{2}}\right] &= \sum_{m=1}^{M^*}\sum_{m'=1}^{m}\sum_{m''=1}^{M^*}a_m\delta_{m'm''}\overline{\mathbf{U}}^{m''-\frac{1}{2}} = \sum_{m''=1}^{M^*}\left[\overline{\mathbf{U}}^{m''-\frac{1}{2}}\sum_{m=1}^{M^*}\sum_{m'=1}^{m}a_m\delta_{m'm''}\right] \\ &= \sum_{m''=1}^{M^*}\left\{\overline{\mathbf{U}}^{m''-\frac{1}{2}}\times\left[\sum_{m=1}^{m''-1}a_m\underbrace{\sum_{m'=1}^{m}\delta_{m'm''}}_{=0,\ \text{since } m'<m''} + \sum_{m=m''}^{M^*}a_m\underbrace{\sum_{m'=1}^{m}\delta_{m'm''}}_{=1,\ \text{as } m'=m''\in\Sigma}\right]\right\} \\ &= \sum_{m''=1}^{M^*}\left[\overline{\mathbf{U}}^{m''-\frac{1}{2}}\left(\sum_{m=m''}^{M^*}a_m\right)\right]\end{aligned}$$

from which we see that by introducing a new set of weights,

$$bm' = \frac{1}{M}\sum_{m=m'}^{M^*}a_m, \quad \forall m = 1,\ldots,M^*. \tag{3.43}$$

we obtain

$$\langle\zeta\rangle^{n+1} = \zeta^0 - \Delta t \cdot \mathrm{div} \sum_{m'=1}^{M^*} b_{m'} \overline{\mathbf{U}}^{m'-\frac{1}{2}}, \tag{3.44}$$

(i.e., as a single weighted sum). The relationship between the two sets of weights is illustrated in Fig. 15. Once $\{a_m\}$ is chosen, the other set $\{b_m\}$ is uniquely determined by the the first set. Finally, we define

$$\langle\langle\overline{U}\rangle\rangle^{n+\frac{1}{2}}_{i+\frac{1}{2},j} = \sum_{m=1}^{M^*} b_m \overline{U}^{m-\frac{1}{2}}_{i+\frac{1}{2},j} \quad \langle\langle\overline{V}\rangle\rangle^{n+\frac{1}{2}}_{i,j+\frac{1}{2}} = \sum_{m=1}^{M^*} b_m \overline{V}^{m-\frac{1}{2}}_{i,j+\frac{1}{2}}, \tag{3.45}$$

to satisfy (3.39) as long as the integration of (3.41) starts with $\zeta^0 \equiv \langle\zeta\rangle^{\mathrm{n}}$. This implies that at every baroclinic step, after the barotropic time stepping is complete, the instantaneous values of ζ and $\overline{\mathbf{U}}$ are replaced with their fast-time averages in the sense of (3.38). These averaged values are used as initial conditions for the barotropic mode during the next baroclinic step.

After the completion of time stepping for the barotropic mode, the vertical coordinate system is updated via (1.10) using $\langle\zeta\rangle^{n+1}$. The new set of $H^{n+1}_{i,j,k}$ becomes available to complete the 3D time step. This is followed by computation of $u^{n+1}_{i+\frac{1}{2},j,k}$, $v^{n+1}_{i,j+\frac{1}{2},k}$ and their subsequent vertical integration. The integrals are subtracted from $\langle\overline{U}\rangle^{n+1}_{i+\frac{1}{2},j}$ and $\langle\overline{V}\rangle^{n+1}_{i,j+\frac{1}{2}}$, and the difference is divided by the depth corresponding to $\langle\zeta\rangle^{n+1}$ and the local topography h. The resultant correction term is then distributed uniformly throughout the vertical column to ensure that vertical integrals of updated $u^{n+1}_{i+\frac{1}{2},j,k}$ and $v^{n+1}_{i,+\frac{1}{2},k}$ are exactly the same as $\langle\overline{U}\rangle^{n+1}_{i+\frac{1}{2},j}$ and $\langle\overline{V}\rangle^{n+1}_{i,j+\frac{1}{2}}$. This completes the update of the 3D velocity field.

The update of the tracer fields begins with interpolation of 3D velocities between time steps n and $n+1$ to compute the mass fluxes $U^{n+\frac{1}{2}}$ and $V^{n+\frac{1}{2}}$ that are then corrected in the way just described to ensure that their vertical integrals are exactly equal to $\langle\langle\overline{U}\rangle\rangle^{n+\frac{1}{2}}$ and $\langle\langle\overline{V}\rangle\rangle^{n+\frac{1}{2}}$. This guarantees that after computation of the vertical velocity $W^{n+\frac{1}{2}}$ via (1.19) and substitution of H^n, H^{n+1}, $U^{n+\frac{1}{2}}$, $V^{n+\frac{1}{2}}$, and $W^{n+\frac{1}{2}}$ into (1.17), the later condition holds exactly. Tracer fluxes are then computed by an interpolation of the tracer values in space and in time to the placement of the corresponding velocity component that it is multiplied by (Section 4). The resultant time step for the tracer field is both conservative and constancy preserving.

3.3. Barotropic time stepping

Since the actual time-stepping algorithm for the barotropic mode is more sophisticated than (3.41), we need to show in more detail how to combine it with the averaging procedure. The barotropic equations are

$$\frac{\partial\zeta}{\partial t} + \mathrm{div}(D\bar{\mathbf{u}}) = 0 \tag{3.46}$$

$$\frac{\partial}{\partial t}(D\bar{\mathbf{u}}) + Df\mathbf{k}\times\bar{\mathbf{u}} = F(\zeta) + \cdots, \tag{3.47}$$

where $F(\zeta)$ is the barotropic pressure-gradient term (3.32). The dots in (3.47) denote slowly varying terms (i.e., baroclinic-mode, nonlinear, and viscous terms), most of which are kept constant

during the barotropic time stepping within one baroclinic step. Given the barotropic time step size, $\Delta t_* = \Delta t/M$, two nondimensional numbers are

$$\Delta t_* \sqrt{gh\left(\frac{1}{\Delta x^2}+\frac{1}{\Delta y^2}\right)} \quad \text{and} \quad f\Delta t_*. \tag{3.48}$$

These are respectively the Courant number for external gravity waves [12] and the ratio of the time step to an inertial period. For any reasonable choice of parameters, the former is much more restrictive than that the later (e.g., for a horizontal grid spacing of $\Delta x{=}\Delta y = 45\,\mathrm{km}$ and a characteristic depth $h = 5000\,\mathrm{m}$, it reaches unity at $\Delta t_* = 150\,\mathrm{s}$, while $f\Delta t_*$ does not exceed 0.01). Their contrast is even larger for finer spatial resolution. Consequently, the barotropic time step is stiffly limited by the phase speed of external gravity waves, while other factors—Coriolis and advection terms—impose no further restriction. In this case the efficiency of time stepping algorithms can be predicted from a linear theory: $\alpha_{\max} \approx 2.4$ for the predictor–corrector (2.38)–(2.41), and $\alpha_{\max} \approx 1.8$ for the generalized FB (2.49). In practice this translates into permissible Courant numbers (cf., (2.7) and (3.48), left) of 1.2 and 0.9, respectively. Since FB requires only one computation of the right-hand side of each equation per time step, it is 1.5 times more efficient than the predictor–corrector in the computational cost per unit simulation time.

The practical barotropic time-stepping algorithm is based on generalized FB algorithm (2.49) and utilizes temporal interpolation of prognostic variables, rather than complete right-hand side terms (cf., (2.38)–(2.41) and discussion thereafter). It begins with an AB3-extrapolation of free-surface elevation and barotropic velocities

$$\zeta^{m+\frac{1}{2}} = \left(\frac{3}{2}+\beta\right)\zeta^m - \left(\frac{1}{2}+2\beta\right)\zeta^{m-1} + \beta\zeta^{m-2}$$
$$\bar{\mathbf{u}}^{m+\frac{1}{2}} = \left(\frac{3}{2}+\beta\right)\bar{\mathbf{u}}^m - \left(\frac{1}{2}+2\beta\right)\bar{\mathbf{u}}^{m-1} + \beta\bar{\mathbf{u}}^{m-2}$$

with a subsequent flux computation

$$\overline{U}^{m+\frac{1}{2}} = D^{m+\frac{1}{2}}\bar{u}^{m+\frac{1}{2}}\Delta\eta, \quad \overline{V}^{m+\frac{1}{2}} = D^{m+\frac{1}{2}}\bar{v}^{m+\frac{1}{2}}\Delta\xi,$$

where $D^{m+\frac{1}{2}} = h + \zeta^{m+\frac{1}{2}}$. The free surface update,

$$\zeta^{m+1} = \zeta^m - \Delta t_* \mathrm{div}\overline{\mathbf{U}}^{m+\frac{1}{2}} \tag{3.49}$$

is followed by an update of the momentum equations,

$$\bar{\mathbf{u}}^{m+1} = \frac{1}{D^{m+1}}\{D^m\bar{\mathbf{u}}^m + \Delta t_*[F(\zeta') - D^{m+\frac{1}{2}}f\mathbf{k}\times\bar{\mathbf{u}}^{m+\frac{1}{2}} + \cdots]\}, \tag{3.50}$$

where $F(\zeta')$ uses backward-interpolated free surface,

$$\zeta' = \delta\zeta^{m+1} + (1-\delta-\gamma-\epsilon)\zeta^m + \gamma\zeta^{m-1} + \epsilon\zeta^{m-2}$$

involving the newly computed values ζ^{m+1}.

[12] The left expression in (3.48) is derived assuming a nonrotational ($f = 0$), constant-depth, shallow-water model discretized on a C-grid and using an FB time step.

$$D^m = h + \zeta^m \quad \text{and} \quad D^{m+1} = h + \zeta^{m+1}.$$

The spatial discretization of the Coriolis term $D^{m+\frac{1}{2}} f \mathbf{k} \times \bar{\mathbf{u}}^{m+\frac{1}{2}}$ ensures no contribution to the kinetic energy integral (Holland and Lin, 1975, see also Arakawa and Lamb, 1977, Eqs. (262), (263) and (281)–(285)) for the curvilinear-coordinate version: the velocity components, $(\bar{u}, \bar{v})$, are interpolated first to the location of ζ-points on the C-grid, where they multiplied by Coriolis parameter f (with advective cross-terms due to curvilinear coordinates added in), multiplied by total depth D, and the products are then interpolated further to the locations of the partner component. In all computations presented here, we use the parameter values, $\beta = 0.281105$, $\gamma = 0.088$, $\delta = 0.614$ and $\epsilon = 0.013$, specified at the end of Section 2. The computation of fast-time averaged barotropic variables, $\langle\zeta\rangle^{n+1}$ and $\langle\overline{\mathbf{U}}\rangle^{n+1}$, is done by (3.38) applied to (3.49) and (3.50). $\langle\langle\overline{\mathbf{U}}\rangle\rangle^{n+\frac{1}{2}}$ is computed by (3.45) just after $\overline{\mathbf{U}}^{m+\frac{1}{2}}$ becomes available.

3.4. Choice of filter shape

The analytical study in Higdon and de Szoeke (1997), reveals a probable scenario for computational instability in a split-explicit model where the eigenvalues [13] of the uncoupled baroclinic and barotropic modes coincide on the complex plane, and the perturbation due to inaccurate splitting and subsequent coupling moves some of the eigenvalues outside the unit circle. This coincidence is possible when the baroclinic mode gets a phase increment $\omega_k \Delta t$ while the barotropic mode gets $2\pi n + \omega_k \Delta\, t$ (i.e., aliasing). Temporal filtering of the barotropic variables excludes this possibility, but, as criticized by (Hallberg, 1997), it also results in additional numerical inaccuracy and requires an integration of the barotropic mode significantly beyond $n + 1$ in order to place the averaged values at $n + 1$. Although split-explicit models without temporal averaging of the fast mode are known to exist, their numerical stability is most likely attributable to some kind of implicit dissipation. For example, our time-splitting algorithm becomes equivalent to the method of averages (Nadiga et al., 1997) if we set $\{a_m\}$ to the delta function, $\alpha_m = \delta(M - m)$. This method relies on a Smolarkiewicz advection scheme that is sufficiently dissipative and stable when used in combination with a forward time step. Our experience with ROMS shows that the model becomes weakly unstable with a delta-function weighting. In contrast, (Hallberg, 1997), uses centered spatial differencing, no time-averaging, and a time-stepping algorithm that provides a controllable amount of dissipation through its truncation term within second-order accuracy. Our approach is to construct filters that resolve these issues.

Assuming $M \gg 1$, we neglect the truncation error in the barotropic time-stepping for the present analysis. Then an unfiltered Fourier component, ω_k, of the barotropic mode gets a phase increment $\alpha = \omega_k \Delta t$ in one baroclinic time step Δt. If the same component is subject to the weighted averaging in (3.38), its step multiplier is

$$\lambda(\alpha) = \int_0^{\tau*} \mathrm{e}^{-\mathrm{i}\alpha\cdot\tau} A(\tau)\, \mathrm{d}\tau, \tag{3.51}$$

[13] Eigenvalues are roots of the characteristic polynomial that are also Fourier component phase multipliers corresponding to one time step of the slow (baroclinic) mode.

where we have replace the discrete summation over m with an integral over τ(n.b., $A(\tau)$ is analogous to α_m, and τ plays the role of m/M). Ideally, $\lambda(\alpha) = e^{-\alpha}$ for small α, and $\lambda(\alpha) \to 0$ for large α. A Taylor series expansion for small α is

$$e^{-i\alpha\tau} = 1 - i\alpha\tau - \frac{\alpha^2\tau^2}{2} + \frac{i\alpha^3\tau^3}{6} + \cdots$$

leads to

$$\lambda(\alpha) = 1 - i\alpha - \frac{\alpha^2}{2}\mathscr{I}_2 + \frac{i\alpha^3}{6}\mathscr{I}_3 + \frac{\alpha^4}{24}\mathscr{I}_4 + \cdots, \tag{3.52}$$

where

$$\mathscr{I}_n = \int_0^{\tau*} \tau^n A(\tau)\,d\tau, \quad n = 2, 3 \ldots. \tag{3.53}$$

This takes into account that $\mathscr{I}_0 \equiv \mathscr{I}_1 \equiv 1$ due to the normalization and consistency conditions (3.37).

An analysis of (3.52) shows that any choice of a positive-definite shape function, $A(\tau)$, results in at most a first-order accuracy for the time stepping of the barotropic mode, i.e., $\lambda(\alpha)$ agrees with $e^{-i\alpha}$ only up to $\mathscr{O}(\alpha^2)$: using the identity, $\tau^2 \equiv (\tau - 1)^2 + 2\tau - 1$, we find that

$$\mathscr{I}_2 = \int_0^{\tau*} (\tau - 1)^2 A(\tau)\,d\tau + 2\mathscr{I}_1 - \mathscr{I}_0 = 1 + \epsilon, \tag{3.54}$$

where we have used the relation, $2\mathscr{I}_1 - \mathscr{I}_0 \equiv 1$. Unless $A(\tau)$ is a delta-function, $\delta(\tau - 1)$, the integrand is positive definite, and $\epsilon > 0$. Substitution of $\mathscr{I}_2$ into (3.52) leads to the appearance of ϵ as a coefficient in the leading-order truncation term at second order. $\epsilon > 0$ corresponds to numerical dissipation.

If (3.51) can be represented as

$$\lambda(\alpha) = \mathscr{R}(\alpha)e^{-i\alpha}, \tag{3.55}$$

where the response function $\mathscr{R}(\alpha)$ is real-valued, the resultant filter is nondispersive (i.e., it has zero phase error). The simplest way to achieve nondispersion is to choose a shape function symmetric about $\tau = 1$. Indeed, substitution of $\tau = 1 + \xi$, hence $A(\tau) = A(1 + \xi) = A(1 - \xi)$, into (3.51) leads to

$$\lambda(\alpha) = \int_{-\Delta\tau}^{+\Delta\tau} e^{-i\alpha(1+\xi)} \frac{A(1+\xi) + A(1+\xi)}{2}\,d\xi = e^{-i\alpha} = \int_{-\Delta\tau}^{+\Delta\tau} A(1+\xi)\cdot\cos(\alpha\xi)\,d\xi = \mathscr{R}(\alpha)e^{-i\alpha} \tag{3.56}$$

assuming that $A(\tau)$ is distinct from 0 only within the interval, $1 - \Delta\tau \leqslant \tau \leqslant 1 + \Delta\tau$, with $\Delta\tau \leqslant 1$.

For computational efficiency it is advantageous to use a nonsymmetric shape because it shortens the extent of integral portion beyond n+1. But we are interested in minimizing dispersion in the more general, nonsymmetric case. To do so we must construct $A(\tau)$ in such a way that it results in

$$\mathscr{R}(\alpha) = 1 - \epsilon\frac{\alpha^2}{2} + \theta\frac{\alpha^4}{24} - \chi\frac{i\alpha^5}{120} + \cdots, \tag{3.57}$$

where there are no $\mathrm{i}\alpha$ and $\mathrm{i}\alpha^3$-terms (their presence would respectively cause the zeroth-order error in phase speed and the second-order dispersive error). Hence, $\mathscr{R}(\alpha)$ is allowed to deviate from a real-valued function only in $\mathscr{O}(\mathrm{i}\alpha^5)$-terms. Multiplication of the above by $\mathrm{e}^{-\mathrm{i}\alpha}$ and Taylor expansion yields

$$\mathscr{R}(\alpha)\mathrm{e}^{-\mathrm{i}\alpha} = 1 - \mathrm{i}\alpha - (1+\epsilon)\frac{\alpha^2}{2} + (1+3\epsilon)\frac{\mathrm{i}\alpha^3}{6} + (1+6\epsilon+\theta)\frac{\alpha^4}{24} + \cdots. \tag{3.58}$$

In comparison with (3.52), this implies that

$$\mathscr{I}_3 = 3\mathscr{I}_2 - 2 \tag{3.59}$$

is the necessary condition to cancel out the $\mathscr{O}(\mathrm{i}\alpha^3)$ dispersive term.

Fig. 16 shows $\lambda(\alpha)$ for several filters in common use. Rectangular-shaped filters are characterized by the large dissipation for small values of α and relatively slow, oscillatory decay for large α in comparison with a smooth filter that has rapid decay after $\alpha = 2\pi$. As inaccurate as it may appear, flat averaging over $2\Delta t$ (Fig. 16, left top) results in

$$\lambda(\alpha) = \frac{\sin\alpha}{\alpha}\mathrm{e}^{-\mathrm{i}\alpha}, \tag{3.60}$$

which has a truncation error comparable to that of a weighted implicit time step,

$$\begin{aligned} \zeta^{n+1} &= \zeta^n - \mathrm{i}\alpha[\beta u^{n+1} + (1-\beta)u^n], \\ u^{n+1} &= u^n - \mathrm{i}\alpha[\beta\zeta^{n+1} + (1-\beta)\zeta^n] \end{aligned} \tag{3.61}$$

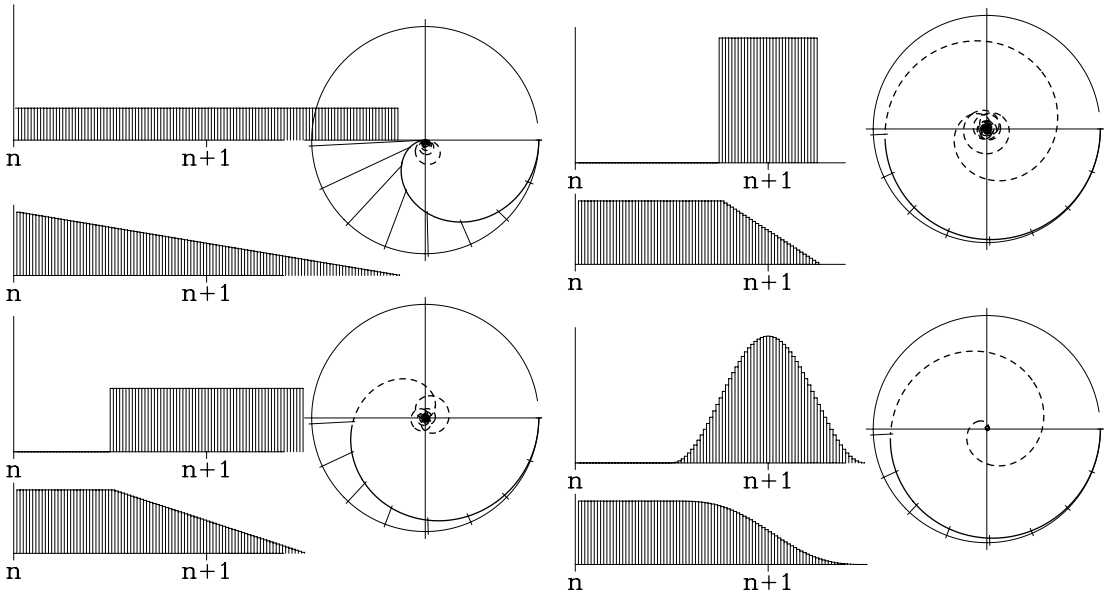

Fig. 16. Comparison of differently shaped filters. The left portion of each panel shows the primary and secondary weights (cf., Fig. 15). The circles on the right portion show the complex roots for the physical mode of the filtered barotropic mode. The solid curve turns to dashed when entering the aliasing range, $\omega\Delta t \geqslant \pi$. The roots must be well within the unit circle to prevent numerical instability.

with

$$\lambda(\alpha) = \frac{1 - \mathrm{i}\alpha - \beta(1-\beta)\alpha^2}{1 + \beta^2\alpha^2}, \tag{3.62}$$

and $\beta = 2/3$. This means that the commonly used Backward Euler (BE) time step ($\beta = 1$) is even less accurate for an implicit free-surface model. In contrast with both of these, the cos-shaped filter historically used in ROMS, [14]

$$A(\tau) = \begin{cases} 1 + \cos(2\pi(\tau - 1)), & \frac{1}{2} < \tau < \frac{3}{2}, \\ 0, & \text{otherwise} \end{cases} \tag{3.63}$$

is characterized by

$$\lambda(\alpha) = \frac{\sin\frac{\alpha}{2}\cdot \mathrm{e}^{-\mathrm{i}\alpha}}{\frac{\alpha}{2}(1 - \frac{\alpha^2}{4\pi^2})} = \mathrm{e}^{-\mathrm{i}\alpha}\begin{cases} 1 - \frac{(\pi^2-6)}{24\pi^2}, & \alpha \to 0, \\ \mathcal{O}(1/\alpha^3), & \alpha \to \infty \end{cases}$$

with removable singularities at $\alpha = \pm 2\pi$. Although it is still only first-order accurate, its leading-order dissipation, $\epsilon = (\pi^2 - 6)/(12\pi^2) \approx 0.0326$, is one-and-half orders of magnitude smaller than for the BE implicit scheme.

To further improve the temporal accuracy of the filtered barotropic mode, we define a shape function with some of the weights allowed to be negative

$$A(\tau) = A_0\left\{\left(\frac{\tau}{\tau_0}\right)^p\left[1 - \left(\frac{\tau}{\tau_0}\right)^q\right] - r\frac{\tau}{\tau_0}\right\}, \tag{3.64}$$

where p, q are parameters and A_0, τ_0 and r are then chosen to satisfy normalization, consistency, and second-order accuracy conditions,

$$I_n = \int_0^{\tau^*} \tau^n A(\tau)\,\mathrm{d}\tau = 1, \quad n = 0, 1, 2 \tag{3.65}$$

using Newton iterations. τ^* is the upper limit of τ with $A(\tau) \geqslant 0$. In practice we initially set [15]

$$\mathscr{A} = 1, r = 0 \quad \text{and} \quad \tau_0 = \frac{(p+2)(p+q+2)}{(p+1)(p+q+1)},$$

compute $A(\tau)$ via (3.64), normalize using (3.37), and adjust r iteratively to satisfy the n=2 condition of (3.65). The results are shown in Fig. 17, left side.

Alternatively to targeting $\mathscr{I}_2 = 1$, one might chose to satisfy (3.59) to minimize numerical dispersion. No choice of r eliminates both $\mathcal{O}(\alpha^2)$ and $\mathcal{O}(\mathrm{i}\alpha^3)$ truncation terms, but the r-term can reduce both of them relative to the $r = 0$ choice. Allowing negative weights in the left portion of the filter is also beneficial for computational efficiency because it shortens the required number of barotropic time steps. All filters on the left-hand side of Fig. 17 extend no farther than $\Delta t/4$ or $\Delta t/3$ beyond the baroclinic time step $n + 1$. A comparison with time-stepping schemes available for an

[14] A "raised" version of it, $A(\tau) = 1 + 0.85\cdot\cos(2\pi(\tau - 1))$, is known as a Hamming window (Hamming, 1989).

[15] This choice results in a center of gravity for $\{a_m\}$ at $m/M = 1$ in the limit $M \to \infty$, where $\tau = m/M$ in (3.64) with $r = 0$.

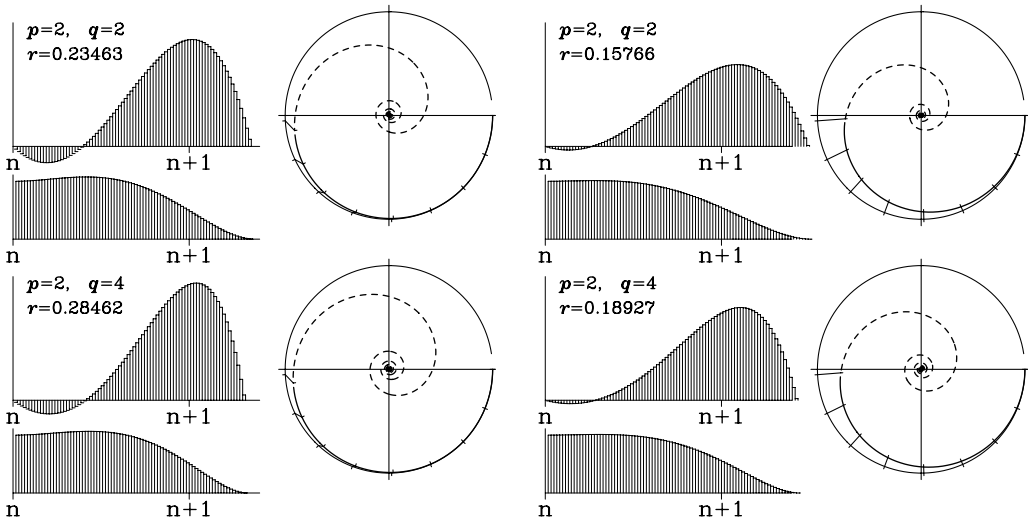

Fig. 17. Shape functions and corresponding step multipliers $\lambda(\alpha)$ for the filter (3.64) with different choices for p and q (left side) second-order accurate filters and (right side) optimized for minimal numerical despersion (3.59).

implicit free-surface model [16] shows that, with a proper choice of $A(\tau)$, the split-explicit model is inherently more accurate for time-resolved barotropic motions. The choice of parameters p and q controls the damping of the unresolved barotropic frequencies that determine the stability and robustness of the model. A complete quantitative analysis in a manner of (Higdon and de Szoeke, 1997), is beyond the scope of the present study; our practical experience indicates that filtering is generally required for stability (one cannot set α_m to a delta-function), but even the least dissipative filter in Fig. 17 result in a stable model for our applications without any need for explicit viscosity in the barotropic mode.

4. A hybrid predictor–corrector for the baroclinic time step

Because of the mathematical similarity of their equations, time-stepping algorithms for the baroclinic mode are generally similar to the barotropic ones. The differences arise from the necessity for a conservative, constancy-preserving algorithm for tracers. We will show how this makes it necessary to update the velocities before the tracers. Similar to (3.48), the allowed time step is limited mainly by internal gravity waves, but the contrast with the Coriolis restriction is not so dramatic. In addition, the advective Courant number is not expected to be very small; e.g., for typical oceanographic conditions, the phase speed of internal gravity waves may be 2.5 m/s, while the advection speed may be as large as 1 m/s. For coarse to moderate horizontal resolution, the baroclinic time step may be as large as 2 h, which is close to $1/f$ outside the tropics. Although the generalized FB algorithm is a clear favorite for the barotropic mode, we find that it more favorable to chose a predictor–corrector approach for the baroclinic mode.

[16] Since the implicit AM3 is only conditionally stable, these are limited to a weighted backward Euler step (cf. (3.61)).

Most oceanic models use a single-step algorithm for the 3D equations: either LF (MOM and its derivatives, MICOM, and POM) or AB3 (SPEM/SCRUM family). This choice has two weaknesses:

(i) Since the temperature and salinity are responsible for the stratification, hence the baroclinic pressure gradient, and since both momentum and tracer equations are advanced simultaneously for one time step, the momentum equations feel feedback from the changed tracer distribution only during the next step. Within the stiffest part of the system (i.e., propagation of internal gravity waves), the even-step velocity is coupled predominantly with the odd-step tracer field, and vice versa, while the odd–odd and even–even couplings are much weaker. In fact, for a linearized system and an LF time step, these two modes are completely independent. The use of AB3 mitigates this effect, but does not completely eliminate it.

(ii) In a free-surface model the grid-box heights, $H^{n+1}_{i,j,k}$, are set by the barotropic mode using an entirely different time-stepping algorithm. As the result, in the case of LF it is difficult to build a conservative and constancy-preserving advection scheme for tracers, because LF advances tracer fields from step $n-1$ to step $n+1$ with tracer fluxes computed at time step n, while the discrete continuity equation (1.17) relates $H^{n+1}_{i,j,k}$ with $H^{n}_{i,j,k}$ (instead of $H^{n-1}_{i,j,k}$), and the associated mass fluxes are time-centered at $n+\frac{1}{2}$. In the case of AB3, this problem may be addressed if a forward extrapolation of the pre-computed right-hand side for the tracer equations is replaced with an extrapolation of velocity components and a subsequent correction of their vertical averages, with a multiplication by the extrapolated tracers to compute tracer fluxes.

To make (1.14) and (1.17) consistent with their continuous counterparts with at least second-order accuracy, the mass fluxes, $(U_{i+\frac{1}{2},j,k},\ V_{i,j+\frac{1}{2},k},\ W_{i,j,k+\frac{1}{2}})$, and interfacial tracer values, $(\tilde{q}_{i+\frac{1}{2},j,k},\ \tilde{q}_{i,j+\frac{1}{2},k},\ q_{i,j,k+\frac{1}{2}})$, must be time-centered at $n+\frac{1}{2}$. Hence (1.17) becomes

$$H^{n+1}_{i,j,k}\Delta\mathscr{A}_{i,j} = H^{n}_{i,j,k}\Delta\mathscr{A}_{i,j} - \Delta t\left[U^{n+\frac{1}{2}}_{i+\frac{1}{2},j,k} - U^{n+\frac{1}{2}}_{i-\frac{1}{2},j,k} + V^{n+\frac{1}{2}}_{i,j+\frac{1}{2},k} - V^{n+\frac{1}{2}}_{i,j-\frac{1}{2},k} + W^{n+\frac{1}{2}}_{i,j,k+\frac{1}{2}} - W^{n+\frac{1}{2}}_{i,j,k-\frac{1}{2}}\right] \tag{4.1}$$

and (1.14) turns into

$$q^{n+1}_{i,j,k} = \left\{ q^{n}_{i,j,k}H^{n}_{i,j,k} - \frac{\Delta t}{\Delta\mathscr{A}_{i,j}}\left[\tilde{q}^{n+\frac{1}{2}}_{i+\frac{1}{2},j,k}U^{n+\frac{1}{2}}_{i+\frac{1}{2},j,k} - \tilde{q}^{n+\frac{1}{2}}_{i-\frac{1}{2},j,k}U^{n+\frac{1}{2}}_{i-\frac{1}{2},j,k} + \tilde{q}^{n+\frac{1}{2}}_{i,j+\frac{1}{2},k}V^{n+\frac{1}{2}}_{i,j+\frac{1}{2},k} - \tilde{q}^{n+\frac{1}{2}}_{i,j-\frac{1}{2},k}V^{n+\frac{1}{2}}_{i,j-\frac{1}{2},k}\right.\right.$$
$$\left.\left. + \tilde{q}^{n+\frac{1}{2}}_{i,j,k+\frac{1}{2}}W^{n+\frac{1}{2}}_{i,j,k+\frac{1}{2}} - \tilde{q}^{n+\frac{1}{2}}_{i,j,k+\frac{1}{2}}W^{n+\frac{1}{2}}_{i,j,k+\frac{1}{2}}\right]\right\} \Big/ H^{n+1}_{i,j,k}. \tag{4.2}$$

Here (4.1) is not to be interpreted as a method for computing $H^{n+1}_{i,j,k}$ but rather as a constraint imposed on the set of mass fluxes, $\left(U^{n+\frac{1}{2}},\ V^{n+\frac{1}{2}},\ W^{n+\frac{1}{2}}\right)$, satisfied by enforcing that the vertical integrals of $\left(U^{n+\frac{1}{2}},\ V^{n+\frac{1}{2}}\right)$ are equal to $\left(\langle\langle\overline{U}\rangle\rangle^{n+\frac{1}{2}},\ \langle\langle\overline{V}\rangle\rangle^{n+\frac{1}{2}}\right)$ defined by (3.45). Once this is satisfied, building a tracer advection scheme is just a matter of spatial interpolation of tracer variables to compute interfacial values and temporal extrapolation/interpolation to $n+\frac{1}{2}$ to achieve at least second-order accuracy and maintain numerical stability.

The simplest possibility is to extrapolate q forward in time before doing the spatial interpolation using a second- or third-order accurate Adams–Bashforth extrapolation rule for the right-hand side,

$$q^{n+\frac{1}{2}}_{i,j,k} = \left(\frac{3}{2}+\beta\right)q^{n}_{i,j,k} - \left(\frac{1}{2}+2\beta\right)q^{n-1}_{i,j,k} + \beta q^{n-2}_{i,j,k}. \tag{4.3}$$

$\beta = 0$ yields AB2, and $\beta = 5/12$ yields AB3 (Appendix A). This is preceded by a similar AB3-like update for the velocity field so that velocities at $n+1$ participate in interpolation to compute mass fluxes at $n+\frac{1}{2}$ as in (2.49), except that now ζ and u switch roles.

As an alternative to using local grid points in the previous time steps, one can chose an UTOPIA or COSMIC-like algorithm (Leonard et al., 1996). There is no need for forward extrapolation in time since only tracer values at time step n are used. This is potentially the most accurate approach because it uses a more compact stencil, and by its design the dispersive errors of time and space differencing compensate each other. However, the resultant schemes are unavoidably upstream-biased in all three spatial directions. This is undesirable for long-term simulations because of its vertical hyper-diffusion in the leading order truncation error, and this causes excessive artificial diapycnal mixing if temporal oscillations are present in the vertical velocity field (as is quite common in oceanic models). This algorithm is a single-step method, but its operational complexity is similar to a predictor–corrector's. Since a fully 3D UTOPIA algorithm is impractical, COSMIC is the most likely candidate. This algorithm includes computation of multi-dimensional finite-volume fluxes in each direction via successive 1D, nonconservative, advective updates in both transverse directions to get provisional tracer fields, after which the 1D QUICKEST algorithm is applied to compute fluxes.

The provisional field, $q^{n+\frac{1}{2}}$, also can be obtained by an *advective-form* predictor substep, where abandonment of the conservation principle is acceptable because $q^{n+\frac{1}{2}}$ are used only for the computation of fluxes in (4.2) and thereafter discarded. Conversely, since the set of mass fluxes satisfying (4.1) exists only between time steps n and $n+1$ (but not between $n-1$ and $n+\frac{1}{2}$), a conservative predictor substep cannot be made constancy preserving; hence, the resultant predictor–corrector algorithm will not be so either. A centered scheme for spatial derivatives in combination with an LF time step yields

$$q^{n+1,*}_{i,j,k} = q^{n-1}_{i,j,k} - 2\Delta t\left[\overline{u\delta_\xi q}^{\,\xi} + \overline{v\delta_\eta q}^{\,\eta} + \overline{w\delta_z q}^{\,z}\right]\Big|^{n}_{i,j,k}. \tag{4.4}$$

The symbols δ and overline denote differencing and interpolation in the direction designated by their sub- and superscripts (in principle, these operators can be higher- than-second order accurate), and u, v, and w are velocity components computed from the interface fluxes $U^n_{i+\frac{1}{2},j,k}$, $V^n_{i,j+\frac{1}{2},k}$ and $W^n_{i,j,k+\frac{1}{2}}$. Once $q^{n+1,*}$ becomes available, $q^{n+\frac{1}{2}}$ is computed using a three-point interpolation

$$q^{n+\frac{1}{2}}_{i,j,k} = \left(\frac{1}{2}-\gamma\right)q^{n+1,*}_{i,j,k} + \left(\frac{1}{2}+2\gamma\right)q^{n}_{i,j,k} - \gamma q^{n-1}_{i,j,k}, \tag{4.5}$$

after which a high-order spatial-interpolation scheme (described below) is used to compute the interfacial flux values, $\tilde{q}^{n+\frac{1}{2}}_{i+\frac{1}{2},j,k}$, $\tilde{q}^{n+\frac{1}{2}}_{i,j+\frac{1}{2},k}$, and $\tilde{q}^{n+\frac{1}{2}}_{i,j,k+\frac{1}{2}}$ in (4.2). Since $q^{n+1,*}$ is needed only to compute $q^{n+\frac{1}{2}}$, the operations (4.4) and (4.5) can be combined into a single step,

$$q^{n+\frac{1}{2}}_{i,j,k} = \left(\frac{1}{2}+2\gamma\right)q^{n}_{i,j,k} + \left(\frac{1}{2}-2\gamma\right)q^{n-1}_{i,j,k} - (1-2\gamma)\Delta t \quad \text{[same as in (4.4)]}. \tag{4.6}$$

Overall the combination of (4.6) and (4.2) is similar to LF–AM3 (with $\gamma = 1/12$) or LF–TR ($\gamma = 0$) predictor–corrector step (cf. (2.38)–(2.41) and Fig. 8).

Finally, instead of using the advective form of the tracer equation, the predictor step employs a *pseudo-compressible* algorithm to achieve constancy preservation. In this approach we compute two auxiliary grid-box height fields, $H^-_{i,j,k}$ and $H^+_{i,j,k}$, by stepping backward and forward in time,

$$H^{\pm}_{i,j,k} = H^n_{i,j,k} \mp \left(\frac{1}{2} - \gamma\right) \frac{\Delta t}{\Delta \mathscr{A}_{i,j}} [U^n_{i+\frac{1}{2},j,k} - U^n_{i-\frac{1}{2},j,k} + V^n_{i,j+\frac{1}{2},k} - V^n_{i,j-\frac{1}{2},k} + W^n_{i,j,k+\frac{1}{2}} - W^n_{i,j,k-\frac{1}{2}}]. \quad (4.7)$$

Then we perform a flux-divergent update of the tracer field, q, using an LF step combined with three-point interpolation (cf., (2.38)),

$$q^{n+\frac{1}{2}}_{i,j,k} = \left\{ \left[\left(\frac{1}{2} + 2\gamma\right) q^n_{i,j,k} + \left(\frac{1}{2} - 2\gamma\right) q^{n-1}_{i,j,k} \right] H^-_{i,j,k} - \frac{(1-2\gamma)\Delta t}{\Delta \mathscr{A}_{i,j}} \cdot [\tilde{q}^n_{i+\frac{1}{2},j,k} U^n_{i+\frac{1}{2},j,k} - \tilde{q}^n_{i-\frac{1}{2},j,k} U^n_{i-\frac{1}{2},j,k} + \tilde{q}^n_{i,j+\frac{1}{2},k} V^n_{i,j+\frac{1}{2},k} - \tilde{q}^n_{i,j-\frac{1}{2},k} V^n_{i,j-\frac{1}{2},k} + \tilde{q}^n_{i,j,k+\frac{1}{2}} W^n_{i,j,k+\frac{1}{2}} - \tilde{q}^n_{i,j,k-\frac{1}{2}} W^n_{i,j,k-\frac{1}{2}}] \right\} \Big/ H^+_{i,j,k}. \quad (4.8)$$

After this step $H^-_{i,j,k}$ and $H^+_{i,j,k}$ further do not participate in any computation and are discarded.

The construction of (4.7) and (4.8) makes the constancy preservation property clear: if $q^{n-1} \equiv q^n \equiv \text{const}$, then $q^{n+\frac{1}{2}}$ assumes the same constant value, regardless of the divergence of mass fluxes $U^n_{i+\frac{1}{2},j,k}$, $V^n_{i,j+\frac{1}{2},k}$ and $W^n_{i,j,k+\frac{1}{2}}$. However, since H^+ and H^+ have no relation to the actual grid-box height field by the barotropic mode (i.e., $H^{n+1}_{i,j,k}$ determined from $\langle\zeta\rangle^{n+1}_{i,j}$ via (1.10)), this update is not conservative. In fact, the use of the artificial divergence equation (4.7) just provides a way of trading in the conservation property in favor of constancy preservation, following the continuous identity,

$$\nabla(q\mathbf{u}) = (\mathbf{u} \cdot \nabla q) + q\nabla\mathbf{u} \quad (4.9)$$

and dropping the last term. At the same time, the pseudo-compressible time step is numerically similar to the conservative update during the corrector substep and therefore is preferable over the advective form (4.4).

Once the tracer concentration is available at the proper time, either n or $n + \frac{1}{2}$, it needs to be interpolated to grid-box interfaces to compute tracer fluxes. Three options are available in ROMS for doing so. The first is a centered, fourth-order-accurate interpolation (cf., Dietrich et al., 1997),

$$\tilde{q}_{i+\frac{1}{2},j,k} = \frac{-q_{i-1,j,k} + 7q_{i,j,k} + 7q_{i+1,j,k} - q_{i+2,j,k}}{12} \quad (4.10)$$

that can be expressed as a mid-point average enhanced by a curvature term

$$\tilde{q}_{i+\frac{1}{2},j,k} = \frac{q_{i,j,k} + q_{i+1,j,k}}{2} - \frac{\overline{\delta q}_{i+1,j,k} - \overline{\delta q}_{i,j,k}}{6}, \quad (4.11)$$

where $\overline{\delta q}_{i,j,k}$ and $\overline{\delta q}_{i+1,j,k}$ are averaged elementary differences

$$\overline{\delta q}_{i,j,k} = \frac{\delta q_{i-\frac{1}{2},j,k} + \delta q_{i+\frac{1}{2},j,k}}{2} \quad (4.12)$$

and $\delta q_{i+\frac{1}{2},j,k} = q_{i+1,j,k} - q_{i,j,k}$. The second option is to replace (4.12) with harmonic averaging (cf., Shchepetkin and McWilliams, 2003)

$$\overline{\delta q}_{i,j,k} = \frac{2\delta q_{i+\frac{1}{2},j,k}\delta q_{i-\frac{1}{2},j,k}}{\delta q_{i+\frac{1}{2},j,k} + \delta q_{i-\frac{1}{2},j,k}} \tag{4.13}$$

as long as $\delta q_{i+\frac{1}{2},j,k}$ and $\delta q_{i-\frac{1}{2},j,k}$ have the same sign, and $\overline{\delta q}_{i,j,k} = 0$ if their signs are different. In this case (4.11) has the property that the interpolated value, $\tilde{q}_{i+\frac{1}{2},j,k}$, is bounded by the values at the two neighboring points, $q_{i,j,k}$ and $q_{i+1,j,k}$, regardless of the values at the two extreme points of the stencil. Although this measure by itself does not strictly guarantee monotonicity preservation for the whole advection scheme, because the time stepping is done independently from spatial discretization, it tends to reduce spurious oscillations that arise with nonsmooth advected fields. The third option is an upstream-biased, parabolic interpolation,

$$\tilde{q}_{i+\frac{1}{2},j,k} = \frac{q_{i,j,k} + q_{i+1,j,k}}{2} - \frac{1}{6}\cdot\begin{cases} q''_{i,j,k}, & u_{i+\frac{1}{2},j,k} > 0, \\ q''_{i+1,j,k}, & u_{i+\frac{1}{2},j,k} < 0, \end{cases}$$

where

$$q''_{i,j,k} = q_{i+1,j,k} - 2q_{i,j,k} + q_{i-1,j,k}.$$

This results in a dissipatively dominant (i.e., hyper-diffusive) truncation error. The overall performance of the advection scheme is similar to that reported in (Farrow and Stevens, 1995). Vertical interpolation is done using either a centered fourth-order scheme or, preferably, an interpolation based on conservative parabolic splines as in (3.16) (Fig. 14). Use of an upstream-biased scheme in the vertical direction is avoided to diminish artificial diapycnal fluxes.

The time stepping for the momentum equations follows the same approach as above: a nonconservative (pseudo-compressible) predictor substep followed by a conservative corrector. Spatial discretization of the advective and Coriolis terms generally follows the framework of (Lilly, 1965), and (Mesinger and Arakawa, 1976), adapted for curvilinear horizontal grids. [17]

5. Time stepping the coupled baroclinic–barotropic system

We now summarize the time-stepping algorithm in ROMS, focusing on the discrete-time interactions between the modes (Fig. 18).

Stage 1: Compute the right-hand side for the 3D momentum equations at time step n (i.e., pressure-gradient, Coriolis, and advective terms only; no viscous terms are computed at this time). Apply this right-hand side to advance the 3D momenta using an LF step combined with a half-step, backward interpolation with AM3-like coefficients (the result is time-centered at $n + \frac{1}{2}$). Since at this moment no meaningful values of H^{n+1} are available and it is impossible to

[17] In essence this is done in POM (Blumberg and Mellor, 1987) and SCRUM (Song and Haidvogel, 1994), with the exception that mid-point averaging is replaced with high-order interpolations: third- (upstream-biased) or fourth-order (centered) schemes are applied in the horizontal directions and fourth-order or parabolic splines in the vertical.

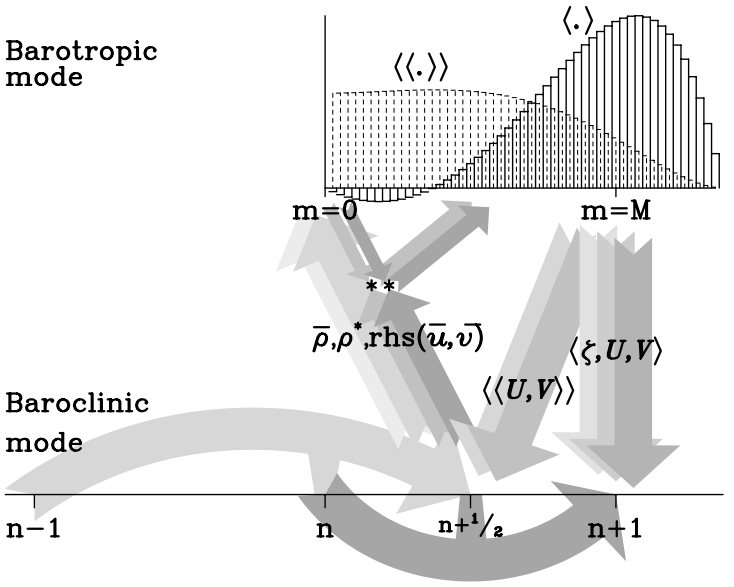

Fig. 18. Barotropic–baroclinic mode data exchange in ROMS: Curved horizontal arrows symbolize the predictor LF step combined with AM3 half-step-back interpolation of the result (light shading) and corrector substeps (dark shading). The four ascending arrows denote the 2-way, vertically averaged densities, $\bar{\rho}$ and ρ^*, and the vertically integrated right-hand side for 3D momentum equations [the last two meet with the two small arrows symbolizing computation of barotropic mode rhs from barotropic variables; so that asterisks (* *) denote the computation of baroclinic-to-barotropic forcing terms]. The five large descending arrows symbolize 2-way, fast-time-averaged barotropic variables for backward coupling. Each arrow originates at the time when the data is logically available, regardless of the temporal placement of the corresponding variable.

satisfy exactly the discrete continuity equation, use the artificial continuity equation (i.e., the pseudo-compressible algorithm). In addition to that, because this predictor step violates CFL for the barotropic mode and no meaningful barotropic mass fluxes time-centered at $n+\frac{1}{2}$ are available yet, set the vertical averages for the newly computed fluxes back to $\langle\overline{\mathbf{U}}\rangle^n$.

Stage 2: Advance the tracer variables in a similar manner with a pseudo-compressible LF step combined with an AM3 interpolation, placing the resultant values at $n+\frac{1}{2}$. (This algorithm is constancy preserving, but not conservative, which is acceptable because the resultant tracer values at $n+\frac{1}{2}$ are used only for computation of advective fluxes during the subsequent corrector step. The same comment applies to the predictor update for the momentum equations at Stage 1).

Stage 3: Compute the right-hand side for the 3D momentum equations (*i.e.,* pressure-gradient, Coriolis, and advective terms) from the mass fluxes and tracers (via density) at $n+\frac{1}{2}$ and the lateral viscosity terms from the old-step velocities, $\mathbf{u}^n$. Vertically integrate everything and also compute and store vertically averaged densities, $\bar{\rho}_i$, ρ_i^*, using (3.18)–(3.23) time-centered at $n+\frac{1}{2}$. Apply the right-hand side to the 3D momentum variables, but do not finalize the time step since H^{n+1} and $\langle\overline{\mathbf{U}}\rangle^{n+1}$ are not available yet.

Stage 4: Compute the right-hand side terms for the barotropic mode from barotropic variables using (3.32) for the pressure gradient and subtract it from the corresponding vertical integrals of the 3D right-hand side computed in Stage 3 (i.e., convert them into baroclinic-to-barotropic

forcing terms). [18] Advance the barotropic variables by M^* time steps (slightly beyond the baroclinic time step $n+1$, depending on the shape of the fast-time filter), performing a 2-way, fast-time averaging of barotropic variables on the way. (The baroclinic forcing terms are kept constant during this procedure, but the barotropic pressure-gradient terms are recomputed by (3.32) with participation of $\bar{\rho}_i$ and ρ_i^* at every barotropic step). Once this is complete, update the vertical coordinate system, $\{z_{i,j,k},\ z_{i,j,k+\frac{1}{2}},\ H_{i,j,k}\}^{n+1}$, to be consistent with $\langle\zeta\rangle^{n+1}$.

Stage 5: Finalize the computation of the 3D mass fluxes begun in Stage 3 using the now available H^{n+1}, and set the vertical average to $\langle\overline{\mathbf{U}}\rangle^{n+1}$ from the barotropic mode.

Stage 6: Interpolate the 3D velocity components back in time to $n+\frac{1}{2}$ using a combination of the new time-step values (from Stage 5), values from the predictor step (Stage 4), and old-time step values. (This introduces forward–backward feedback between the momentum and tracer equations as in (2.38)–(2.41) but with the roles of u and ζ switched.) Set the vertical average of the resultant fields to $\langle\langle\overline{\mathbf{U}}\rangle\rangle^{n+\frac{1}{2}}$. Use the resultant velocity field and tracers at $n+\frac{1}{2}$ to compute the tracer fluxes and advance the tracers to $n+1$. (This step is both conservative and constancy preserving.)

6. Conclusions

We have designed a robust computational kernel for a split-explicit, terrain-following-coordinate oceanic model, ROMS.

We use time-stepping algorithms with forward–backward feedback between the pairs of variables responsible for gravity wave propagation (surface or internal) that combine an extended range of stability with the temporal accuracy of the best known algorithms: in effect, generalizing the FB schemes to higher orders of accuracy. Among these schemes, the Euler step (2.13) can be viewed as the first member of the family, AB2–AM3 (2.42) as the second, and AB3–AM4 (2.49) as the third. A similar classification applies to the modified RK2–LF–AM3 family.

Although we use LF–AM3-type predictor–corrector algorithms for the baroclinic mode (generally three-time-level schemes, motivated by comparative linear stability analysis for wave motions), it should be noted that the predictor substep is only needed to obtain provisional variables time-centered at $n+\frac{1}{2}$ for subsequent computation of right-hand side terms subsequently used in the corrector substep. Mode-splitting occurs during the corrector only, which is always a two-time-level scheme in our approach. In this respect our method differs from POM (perhaps the most widely used σ-coordinate model) and is more similar to ones advocated by (Nadiga et al., 1997), and (Higdon, 2002), both of which are RK2-type predictor–corrector algorithms that seem to be a more natural choice for layered models because of the need for positive-definite advection with vanishing layer thicknesses.

[18] There is no need to compute the $F^{(0)}$-part of the barotropic pressure gradient defined by (3.28) because it is already accounted for in the vertical integral of the 3D right-hand side. Since it does not depend on ζ, it remains constant during barotropic time stepping. Because of the "add–subtract" procedure for baroclinic-to-barotropic forcing, this term identically cancels out when the forcing terms are added back to the barotropic right-hand side.

We redefine the barotropic mode equations to account for the nonuniform density field to reduce the mode-splitting error—in essence following the methodology of Higdon and de Szoeke (1997), but here in the context of terrain-following coordinates. The pressure-gradient force for the barotropic mode is derived as a vertical integral of 3D pressure-gradient due to fluctuations in the free-surface elevation, ζ. This ensures accuracy of the mode splitting even in the presence of topography. The computationally efficient implementation of this method involves a special 2-way vertical averaging procedure for density field once per baroclinic time step.

We assure simultaneous conservation and constancy preservation properties for tracers in the evolving coordinate system due to changes in ζ. This is accomplished by 2-way temporal averaging of the barotropic finite-volume fluxes to ensure that the 3D discrete continuity equation holds exactly between two subsequent baroclinic steps even as the whole vertical system of coordinates changes with ζ.

We incorporate a temporal weighted-averaging of the barotropic mode that allows an accurate representation of the barotropic motions resolved by the baroclinic time step (e.g., tides and barotropic Rossby waves).

Finally, our treatment of computationally expensive processes that are not critical for numerical stability (e.g., lateral and vertical mixing parameterizations) is placed outside the main predictor–corrector procedure to mitigate their computational cost.

Built around this kernel, ROMS has been applied to several oceanographic studies of basin-scale and coastal circulation (e.g., Haidvogel et al., 2000; Marchesiello et al., 2003). It has been verified to allow the time step sizes and mode splitting ratios summarized in Table 1 for these configurations. ROMS allows significant increases of the time step size relative to its terrain-following prototypes (SCRUM/SPEM and POM), as well as to other z-(MOM, POP) and isopycnic-coordinate (MICOM) models that use simpler time-stepping algorithms (e.g., single step, synchronous, mostly LF or AB3 for SCRUM). Furthermore, our analysis and practical experience indicate that this gain is achieved without major increase of computational cost due to the predictor–corrector algorithm, in part because most of the computationally expensive processes are still computed only once per time step. Nor do we observe any degradation in the quality of our solutions due to the increased time-step size close to theoretical limits of stability.

Table 1
Permissible time step sizes and mode splitting ratios for several practical applications of ROMS

Configuration	Grid size	Resolution (deg or km)	Time step (s)	Mode splitting ratio	Primary time step limitation by
Atlantic DAMEE	$128 \times 128 \times 20$	0.75°	8640	60 (Gen. FB)	Coriolis force
Atlantic DAMEE	$256 \times 256 \times 20$	0.375°	5760	92 (Gen. FB)	Coriolis/internal
Pacific	$384 \times 224 \times 30$	0.5°	7200	78 (Gen. FB)	Coriolis force
US West Coast	$83 \times 168 \times 20$	15 km	2880	50 (LF–TR)	Internal waves
US West Coast	$126 \times 254 \times 20$	10 km	2160	60 (LF–TR)	Internal waves
Monterey Bay	$93 \times 189 \times 20$	5 km	960	60 (LF–TR)	Internal waves

"(Gen. FB)" and "(LF–TR)" in the Mode Splitting Ratio column indicate the type of time stepping algorithm used for the barotropic mode.

Acknowledgment

This study was supported by grant N00014-02-1-0236 from the Office of Naval Research.

Appendix A. Simple time-stepping algorithms

One of the most commonly used time-stepping algorithms is Leap-Frog (LF) accompanied by an Asselin filter (Asselin, 1972). For (2.3), it may be written as

$$q^{n+1,*} = q^{n-1} - 2\mathrm{i}\alpha \cdot q^{n,*} \tag{A.1}$$

followed by

$$q^{n} = \epsilon q^{n+1,*} + (1-2\epsilon) q^{n,*} + \epsilon q^{n-1}, \tag{A.2}$$

where $\alpha \equiv \omega \Delta t$; $q^{n+1,*}$ and $q^{n,*}$ are "preliminary" values of q^{n+1} and q^{n} and $\epsilon \geqslant 0$ is an adjustable parameter. Substitution of $q^{n+1,*}$ from (A.1) into (A.2) yields

$$q^{n,*} = \frac{q^{n} - 2\epsilon q^{n-1}}{1 - 2\epsilon - 2\epsilon\mathrm{i}\alpha}. \tag{A.3}$$

Since a similar relationship exists between $q^{n+1,*}$ and q^{n+1}, one can exclude the preliminary variables from (A.1),

$$\frac{q^{n+1} - 2\epsilon q^{n}}{1 - 2\epsilon - 2\epsilon\mathrm{i}\alpha} = q^{n-1} - 2\mathrm{i}\alpha \cdot \frac{q^{n} - 2\epsilon q^{n-1}}{1 - 2\epsilon - 2\epsilon\mathrm{i}\alpha}, \tag{A.4}$$

and further rewrite it as

$$q^{n+1} = (1-2\epsilon) q^{n-1} + 2\epsilon q^{n} - 2\mathrm{i}\alpha (q^{n} - \epsilon q^{n-1}) \tag{A.5}$$

(i.e., a single-step version of (A.1) and (A.2)). This leads to a characteristic eigenvalue equation,

$$\lambda^2 + 2(\mathrm{i}\alpha - \epsilon)\lambda - 1 + 2\epsilon(1 - \mathrm{i}\alpha) = 0 \tag{A.6}$$

with roots (cf., Eq. (12) in Asselin, 1972),

$$\lambda_{\pm} = -\mathrm{i}\alpha + \epsilon \pm \sqrt{(1-\epsilon)^2 - \alpha^2} \tag{A.7}$$

and the stability limit

$$|\ \alpha_{\max}(\epsilon)\ | = 1/\sqrt{1 + 2\epsilon - \epsilon^2} \approx 1 - \epsilon. \tag{A.8}$$

This approximation is valid for $\epsilon \ll 1$. A Taylor series analysis of (A.5) leads to a modified equation

$$\frac{\partial q}{\partial t} = -\mathrm{i}\omega q - \frac{\epsilon \Delta t \omega^2 q}{2 - 2\epsilon + \epsilon\mathrm{i}\omega\Delta t} + \mathcal{O}\left((\omega\Delta t)^2\right), \tag{A.9}$$

indicating that the formal accuracy drops to first-order if $\epsilon > 0$ and the leading-order truncation term is dissipative. An Asselin filter introduces the desired damping of the LF computational mode at the expense of a reduced stability range, some dissipation of the physical mode, and a

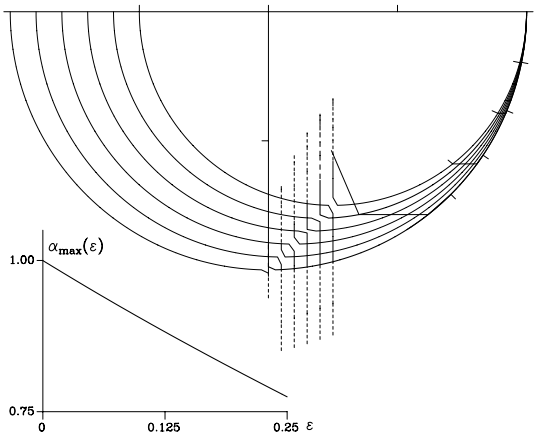

Fig. 19. Complex roots for the LF–Asselin Filter time-stepping algorithm for $\epsilon = 0$, 0.05, 0.1, 0.15, 0.2, and 0.25. The curves corresponding to $\epsilon = 0$, and 0.2 are highlighted. The presence of ϵ terms in (A.7) moves roots strictly along the real axis relative to unfiltered LF roots. ϵ does not affect the imaginary part of $\lambda_{\pm}$. as long as the expression under the radical is positive. Because of this feature, an Asselin filter causes an additional phase-lead error to an already forward-dispersive LF. The lower-left portion shows the dependency of the stability limit $\alpha_{\max}$ on ϵ (cf. (A.8)).

further increase of the phase-lead error of already strongly dispersive LF (Fig. 19). For example, with $\alpha = \frac{\pi}{4}$ and a typical value of $\epsilon = 0.1$, adding an Asselin filter almost doubles the LF phase error.

The properties of an LF–Asselin filter time step are well known. Durran (1991), provides a comprehensive review of this and other commonly used time-stepping algorithms for the first-order hyperbolic problem (2.1). This analysis includes Taylor series expansions for both phase and amplitude errors. However, it is instructive for the algorithmic decisions presented in this paper to trace the location of the amplification factors on the complex plane since this indicates the limits for each method, while the usual analysis of truncation error based on Taylor series expansion does not provide this information. The results are shown in Fig. 20. Even a brief glance at this figure indicates the existence of a variety of algorithms potentially more attractive than the LF–Asselin filter. It also shows that Runge–Kutta (RK) and predictor–corrector methods are generally more accurate than single-step methods. They also require more computational effort because the right-hand side is computed more than once per time step. In fact, these types of algorithms can be viewed as combinations of simple single-stage methods arranged so that the leading-order truncation errors of subsequent stages cancel each other (cf., Hyman, 1979). In some cases it may be more efficient and more accurate to use a single-step method with a smaller time step. To make the comparison fair, we introduce a modified amplification factor that accounts for the number of right-hand side computations:

$$\lambda'(\omega \Delta t) = (\lambda(r \cdot \omega \Delta t))^{1/r}, \tag{A.10}$$

r is the number of right-hand side computations (e.g., $r = 1$ for single-step methods; $r = 2$ for predictor–corrector methods; $r = 3.4$ for RK3 and RK4, respectively). λ' is the composite amplification factor per right-hand side computation.

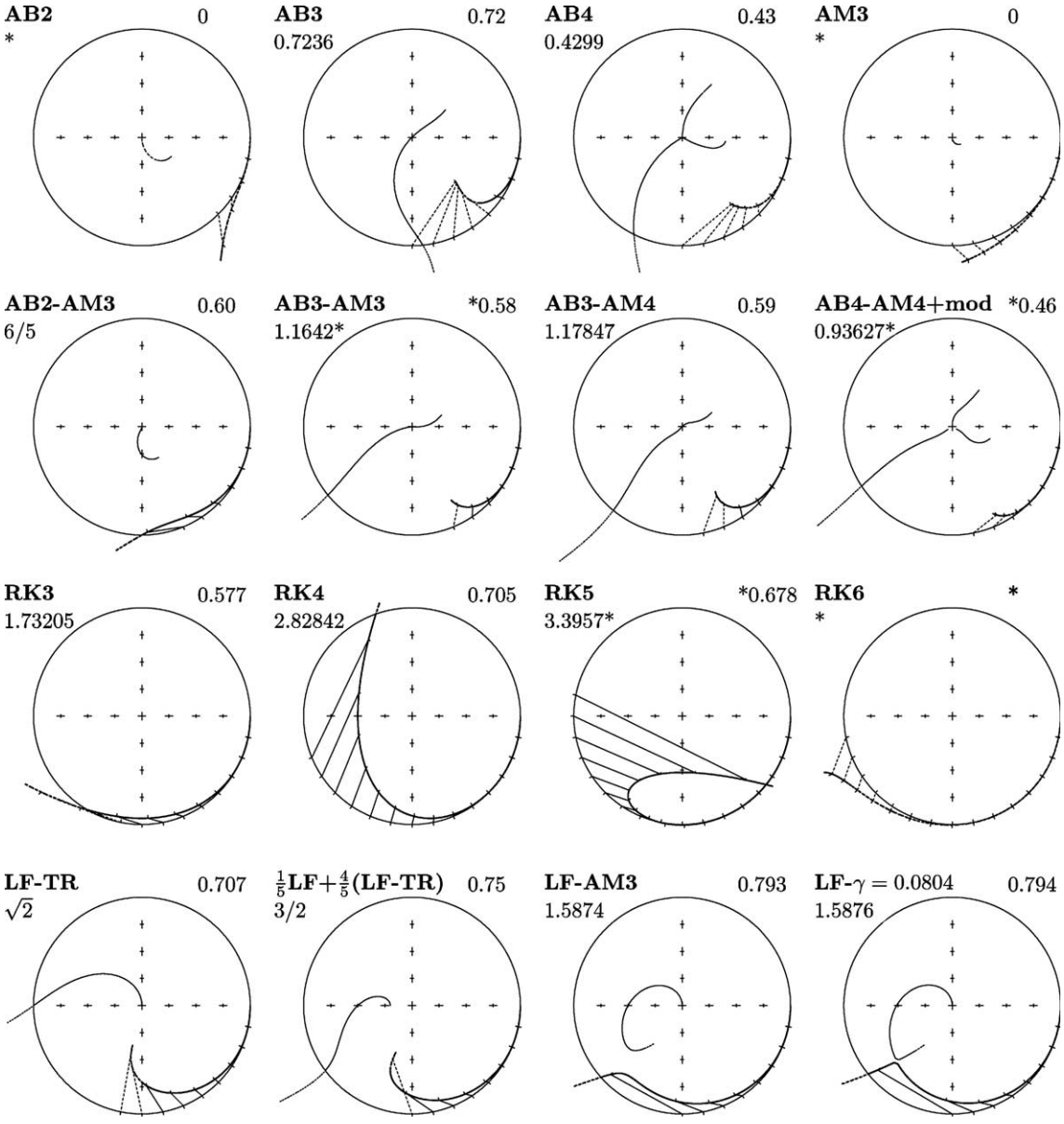

Fig. 20. Amplification factors for simple time-stepping methods plotted on the complex plane relatively to the unit circle. Bold lines correspond to the physical mode and thin lines to the computational mode(s) if any. Once the stability limit is exceeded, solid lines turn to dashed for all modes. The legend is as follows: LF—Leap Frog; TR—trapezoidal rule; AB—Adams–Bashforth; AM—Adams–Moulthon; RK—Runge–Kutta; digits 2, 3, 4 denote the order of accuracy; mod means modification of Milne, in this context $[\mathrm{AB4}-\mathrm{AM4}+\mathrm{mod}]=\frac{251}{270}[\mathrm{AB4}-\mathrm{AM4}]+\frac{19}{270}[\mathrm{AB4}]$, which is formally fifth-order accurate; numbers below the label is the stability limit. An asterisk (*) indicates asymptotic instability; the physical mode of AB4 – AM4 + mod is is weakly unstable, and 0.93627 is the threshold of strong instability of the computational mode. The number on the right is the efficiency factor (stability limit divided by the number of computations of the right-hand side). For each method, the roots of the computational mode corresponding to "ideal" amplification factors of $\exp\{-\frac{\pi i}{16},\ -\frac{\pi i}{8},\ -\frac{3\pi i}{16},\ldots\}$ are connected by straight lines with their ideal locations. This line illustrates the numerical error: shifts in azimuthal and radial directions correspond to phase and amplitude errors, respectively.

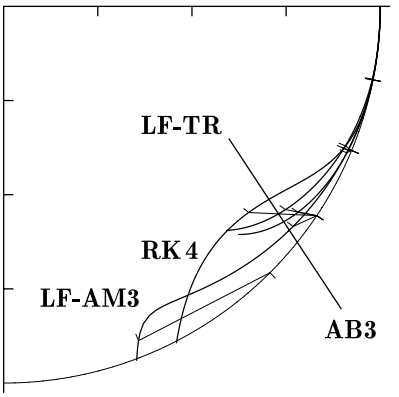

Fig. 21. A fair comparison of time-stepping algorithms: the amplification factor of the physical mode normalized by the number of computations of the right-hand side. Each curve is shown within the limits of stability for its method.

The results are shown in Fig. 21. This comparison shows that AB3 and LF–AM3 offer the best accuracy per computational cost, leaving RK4 and LF–TR behind. RK4 is definitely the most accurate if $\omega\Delta t < \frac{\pi}{16}$, but it rapidly departs from the unit circle when $\omega\Delta t > \frac{\pi}{8}$. AB3 and LF–AM3 are less dissipative than RK4 and LF–TR in the vicinity of $\omega\Delta t = \pi/8$, with LF–AM3 having somewhat larger phase-lead errors than AB3. Finally, none of these algorithms is accurate if used in a computational regime requiring less than 10 right-hand side computations per period of physical oscillation. LF (not shown here) has a smaller phase error than LF–AM3 if both are used in the computational regimes close to their limits of stability, but it lacks third-order accuracy, resulting in a noticeable phase-lead error even for well resolved frequencies. As a rule of thumb, one may conclude that that $\omega\Delta t \approx 0.8r$ sets a "speed limit" per computational cost for virtually all of the explicit algorithms considered here.

For the advection problem the truncation error of spatial differencing always causes a phase delay for high wavenumbers; therefore, a partly compensating phase-lead error of the time stepping algorithm can be tolerated. In fact, if a second-order spatial discretization is used, there is no need for the use of an algorithm other than LF since its phase-lead error is always less than the delay caused by spatial differencing, with compensation occurring only at the limit of stability. In the case of fourth- or higher-order spatial differencing, as well as for second-order differencing on a staggered grid (e.g., the shallow-water system on a C-grid), the use of a higher-order algorithm (i.e., AB3 or LF–AM3) is beneficial because the overall phase error may be dominated by the time-integration error.

Another method worth consideration is the generalized Adams–Bashforth step

$$q^{n+1} = q^n + \mathrm{i}\alpha\left\{\left(\frac{3}{2}+\beta\right)q^n - \left(\frac{1}{2}+2\beta\right)q^{n-1} + \beta q^{n-2}\right\}, \tag{A.11}$$

where β is an adjustable parameter. The choice $\beta = 0$ corresponds to AB2, while $\beta = 5/12$ yields a third-order accurate AB3 that achieves the best possible order of accuracy on the given stencil. In the case where ($\beta < 1/6$, the method has an asymptotic instability of the physical mode (similar to that of AB2). Setting $\beta = 0.281105$ corresponds to the case where the physical and one of the computational modes meet each other (Fig. 22). Below this value the instability of the physical mode

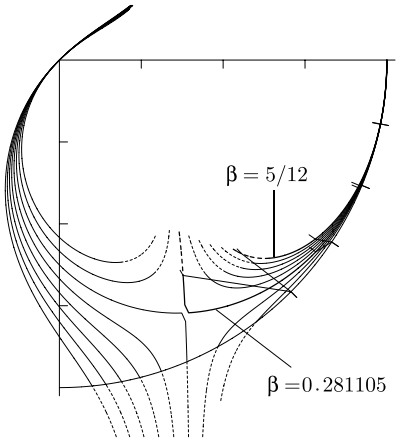

Fig. 22. Amplification factors for β-family of Adams–Bashforth time-stepping algorithms. Highlighted curves correspond to $\beta = 0.281105$ (where the physical and one of the computational modes meet each other at the saddle point; this choice approximately coincides with the maximum possible stability limit of $\alpha = 0.78616$) and $\beta = 5/12$ (the usual, third-order AB3 method).

occurs first (as in the case of LF–AM3), while past it one of the computational modes goes unstable first (as in the case of AB3). This latter value β yields a stability limit of $\alpha = 0.78616$ that approximately coincides with that for the β value corresponding to the largest possible stability limit.

References

Arakawa, A., Lamb, V.R., 1977. Computational design of the basic dynamical processes of the UCLA general circulation model. Methods Comput. Phys. 17, 174–267.

Asselin, R., 1972. Frequency filter for time integations. Month. Weath. Rev. 100, 487–490.

Beckmann, A., 1998. The representation of bottom boundary layer processes in numerical ocean circulation models. In: Chassignet, E.P., Verron, J. (Eds.), Ocean modeling and Parametrization. Kluwer Academic Publishers, Dordrecht, pp. 135–154.

Bleck, R., Smith, L.T., 1990. A wind-driven isopycnic coordinate model of the north and equatorial Atlantic Ocean: 1. Model development and supporting experiments. J. Geophys. Res. 95C, 3273–3285.

Blumberg, A.F., Mellor, G.L., 1987. A description of a three-dimensional coastal ocean circulation model. In: Heaps, N. (Ed.), Three-dimensional Coastal Ocean Models, pp. 1–16 (Pub. AUG).

Brown, J.R., Campana, K.A., 1978. An economical time difference system for numerical weather prediction. Month. Weath. Rev. 106, 1125–1136.

Bryan, K., Cox, M., 1969. A numerical method for the study of the circulation of the world ocean. J. Comp. Phys. 4, 347–376.

Canute, C., Hussaini, M.Y., Quarteroni, A., Zang, T.A., 1988. Spectral Methods in Fluid Mechanics. Springer-Verlag, Belin, 567p.

Dietrich, D.E., Lin, C.A., Mestas-Nunez, A., Ko, D.-S., 1997. A high resolution numerical study of Gulf of Mexico fronts and Eddies. Meteorol. Atmos. Phys. 64, 187–201.

Dukowitz, J.K., Smith, R.D., Malone, R.C., 1993. A reformulation and implementation of the Bryan–Cox–Semtner ocean model on the connection machine. J. Atmos. Oceanic Technol. 10, 195–208.

Dukowitz, J.K., Smith, R.D., 1994. Implicit free-surface method for the Bryan–Cox–Semtner ocean model. J. Geophys. Res. 99, 7991–8014.

Dukowicz, J.K., 1994. Computational efficiency of the hybrid penalty-pseudocompressibility method for incompressible flow. Comput. Fluids 23 (2), 479–486.

Durran, D.R., 1991. The third-order Adams–Bashforth method: an attractive alternative to leapfrog time differencing. Month. Weath. Rev. 119, 702–720.

Dvinsky, A.S., Dukowicz, J.K., 1993. Null-space-free methods for the incompressible Navier–Stokes equations on non-staggered curvilinear grids. Comput. Fluids 22 (6), 685–696.

Farrow, D.E., Stevens, D.P., 1995. A new tracer advection scheme for Bryan–Cox type ocean general circulation models. J. Phys. Ocean. 25, 1731–1741.

Griffies, S.M., Boning, C., Bryan, F.O., Chassignet, E.P., Gerdes, R., Hasumi, H., Hirst, A., Treguier, A.-M., Webb, D., 2000. Development in ocean climate modeling. Ocean Model. 2, 123–192.

Haidvogel, D.B., Arango, H., Hedstrom, K., Beckmann, A., Rizzoli, P., Shchepetkin, A.F., 2000. Model evaluation experiments in the North Atlantic Basin: simulations in non-linear terrain-following coordinates. Dyn. Atmos. Oceans 32, 239–281.

Hallberg, R.W., 1997. Stable split time stepping schemes for large scale ocean modeling. J. Comp. Phys. 135, 54–65.

Hamming, R.W., 1989. Digital filters, third ed. Prentice-Hall, Englewood Cliffs, NJ.

Haney, R.L., 1991. On the pressure gradient force over steep topography in sigma coordinate ocean models. J. Phys. Ocean. 21, 610–618.

Higdon, R.L., Bennett, A.F., 1996. Stability analysis of operator splitting for large-scale ocean modelling. J. Comp. Phys. 123, 311.

Higdon, R.L., de Szoeke, R.A., 1997. Barotropic–baroclinic time splitting for ocean circullation modeling. J. Comp. Phys. 135, 31–53.

Higdon, R.L., 2002. A two-level time-stepping method for layered ocean circulation models. J. Comp. Phys. 177, 59–94, doi:10.1006/jcph.2002.7003.

Holland, Lin, 1975. On the generation of mesoscale eddies and their contribution to the oceanic general circulation. J. Phys. Ocean. 5, 642–657.

Hyman, J.M., 1979. A method of lines approach to the numerical solution of conservation laws. In: Vichnevetsky, R., Stepleman, R.S. (Eds.), Advances in Computer Methods for Partial Differential Equations, vol. III, pp. 313–321 , (Pub. IMACS).

Killworth, P.D., Stainforth, D., Webb, D.J., Paterson, S.M., 1991. The development of a free-surface Bryan–Cox–Semtner ocean model. J. Phys. Ocean. 21, 1333–1348.

Leonard, B.P., Lock, A.P., McVean, M.K., 1996. Conservative explicit unrestricted-time-step constancy preserving advection schemes. Month. Weath. Rev. 124, 2588–2606.

Lilly, D.K., 1965. On the computational stability of time-dependent non-linear geophysical fluid dynamics problem. Month. Weath. Rev. 93, 11–26.

Lin, S.-J., 1997. A finite volume integration method for computing pressure gradient force in general vertical coordinates. Q. J. R. Meteorol. Soc. 123, 1749–1762.

Maas, L.R.M., 1997a. Topographic filtering and reflectionless transmission of long waves. J. Phys. Ocean. 27, 195–202.

Maas, L.R.M., 1997b. On the nonlinear Helmholtz response of almost-enclosed tidal basins with sloping bottoms. J. Fluid Mech. 349, 361–380.

Marchesiello, P., McWilliams, J.C., Shchepetkin, A., 2003. Equilibrium structure and dynamics of the California Current System. J. Phys. Ocean. 33, 753–783.

Mesinger, F., Arakawa, A., 1976. Numerical Methods used in atmospheric models, vol. 1, GARP Publ. Ser. 17., World Meteor. Org., 64pp.

Multigrid Methods, 1981. NASA Conference Publication 2202. 303p, (call # QA 377 M944).

Munnich, M., 1993. On the influence of bottom topography on the vertical structure of internal seiches. Disssertation. ETH Zürich, 97pp.

Nadiga, B.T., Hecht, M.W., Margolin, L.G., Smolarkiewicz, P.K., 1997. On simulating flows with multiple time scales using a method of averages. Theoret. Comput. Fluid Dyn. 9, 281–292.

Shchepetkin, A.F., McWilliams, J.C., 2003. A method for computing horizontal pressure-gradient force in an oceanic model with a non-aligned vertical coordinate. J. Geophys. Res. 108 (C3), 3090, doi:10.1029/2001C001047.

Skamarock, W.C., Klemp, J.B., 1992. The stability of time-split numerical methods for the hydrostatic and the nonhydrostatic elastic equations. Month. Weath. Rev. 120, 2109–2197.

Song, Y.T., Haidvogel, D., 1994. A semi-implicit ocean circullation model using a generalized topography following coordinate system. J. Comp. Phys. 115, 228–248.

Willebrand, J., Barnier, B., Böning, C., Dieterich, C., Killworth, P.D., LeProvost, C., Jia, Y., Molines, J.-M., New, A.L., 2001. Circulation characteristics in three eddy-permitting models of the North Atlantic. Progress Oceanogr. 48, 123–161.

Yanenko, N.N., 1971. The method of fractional steps. Springer-Verlag, Berlin, 160p.